# Modeling and Experimental Validation of a Low-Lift, Vapor Compression Heat Pump

By Muhammad Tauha Ali

A Thesis Presented to the Masdar Institute of Science and Technology in Partial Fulfillment of the Requirements for the Degree of

Master of Science in Mechanical Engineering

August 2011



AUTHOR'S DECLARATION

I understand that copyright in my thesis is transferred
to Masdar Institute of Science and Technology.

Author ____________________________________

RESEARCH SUPERVISORY COMMITTEE MEMBERS

Dr. Peter Armstrong, Chair, ____________________________________

Masdar Institute of Science and Technology

Dr. Matteo Chiesa, ____________________________________

Masdar Institute of Science and Technology

Dr. Scott Kennedy, ____________________________________

Masdar Institute of Science and Technology

# Abstract

In this study, a heat pump test stand and a test chamber have been built for assessment of the energy savings of low-lift radiant-cooling cooling technology with pre-cooling control. The heat pump test stand has been built from a conventional split unit heat pump to be able to operate in either Direct Expansion (DX) mode or Chiller mode. A central data acquisition and control system has been developed for controlling compressor speed, condenser fan speed and expansion valve position. Component models have been developed from first principles to model the performance of the heat pump in DX mode or Chiller mode. The objective of this study is to present a system model based on first principles with minimum parameters estimation. The system model is found to accurately predict the system COP within ±20% for both Chiller mode and DX mode operation for majority of data points. Assessment of the effect of refrigerant oil on heat pump performance is also provided. The refrigerant oil tends to increase heat transfer in the fan-coil condenser and brazed-plate evaporator. However, at low refrigerant flow rates, the heat transfer was found to decrease for fan-coil condenser. The pressure drop was found to increase in the heat exchangers with inclusion of oil. A comparison between the component models developed in this study and those presented in (Zakula, 2010) is also given. The models developed in this study provide better estimation of system parameters especially for pressure drop. Equations for controlling condenser and compressor fan speeds during pre-cooling control for optimal operation based on the optimization results presented in (Zakula, 2010) are also presented for use in pre-cooling control.

*This research was supported by the Government of Abu Dhabi to help fulfill the vision of the late President Sheikh Zayed Bin Sultan Al Nayhan for sustainable development and empowerment of the UAE and humankind.*

Acknowledgments

I am firstly grateful to Almighty Allah for giving me the strength and ability to carry out this study. Secondly, I like to thanks Dr. Peter Armstrong for his thoughtful and wide-ranging advice throughout the study. I am grateful to all my friends especially Arslan Khalid for his stepper motor circuit used for controlling of the expansion valve, Zaid Thaboub and Abdul Qadir for assisting me in insulation of test chamber and Marwan Mokhtar for providing me initial guidance on instrumentation. I like to acknowledge my colleagues at Massachusetts Institute of Technology, Nicholas Gayeski for laying down the foundation of my experimental work and providing me his test stands experimental data set, Tea Zakula for sending me the MATLAB code of her heat exchanger models and Ryan Willingham for providing me the start in learning of CRBasic and Acetylene welding. I also want to thank Masdar security guards who provided the necessary assistance in times of need while preparing the test facility. Lastly, I like to thank my family for nourishing me during my course of work.

# Contents

# List of Tables

# List of Figures

# CHAPTER 1

# Introduction

Global warming is both a cause and effect of the use of active air-conditioning systems for maintaining comfort level for humans. Buildings account for over 40% of primary energy usage in the world (World Building Council for Sustainable Development (WBCSD), 2008). Around 30% (Radhi, 2009; US Department of Energy, 2010) of this energy is used for air conditioning. For hot and humid climates, such as in United Arab Emirates (UAE), this share can reach 40% and on the peak day exceeds 60% of buildings energy use (Ali, Mokhtar, Chiesa, & P. Armstrong, 2011; Radhi, 2009). Due to global warming and increase in energy costs, efforts are being made to enhance the efficiency of air-conditioning equipment by imposing efficiency standards; use of low-energy cooling technologies and by improving the building envelope to reduce cooling/heating loads.

One of the most common methods of increasing equipment efficiency is through implementing variable speed drives in electric motors to match demand. The savings achieved over constant electric drives are reported between 20%-40% (Qureshi & Tassou, 1996; Shimma, Tateuchi, & Sugiura, 1985). Another method for achieving over 40% increase in system efficiency is through radiant cooling (Feustel & Stetiu, 1995; Roth, Westphalen, Dieckmann, S. D. Hamilton, & Goetzler, 2002). The radiant cooling system only handles sensible loads. Therefore, a separate ventilation system is needed to replace humid air with dry air (Feustel & Stetiu, 1995; Niu, L. Z. Zhang, & Zuo, 2002). Among the different types of ventilation systems available for handling latent loads, desiccant dehumidification can achieve up to 25% energy savings over conventional systems (Michael D. Larrañaga, Mario G. Beruvides, H.W. Holder, Enusha Karunasena, & David C. Straus, 2008). For Abu Dhabi, it is estimated that sensible cooling accounts for around 80% of the buildings cooling load (Ali et al., 2011). Implementation of low-lift, radiant cooling with pre-cooling control can reduce this load by around 70% for Abu Dhabi (P. R. Armstrong, Jiang, Winiarski, Katipamula, & Norford, 2009).

This study is part of the low-lift, radiant-cooling with pre-cooling control project being carried out at Masdar Institute (MI), Massachusetts Institute of Technology (MIT) and Pacific Northwest National Laboratory (PNNL). In this study, modeling and experimental validation of conventional vapor compression Direct Expansion (DX) unit equipped with variable speed compressor, condenser and evaporator fan is presented. In chiller mode of operation, the evaporator is modeled as a brazed-plate heat exchanger (HX). The objective of this study is to present a system model based on first principles with minimum parameters estimation.

Chapter 2 presents a review of variable speed compressor savings reported in the literature, system and component models of vapor compression equipment and refrigerant-oil effect on the performance of vapor compression equipment. Component models of the system and the system model are presented in Chapter 3. In Chapter 4, details of experimental setup and instrumentation accuracy are described. Experimental verification of component models and the system model, assessment of effect of refrigerant oil on component models and comparison of the results between the models developed in this study with the models presented in (Zakula, 2010) is presented in Chapter 5. Equations for controlling compressor and condenser speed based on the optimization results of (Zakula, 2010) are also given to be used in pre-cooling control. Lastly, conclusion and directions for future work are presented in Chapter 6.

# CHAPTER 2

# Literature Review

## 2.1 Variable Speed Compressors

In conventional vapor compression equipment, the compressor is driven by a constant speed electric motor. Cooling capacity control is achieved by cylinder unloading, throttling at suction , clearance volume change or by on-off cycling in reciprocating compressors, slide valve position change in rotary or scroll compressors and screw compressors, and changing position of inlet guide vanes in centrifugal compressors (Brown, 1997). Through advancement in electronics technology, speed modulation of electric motors can now be achieved by varying the frequency of power supply. The first reported savings potential of variable capacity control by the use of variable frequency drives (VFD) was presented in (Cohen, J. F. Hamilton, & Pearson, 1974). A system with constant compressor speed, condenser and evaporator fan speed was compared to a system with variable speed compressor, condenser and evaporator fan. Seasonal savings of 28-35% were reported for climates at mid-latitude in US. The savings were mainly attributed to reduced cycling losses, lower condensing temperatures and higher evaporating temperatures at part-loads. In (Qureshi & Tassou, 1996), a comprehensive review of the efforts made to measure the savings potential at residential and commercial level is given. The effects on electrical and mechanical aspects of equipment operation during variable speed are also reviewed.

The mechanical advantages of variable speed compressors most often cited are reduced cycling losses by varying the capacity to meet the demand, accurate temperature control, compressor soft-start and low noise operation (Lida, Yamamoto, Kuroda, & Hibi, 1982). The reduction in pressure ratio from closer approach temperatures also results in increased compressor performance and cycle performance (P. R. Armstrong, Jiang, Winiarski, Katipamula, Norford, et al., 2009; Qureshi & Tassou, 1996; Shimma et al., 1985). The side-effects of implementing inverter drive control are mainly due to harmonics in waveform resulting from waveform modulation. They increase motor losses due to non-sinusoidal waveform, variation in slip of induction motor and torque oscillations resulting in extra stress on windings (Qureshi & Tassou, 1996). It was mentioned by (Rice, 1988) that use of permanent-magnet motor will reduce the slip losses.

Air-conditioning equipment runs on part-load most of the time (Cohen et al., 1974). As mentioned earlier, modulation of the capacity of vapor compression equipment at part-load increases system efficiency due to decreased thermal load for the same heat transfer area. Recent studies (Gayeski, 2010; Gayeski, Zakula, P. R. Armstrong, & Norford, 2010), investigated this effect on a variable speed compressor by running it at low speeds which resulted in very high Coefficient of Performance (COP). This operation of the compressor is termed as low-lift operation as minimum rise in pressure ratio occurs to deliver the required cooling capacity.

## 2.2 Vapor Compression Equipment Modeling

Various models of vapor compression equipment have been presented in the literature. These models can be broadly classified into dynamic and steady state models. Transient modeling is further classified based on the scale of transients such as system startup or compressor valve dynamics and the methodology used in modeling of heat exchangers such as discretized or zonal. Transient modeling of vapor compression equipment is beyond the scope of this thesis. Steady state models of vapor compression equipment range from models based on regression of system variables to models based on first principle analysis of components. An extensive review of these models is provided in (Bendapudi & Braun, 2002; Jin & Spitler, 2002; Iu, 2007).

Hiller and Glicksman are considered to be among the pioneers of modeling of vapor compression cycle's components from first principles (Hiller & Glicksman, 1976). Their model included modeling of compressor, expansion valve and fan-coil HX working as a condenser or evaporator. Their model used real gas properties, accounted for oil circulation effect on compressor capacity and employed modeling of compressor capacity control achieved through clearance volume control or late suction valve closing. Their HX models used zone-by-zone approach which will be explained in section 2.3. The HX models used ε-NTU method for simulation of heat transfer, accounted for pressure drop and in the case of evaporator, effect of moisture presence on evaporator. An empirical model for quick assessment of system performance was presented by Allen and Hamilton (Allen & J. F. Hamilton, 1983). Their model estimated the cooling capacity and compressor power as polynomial functions of condenser and evaporator water temperatures and flow rates. The model of Hamilton and Miller (J. F. Hamilton & Miller, 1990) improved the previous model of (Allen & J. F. Hamilton, 1983) by dividing the system into its components. The component models required refrigerant condition details at the inlet and outlet of the components. The model of Fisher and Rice (Fischer, Rice, & Jackson, 1988) incorporated detailed physical phenomena in the component models. For example, the compressor model included the option of assessing the effect of changes in heat loss and efficiency on compressor power. Also, variable HX conductances were modeled based on different heat transfer phenomenon occurring in the heat exchangers. Empirical models for expansion devices were also included in the system model. The model of Domanski and Didion (Domanski & Didion, 1984) increased the level of detail used to model system components. Damasceno (Damasceno, Goldschmidt, & Rooke, 1990) verified the accuracy of Domanski's model over Fisher's. In Domanski's model, compressor characteristics are captured in greater detail by dividing compressor into five components. The model account for heat transfer and pressure drop between suction and discharge and treats the compression process as a polytropic process. The heat exchangers are also divided into small segments using a tube-by-tube approach which will be explained in section 2.3.

The model presented by Stefanuk (Stefanuk, Aplevich, & Renksizbulut, 1993) chooses the approach of modeling different components based on the physical phenomenon occurring in the components and using experimental data to determine the parameters of each component model. The model presented by Hui Jin (Jin & Spitler, 2002) attempts to minimize the number of parameters needed for such a model. However, certain compromises are made such as compression and expansion processes in the compressor are considered isentropic, constant HX conductance values are assumed and same pressure drop is considered on the discharge and suction side of the compressor. The model presented by Armstrong (P. R. Armstrong, Jiang, Winiarski, Katipamula, Norford, et al., 2009) follows the same approach but considers polytropic processes in the compressor in which the polytropic exponent is modeled as a function of pressure ratio and speed. Also, the model is intended for modeling of a variable speed compressor which is the focus of this study.

## 2.3 Heat Exchanger Modeling

Heat exchangers are usually modeled based on zone-by-zone, tube-by-tube or segment-by-segment approach as described in (Browne & Bansal, 2001; Iu, 2007). In zone-by-zone approach, the HX is divided into zones based on the type of fluid phase. For example, the condenser is divided into de-superheating, condensing and sub-cooling portions. In segment-by-segment or tube-by-tube approach, the HX is discretized into a finite number of elements. Heat transfer and pressure drop calculations are then carried out progressively through the HX.

Extensive experimentation has been carried by researchers to model the air-side heat transfer for different types of fin-tube and fin-plate heat exchangers. A comprehensive review is provided in (Jacobi, Park, Tafti, & X. Zhang, 2001). In the review, correlations and comments on the experimentation with fin-tube HX by the researchers are presented. Effects of fin geometry such as fin pitch, fin type such as plain, wavy, corrugated, louvered etc, tube geometry such as round tube and flat tube and HX operating condition such as dry, wet or frosting are covered. For plain-fin round-tube geometry, it is reported that the heat transfer increases slightly with smaller fin thickness while pressure drop increases for higher fin pitch with negligible influence on heat transfer. A comparison between fin-round tube HX and fin-flat tube HX is also provided. It is concluded that flat-tube HX have higher heat transfer compared to round-tube but during wet operating conditions, the degradation in heat transfer for flat-tube is higher than for round tubes.

The correlation of Grey and Webb (Gray & Webb, 1986) is recommended for modeling heat transfer phenomena in plain-fin round-tube HX over a broad range of parameters.

The fin efficiency for plain-fin round-tube HX is usually calculated based on approximations developed for the circular fin efficiency formulation (Perrotin & Clodic, 2003). The equivalent circular fin method and the sector method can be used for calculation of fin efficiency. The fin profile is considered to be a square for inline tubes and hexagonal for staggered tubes. In the sector method, the fin is divided into several circular sectors based in the tube center and the fin geometry. The sector efficiency is then evaluated from the exact solution for circular fins with an adiabatic tip or from approximations to that solution. In the equivalent circular fin method, the fin efficiency can be calculated by considering a circular fin having the same surface area as a rectangular or hexagonal fin based on tube arrangements or through the Schmidt method (Schmidt, 1949). The Schmidt method is simpler to use than the sector method in which correlations have been developed by Schmidt to find an equivalent circular fin having the same fin efficiency as the rectangular fin or the hexagonal fin. A comparison between the sector and equivalent circular fin method is given in (Perrotin & Clodic, 2003). Use of equivalent circular fin method is recommended for the case of plain fins.

Heat transfer and pressure drop in the two-phase of refrigerants have been investigated extensively for different commercial refrigerants in the case of fin-tube HX. The two-phase heat transfer is generally modeled through three approaches. In the enhancement model approach, the single-phase heat transfer coefficient is multiplied by an enhancement factor. The weighted model considers two-phase heat transfer coefficient to be a sum of convective and film/nucleate condensation/boiling with appropriate weights. A variation on the weighted model is the asymptotic model in which the sum of aforementioned components is considered with appropriate exponents (Wojtan, 2005).

The condensation or evaporation heat transfer is usually modeled by an enhancement model in which the single-phase heat transfer coefficient is multiplied by ratio of vapor quality, viscosity and density ratios, Martinelli parameter ($X_{tt}$)[1], etc. An example of such a model is of Shah (Shah, 1979) which is extensively used because of its simplicity. A comparison of different condensation and evaporation heat transfer correlation developed for modeling refrigerant heat transfer in condensation is presented in (Boissieux, Heikal, & Johns, 2000a, 2000b; Cavallini et al., 2002). It is shown that for older refrigerants such as R22, R-407C etc, the simple enhancement models were able to predict the heat transfer coefficient within ±20%. However, it is mentioned in (Thome, El Hajal, & Cavallini, 2003) that the enhancement model type correlations that were developed earlier over predicts the heat transfer by 20-40% for condensation when applied to new refrigerants working at high pressures such as R410a. A new weighted type model is presented for which prediction of the heat transfer data is reported to be within ±20% for a range of mass flux, tube diameters and refrigerant pressures.

The flow pattern map of Wojtan et. al (Wojtan, Ursenbacher, & Thome, 2005a) is used to identify the different flow regimes. This map is the modified version of Thome El Hajjal map (El Hajal, Thome, & Cavallini, 2003) which was used to develop the superposition model and condensation heat transfer correlations for convective and film condensation. In the new map, two flow regimes namely dryout and mist are added while the stratified-wavy regime is classified into three separate flow regimes based on experimental data. The heat transfer

[1] It is the ratio of theoretical pressure drop that would occur if each fluid could flow separately in the complete cross section with the original rate of each phase (Wojtan, 2005).

correlations for the convective boiling and the nucleate boiling are taken from (Wojtan, Ursenbacher, & Thome, 2005b) as they were developed using this flow pattern map with refrigerant R410a.

There are three approaches that have been found in literature for estimation of two-phase pressure drop. The analytical approach requires solving of differential equations which often require numerical procedures and hence are not suitable for practical implementation. Another method for evaluation of pressure drop is to fit simple models to the experimental data for calculation of pressure drop. The drawback of such an approach is that the result is applicable for a certain range of conditions and the effect of different flow regimes occurring in the two-phase flow is not accounted. A phenomenological based approach uses flow pattern maps to account for different flow regimes and hence is less affected by changes in system fluids. However, curve fitting is still required (Moreno Quibén & Thome, 2007a). A comparison of different flow pattern based models is presented in (Moreno Quibén & Thome, 2007a; Tribbe & Müller-Steinhagen, 2000). The models were tested against an experimental data base with wide range of fluids, diameter, mass and heat fluxes. It is shown in (Moreno Quibén & Thome, 2007a) that empirical models of Friedel (Friedel, 1979) and Grönnerud (Grönnerud, 1972) predict only 67% and 46% of the database within ±30%. A flow pattern based model using the latest flow pattern map of Wojtan et. al (Wojtan, Ursenbacher, & Thome, 2005a) is presented in (Moreno Quibén & Thome, 2007a). The model was able to predict 82% of the database to within ±30%.

There is a lack of availability of open literature on modeling of heat transfer and pressure drop phenomenon due to proprietary nature of brazed-plate HX (Ayub, 2003). In (Ayub, 2003), a survey of the available single-phase heat transfer and pressure drop correlation is presented. It is mentioned that most of the correlations have been developed for specific brazed-plate HX geometry. However, a few correlations are recommended for general use. In (García-Cascales, Vera-García, Corberán-Salvador, & Gonzálvez-Maciá, 2007), review and comparison of the available single-phase and two-phase heat transfer correlations for brazed-plate HX are presented. It is pointed out that the correlations of (Muley & Manglik, 1999) and (Martin, 1996) for single-phase heat transfer and pressure drop tried to generalize the heat transfer correlation by including dependencies of chevron angle and enlargement factor. For two-phase heat transfer, nucleate boiling is the dominant phenomenon at low vapor qualities and high heat fluxes. The correlation of (Cooper, 1984) and (Tran, 1998) is shown to predict majority of the experimental data within ±20% in (Claesson, 2005). However, as the HX geometry features such as chevron angle, area enlargement etc. are not taken into account, these correlation deviates from the experimental data at high vapor quality. Correlations developed specifically for refrigerant condensation and evaporation are presented in (García-Cascales et al., 2007). Correlations of (Hsieh & T. F. Lin, 2002) and (Han, Lee, & Y. H. Kim, 2003) have been developed using R410a as the system fluid. It is shown in (Hsieh & T. F. Lin, 2002) that variation in mass flux doesn't affect the heat transfer coefficient while the heat transfer coefficient increases linearly with heat flux. The correlation of (Han et al., 2003) takes into account HX geometry such as HX pitch and chevron angle but the range of heat fluxes and chevron angles used in its development is limited. It is mentioned in (Han et al., 2003; Hsieh & T. F. Lin, 2002) that the pressure drop in two-phase flow is mainly dependent on vapor quality. Higher vapor quality increases turbulence resulting in increased pressure drop. The effect of mass and heat flux on the pressure drop are minimal while increasing chevron angle results in lower pressure drop for a given evaporating temperature. The pressure drop is observed to increase with decreasing evaporation temperature due to change in specific volume of the saturated vapor.

## 2.4 Oil Effect on Vapor Compression System

A comprehensive review concerning estimation of oil properties, modeling of refrigerant-oil mixture, effect of oil on performance of vapor compression system and on heat exchangers have been presented in (Bandarra Filho, Cheng, & Thome, 2009; Conde, 1996; Shen & Groll, 2005; Youbi-Idrissi & Bonjour, 2008). For compressors, the effect of oil is to reduce the refrigerant mass flow rate and isentropic efficiency. Also, the nominal oil concentration in refrigerant is found to increase when Polyol Ester Oil (POE) is used as compared to mineral oils. It is mentioned in (Shen & Groll, 2005; Youbi-Idrissi & Bonjour, 2008) that oil in the refrigerant decreases the heat transfer and increases the pressure drop. There are contradictory reports in literature on the effect of oil for refrigerant heat transfer in two-phase for heat exchangers. In (Shen & Groll, 2005; Youbi-Idrissi & Bonjour, 2008), increasing the oil concentration is reported to decrease evaporator capacity and increase pressure drop. This decrease in heat transfer and increase in pressure drop are attributed to higher refrigerant-oil mixture viscosity and change in the saturation temperature of the mixture due to difference in bubble temperature of two fluids. However, COP of the system is found to be higher when miscible oils such as POE are used compared to immiscible oils. (Hambraeus, 1995) found that a miscible oil of lower viscosity increases the heat transfer coefficient as compared to a miscible oil of higher viscosity. However, reason for this increase is not reported. In (Bandarra Filho et al., 2009), an effort is made to explain the increase in heat transfer for small oil concentrations is given that was reported in some studies. The enhancement depends on type of lubricant oil, heat flux, mass flux, flow patterns and type of tubes. However, it is mentioned that an exact explanation for enhancement has never been truly identified. Heat transfer is found to increase with increase in mass flux due to promotion of annular flow because of higher surface tension of oil. The studies investigating effect of ester based oils with R-134a and R-410a on heat transfer have found that at low and intermediate vapor qualities, inclusion of small concentration of oil has a positive influence on heat transfer (Doerr, Pate, & Eckels, 1994; Hambraeus, 1995; Hu, Ding, Wei, Z. Wang, & K. Wang, 2008; Nidegger, Thome, & Favrat, 1997; Tche´ou & McNeil, 1994; Zu¨ rcher, Thome, & Favrat, 1997). However, at high vapor qualities oil tends to negatively influence heat transfer. It is suggested in (Bandarra Filho et al., 2009) that correlations developed for pure refrigerants can be applied using the refrigerant-oil mixture properties for calculation of heat transfer. However, for two-phase pressure drop, corrections should be made to the pure refrigerant friction factor correlations.

Investigation of varying oil concentration on system performance by varying compressor speed of a rotary compressor is presented in (Sarntichartsak, Monyakul, Thepa, & Nathakaranakule, 2006). For R-407c/POE oil mixture, the oil concentration varied from 0.5-1% oil concentration with 1litre of POE oil compressor charge. The compressor's electrical frequency variation was in the range of 30-50Hz. It was reported that increasing the oil concentration tends to have a negative influence on system performance.

# CHAPTER 3

# Component Modeling

## 3.1 Vapor Compression Cycle

The conventional vapor compression heat pump is comprised of a compressor, condenser, expansion valve and evaporator. In this study, models are developed for modeling the physical phenomenon occurring in each of them. The component models comprise of compressor, condenser and evaporator. The evaporator is modeled as a fin-tube HX for DX mode of operation and as a brazed-plate HX for chiller mode of operation. The expansion valve is modeled as an isenthalpic process.

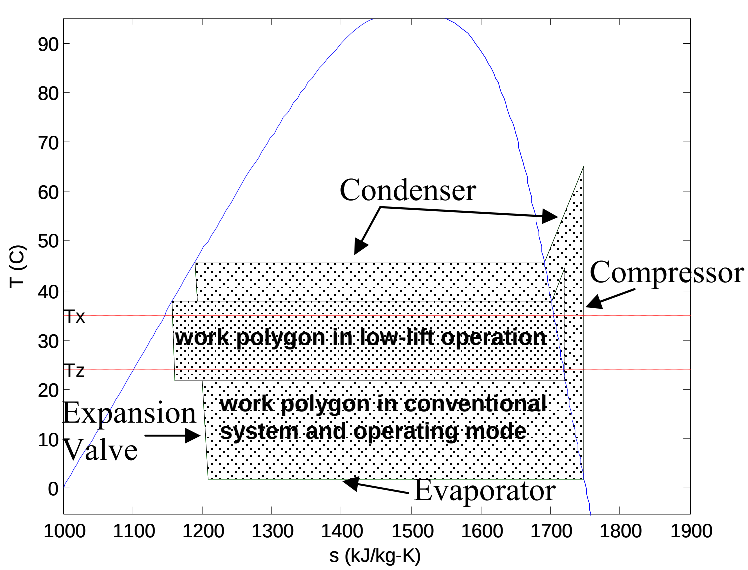


Figure 3.1: T-s diagram of vapor compression cycle with low-lift operation illustration (P. R. Armstrong, Jiang, Winiarski, Katipamula, & Norford, 2009)

Figure 3.1 illustrates the thermodynamic processes that occur in the components of a vapor compression cycle. It can be observed from Figure 3.1 that during low-lift operation the work done by the compressor has been reduced significantly while the magnitude of heat transfer processes that occur inside the condenser and evaporator remains approximately the same. This result in a significant increase in COP of the system which is illustrated in Figure 4.7 and Figure 4.8 presented in Chapter 4.

### 3.2 Refrigerant Oil-Mixture Modeling

In a vapor compression system, oil is required to lubricate the moving parts of the compressor. Due to clearances required for moving of compressor parts, some oil gets carried to the other parts of the system. The general trend of oil is to reduce the heat transfer and increase the pressure drop though researchers have found that presence of oil may sometimes enhance the heat transfer in the two-phase region (Bandarra Filho et al., 2009; Hu et al., 2008). The oil effect on the system performance is modeled using the property equations available in the literature. It is shown in (Thome, 2004) that the Equation 3.2.2 is valid for lubricating oils for temperature range of -18-204°C and specific gravity[2] range of 0.75-1.05. The specific gravity of POE oil for Viscosity Grade (VG) 22 to VG68 is in the range of 0.98-0.995 at 20°C ("Harp Lubricants – Technical Data Sheet Harp Polyol Ester Oils,"). The property equations found in the literature have been developed for refrigerant oil POE/VG68 properties which are given in Equations 3.2.1-3.2.5 (Wei, Ding, Hu, & K. Wang, 2008):

---

[2] Specific gravity is defined as ratio of density of a substance to the density of reference substance such as water.

$$\rho_{oil} = (0.97386 - 6.91673e - 4 * (T - 273))/1e3 \tag{3.2.1}$$

$$cp_{oil} = 4.186 * \frac{0.388 + 0.00045 * (1.8 * (T - 273) + 32)}{\left(\frac{\rho_{oil}}{998.5}\right)^{.5}} \tag{3.2.2}$$

$$k_{oil} = .\frac{1172}{\frac{\rho_{oil}}{998.5}} * (1 - 0.0054 * (T - 273)) \tag{3.2.3}$$

$$\mu_{oil} = \left(1062.075 * \exp\left(-\frac{T - 273}{32.29}\right) + 4.90664\right) * 1e^{-6} * \rho_{oil} \tag{3.2.4}$$

$$\sigma_{oil} = \left(29 - 0.4 * (T_{sat} - 273)\right) * 1e^{-3} \tag{3.2.5}$$

The oil is miscible with the refrigerant in liquid phase only. The nominal oil concentration is therefore specified based on oil mass fraction at the condenser outlet as given by Equation 3.2.6:

$$\omega_{oil} = \frac{m_{oil}}{m_{ref_{liq}} + m_{oil}} \tag{3.2.6}$$

However, when the refrigerant is in two-phase, the nominal oil concentration doesn't represent the true oil concentration of refrigerant-oil mixture. The local oil concentration of refrigerant-oil mixture increases with increasing vapor quality (Wei et al., 2008). The local oil concentration can be obtained from conservation of mass and is given in Equation 3.2.7:

$$\omega_{local} = \frac{\omega_{oil}}{(1 - x)} \tag{3.2.7}$$

It is mentioned in (Bandarra Filho et al., 2009) that the vapor quality at the exit of the evaporator is always less than one because of miscibility of oil with refrigerant. Therefore, refrigerant properties at the evaporator outlet are always evaluated at saturated pressure and vapor quality of 1-$\omega_{oil}$. Figure 3.2 illustrates the variation in local oil concentration in the two-phase region.

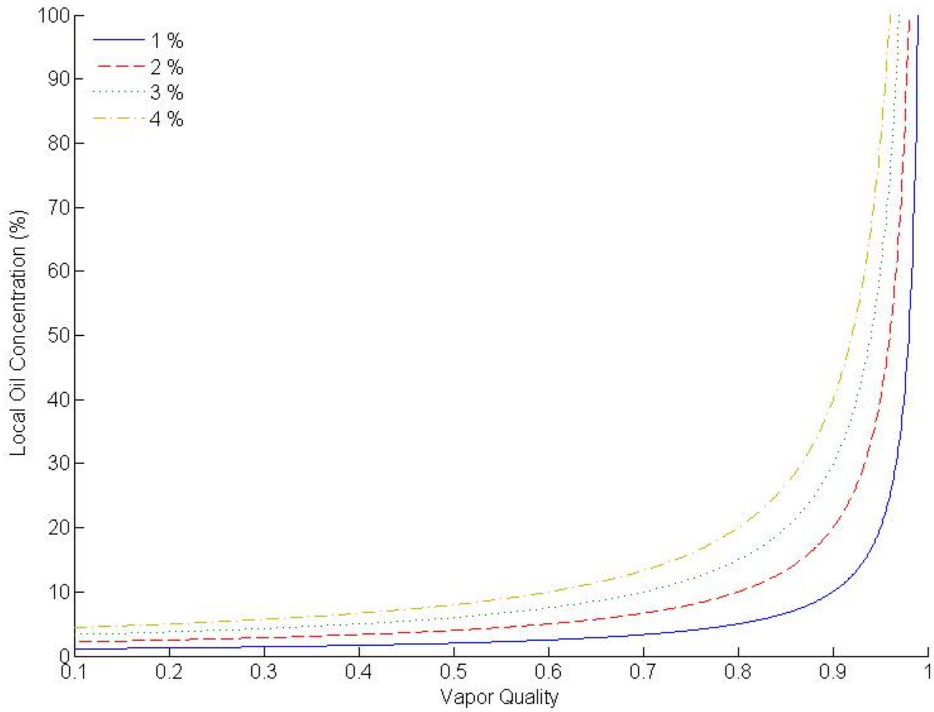


Figure 3.2: Local oil concentration vs. vapor quality

The heat transfer and pressure drop correlations used in this study have been developed for pure refrigerant. The use of pure refrigerant correlations with refrigerant-oil mixture properties have been used by researchers for modeling oil effect (Bandarra Filho et al., 2009). The refrigerant-oil mixture properties are calculated from the mixture models given in Equations 3.2.8-3.2.13 (Bandarra Filho et al., 2009; Youbi-Idrissi & Bonjour, 2008) while refrigerant properties of R410a are calculated from Refprop 8.0.:

$$\rho_{ref-oil} = \left(\frac{\omega_{local}}{\rho_{oil}} + \frac{1-\omega_{local}}{\rho_{ref_{liq}}}\right)^{-1} \tag{3.2.8}$$

$$cp_{ref-oil} = (1-\omega_{local}) * cp_{ref_{liq}} + \omega_{local} * cp_{oil} \tag{3.2.9}$$

$$k_{ref-oil} = k_{ref_{liq}} * (1 - \omega_{local}) + k_{oil} * \omega_{local} - 0.72 * \left(k_{oil} - k_{ref_{liq}}\right) * (1 - \omega_{local}) * \omega_{local} \quad (3.2.10)$$

$$\mu_{ref-oil} = \mu_{ref}^{1-\omega_{local}} * \mu_{oil}^{\omega_{local}} \quad (3.2.11)$$

$$\sigma_{ref-oil} = \sigma_{ref_{liq}} + \left(\sigma_{oil} - \sigma_{ref_{liq}}\right) * \omega_{local}^{0.51} \quad (3.2.12)$$

$$h_{ref-oil} = h_{ref_{liq}} * (1 - x - \omega_{oil}) + \omega_{oil} * h_{oil} + x * h_{ref_g} \quad (3.2.13)$$

The refrigerant passes through an oil accumulator before entering the compressor as shown in Figure 4.1. Therefore, enthalpies at the compressor outlet and inlet are calculated using Equation 3.2.14 to account for effect of oil.

$$h_{ref-oil} = h_{ref} + \omega_{oil} * h_{oil} \quad (3.2.14)$$

Due to presence of oil, the saturation temperature of the refrigerant-oil mixture deviates from that of the pure refrigerant. Therefore, use of saturation temperature for calculation of two-phase heat transfer is not correct. In (Bandarra Filho et al., 2009), a bulb temperature is instead suggested for calculation of two-phase heat transfer. The coefficients of the Equation 3.2.16 and Equation 3.2.17 are taken from (Bandarra Filho et al., 2009). The coefficients $a_0$ and $b_0$ are specific to a refrigerant and are calculated using the method given in (Thome, 2004). Equation 3.2.15 is used for calculation of bulb temperature given as:

$$T_{bulb} = \frac{A}{\ln(P_{sat} - B)} \quad (3.2.15)$$

where,

$$A = a_0 + 182.5 * \omega_{local} - 724.2 * \omega_{local}^2 + 3868 * \omega_{local}^3 - 5268.9 * \omega_{local}^4 \quad (3.2.16)$$

$$B = b_0 - 0.722 * \omega_{local} + 2.391 * \omega_{local}^2 - 13.779 * \omega_{local}^3 + 17.066 * \omega_{local}^4 \quad (3.2.17)$$

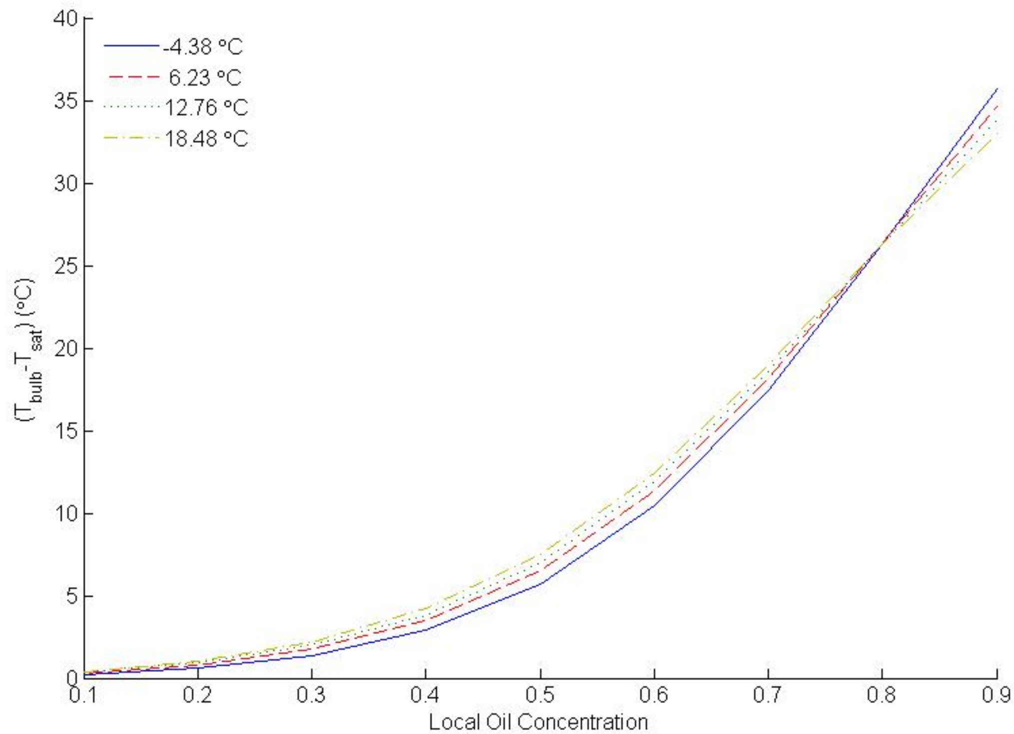


Figure 3.3: Difference between $T_{bulb}$ and $T_{sat}$ of pure refrigerant for different $T_{sat}$ vs. $\omega_{local}$

Figure 3.3 represents the difference between saturation temperature of refrigerant-oil mixture and pure refrigerant. The effect of oil on the mixture's saturation temperature becomes profound for high local oil concentration which occurs in high vapor quality region. It is suggested in (Bandarra Filho et al., 2009), that the mixture properties can be used to calculate heat transfer coefficient in two-phase flow using the correlations developed for pure refrigerants. However, for calculation of pressure drop, an adjustment to the friction factor correlations for two-phase flow is suggested for the model of Moreno et al. (Moreno Quibén & Thome, 2007a). The adjustment is given in Equation 3.2.18:

$$\frac{dP}{dx} = \left(\frac{dP}{dx}\right)_{tp} * \left(\frac{\mu_{oil}}{\mu_{ref}}\right)^{0.184*\omega_{local}} \tag{3.2.18}$$

It is suggested by Thome that at high vapor qualities i.e. vapor quality greater than 0.9 or when dryout occurs in the evaporator, the local oil concentration can be taken as zero in the calculation of heat transfer and pressure drop (Thome, 2011). The oil concentration is taken as 1% of total refrigerant mass flow in this study which is typical of small hermetic compressors ("Hermetic Compressors," 2011). The effect of oil concentration assumption on the vapor compression cycle components is presented in Chapter 5.

## 3.3 Compressor

In this study, a semi-empirical model of compressor volumetric efficiency and mass flow rate is used to estimate the compressor power for given discharge and suction temperatures as presented in (Zakula, 2010). The thermodynamic power is then converted to compressor electrical power using the modified model of Jähnig et al. (Jähnig, Reindl, & Klein, 2000) as presented in (Zakula, 2010).

Equation 3.3.1 describes the compression process:

$$P_1 v_1^n = P_2 v_2^n \tag{3.3.1}$$

where, '$n$' is the polytropic exponent which depends on the type of process. Equation 3.3.2 gives the '$n$' for a real gas undergoing isentropic compression:

$$n_s = \ln\left(\frac{P_2}{P_1}\right) / \ln\left(\frac{\rho_2}{\rho_1}\right) \tag{3.3.2}$$

A compressor in real life doesn't compress all of the volume that is taken in from the suction side due to factors such as the clearance volume, back leakage through valves and out of the compression chamber, pressure loss in the valves mainly suction valve (Jähnig et al., 2000) and heat transfer between suction and discharge side which changes with compressor speed. The mass flow rate through the compressor with no leakage can therefore be described through Equation 3.3.3:

$$\dot{m}_{ref-oil} = C_1 * f_{comp} * \rho_{suc} * \eta_v \tag{3.3.3}$$

where, the constant $C_1$ in Equation 3.3.3 represents the effective swept volume of compressor and '$f_{comp}$' is the compressor speed. Equation 3.3.4 defines the volumetric efficiency $\eta_v$ as:

$$\eta_v = 1 - C_2\left(\left(\frac{P_{dis}}{P_{suc}}\right)^{1/n} - 1\right) \tag{3.3.4}$$

where, the constant $C_2$ represents the clearance volume fraction of the compressor. In the mass flow model given in (Zakula, 2010), the polytropic exponent is taken as the isentropic polytropic exponent. An adjustment is made to the mass flow rate to account for the back leakage which is given in Equation 3.3.5:

$$\dot{m}_{ref-oil} = C_1 * f_{comp} * \rho_{suc} * \eta_v - C_5(P_{dis} - P_{suc}) * \rho_{suc} \tag{3.3.5}$$

The constant $C_5$ in Equation 3.3.5 represents backflow per unit pressure difference. In (Willingham, 2009), a pressure loss model similar to the one presented in (Jähnig et al., 2000) is given. It accounts for the pressure loss in valves and its effect on mass flow rate for a given compressor speed. It also assumes isentropic compression in the compressor. The model is given in Equations 3.3.6-3.3.9:

$$P_{suc_{int}} = P_{suc} - C_3 * \rho_{suc} * {f_{comp}}^2 \tag{3.3.6}$$

$$P_{dis_{int}} = P_{dis} + C_4 * \rho_{dis} * {f_{comp}}^2 \tag{3.3.7}$$

$$\eta_v = 1 - C_2\left(\left(\frac{P_{dis_{int}}}{P_{suc_{int}}}\right)^{1/n} - 1\right) \tag{3.3.8}$$

$$\dot{m}_{ref-oil} = C_1 * f_{comp} * \rho_{suc} * \eta_v \tag{3.3.9}$$

The constants $C_1$ and $C_2$ have the same meaning as in the previous model. However, $C_3$ and $C_4$ represent the ratio of displacement volume to valve area in the suction and discharge valves respectively. This ratio represents the flow resistance experienced by the refrigerant as it passes through the compressor valves. Least squares is used to estimate the coefficients of the mass flow models. The data sets obtained from the test stand built at MI and from (Gayeski, 2010; Gayeski et al., 2010) are used in the evaluation of constants. A comparison of the two mass flow rate models along with a combined model for the experimental data is given in Table 3.1:

Table 3.1: Comparison of mass flow rate models

| | **(Zakula, 2010)** | | **(Willingham, 2009)** | | **Combined** | |
|---|---|---|---|---|---|---|
| | **Coefficient** | **t-statistics** | **Coefficient** | **t-statistics** | **Coefficient** | **t-statistics** |
| C1 $V_{swept}$ ($m^3$) | 8.398E-06 | 4.604E+08 | 7.750E-06 | 4.320E+08 | 8.555E-06 | 2.581E+08 |
| C2 $V_{clearance}$ (%) | 1.132E-02 | 6.809E+02 | 1.084E-02 | 8.980E+01 | 6.570E-10 | 2.445E+01 |
| C3 $Suction_{resistance}$ ($m^2$) | — | — | 2.372E-14 | 4.591E-07 | 1.233E-04 | 8.714E+03 |
| C4 $Discharge_{resistance}$ ($m^2$) | — | — | 2.220E-14 | 8.873E-10 | 2.223E-14 | 7.543E-09 |
| C5 Back flow ($m^3/kPa.s$) | 2.016E-05 | 1.403E+06 | — | — | 2.534E-05 | 8.019E+05 |
| RMSPE % (RMSE (kg/s)) | 8.58 (9.977E-04) | | 10.41 (1.052E-03) | | 8.49 (9.940E-04) | |

It can be observed from Table 3.1 that mass flow model of (Zakula, 2010) and the combined model is in good agreement with the experimental data. The displacement volume estimated by the least squares is close to actual displacement volume obtained from the manufacturer which is 9.2e-6m$^3$. The flow resistance coefficients for both suction and discharge valves for the model of (Willingham, 2009) are almost negligible. However, the flow resistance coefficient for suction valve in the combined model is significant. F-test is performed to assess the combined model significance as compared to model of (Zakula, 2010). The F-statistics value was 0.965 and its significance was computed to be 0.382 which is greater than 0.05. Therefore, mass flow model of (Zakula, 2010) is used in the compressor model.

A model for calculation of thermodynamic compressor power is suggested in (Jähnig et al., 2000) to account for the electrical-mechanical conversion and mechanical losses in the compressor. In (Zakula, 2010), modification is made to the model in which $\eta_{comb}$ is taken as a function of pressure ratio instead of suction pressure. It is given in Equations 3.3.10-3.3.11:

$$\text{Compressor Power} * \eta_{comb} = \dot{m}_{ref-oil} * \frac{n}{n-1} * \frac{P_{suc}}{\rho_{suc}} * \left( \left( \frac{P_{dis}}{P_{suc}} \right)^{\frac{n-1}{n}} - 1 \right) \quad (3.3.10)$$

$$\eta_{comb} = C_6 + C_7 * \exp\left( C_8 * \left( \frac{P_{dis}}{P_{suc}} \right) \right) \quad (3.3.11)$$

Least squares is used to estimate the coefficients for the power model along with the mass model with the actual displacement volume specified. The coefficients and RMSE predicted by the model for the experimental data are given in Table 3.2:

Table 3.2: Coefficients and accuracy of mass and power models

| | |
|---|---|
| C1 $V_{swept}$ ($m^3$) | 9.200E-06 |
| C2 $V_{clearance\ fraction}$ (%) | 1.156E-01 |
| C5 Back flow ($m^3$/kPa. s) | 1.524E-05 |
| C6 | -9.001E-02 |
| C7 | 1.054E+00 |
| C8 | -1.592E-01 |
| RMSPE % (RMSE (kg/s)) | 13.16 (1.745E-03) |
| RMSPE % (RMSE (kW)) | 5.24 (1.897E-02) |

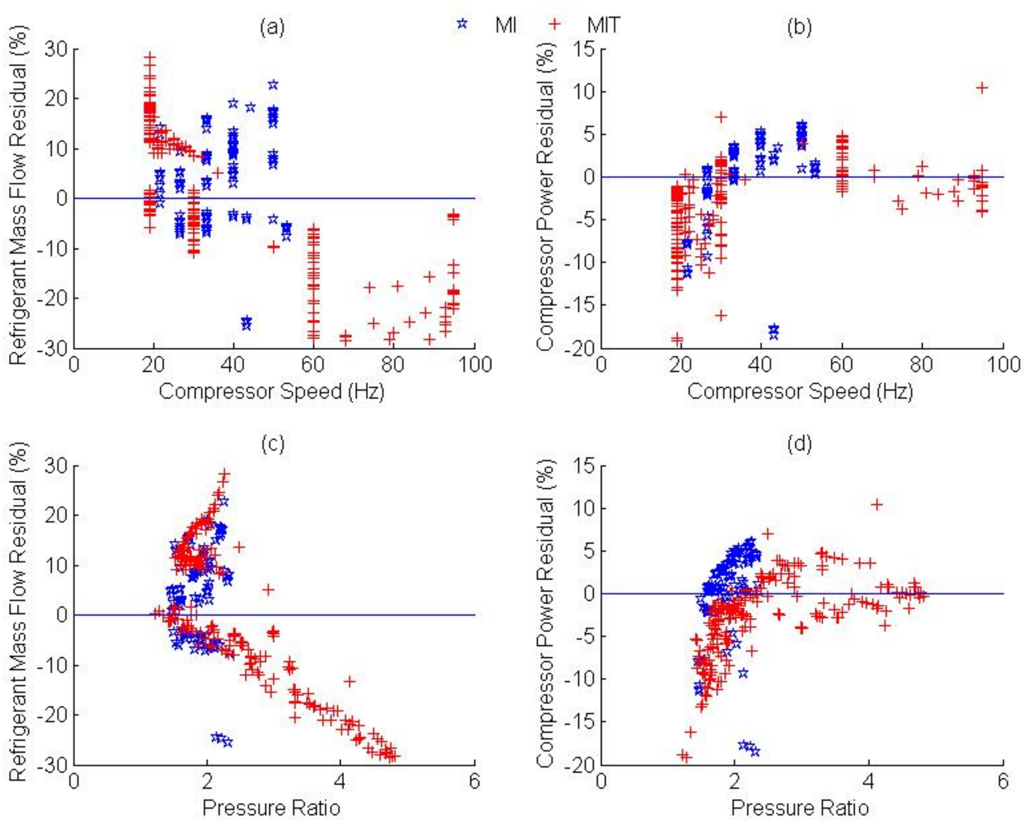


Figure 3.4: (a) Refrigerant mass flow residual vs. compressor speed (b) Compressor power residual vs. compressor speed (c) Refrigerant mass flow residual vs. pressure ratio (d) Compressor power residual vs. pressure ratio

Figure 3.4 shows the residuals of the power and mass flow model. It can be observed that for low compressor speeds, the residuals for mass flow rate are within ±15% for majority of data points. However, the mass flow model doesn't perform well for high pressure ratios occurring at high compressor speeds. It can be observed from Figure 3.5 that the combined electrical and mechanical efficiency of the compressor decreases considerably at high pressure ratios.

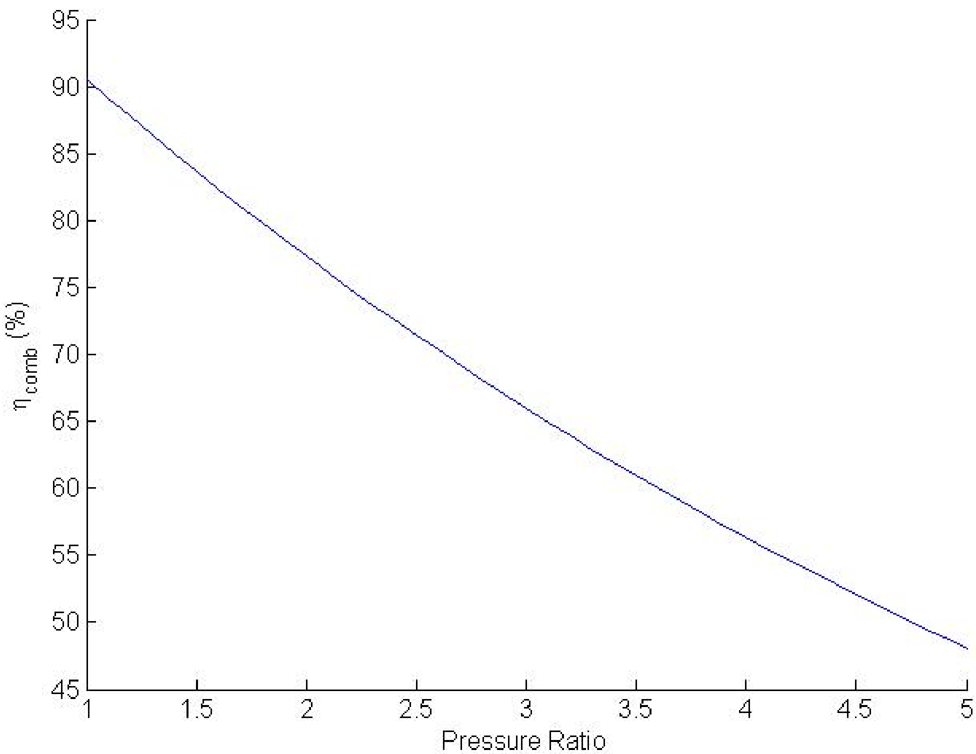


Figure 3.5: Illustration of $\eta_{comb}$ vs. pressure ratio

### 3.3.1 Compressor Model Description

The input and output parameters required for the compressor model are given in Table 3.3:

Table 3.3: Compressor model parameters

| **Input** | **Output** |
|---|---|
| $P_{dis}$ | $T_{dis}$ |
| $P_{suc}$ | $\dot{m}_{ref}$ |
| $Q_{load}$ | Compressor Power |
| $T_{suc}$ | $f_{comp}$ |
| $h_{evap_{in}}$ | |

For the given set of input parameters, MATLAB function 'lsqnonlin' is used to solve for compressor speed by searching $T_{dis}$. Convergence is achieved by satisfying Equation 3.3.12:

$$\text{Balance} = \text{Compressor Power} - Q_{comp} \qquad (3.3.12)$$

where,

$$Q_{comp} = \dot{m}_{ref-oil} * (h_{dis} - h_{suc}) \qquad (3.3.13)$$

The flow chart of the compressor model is given in Figure 3.6.

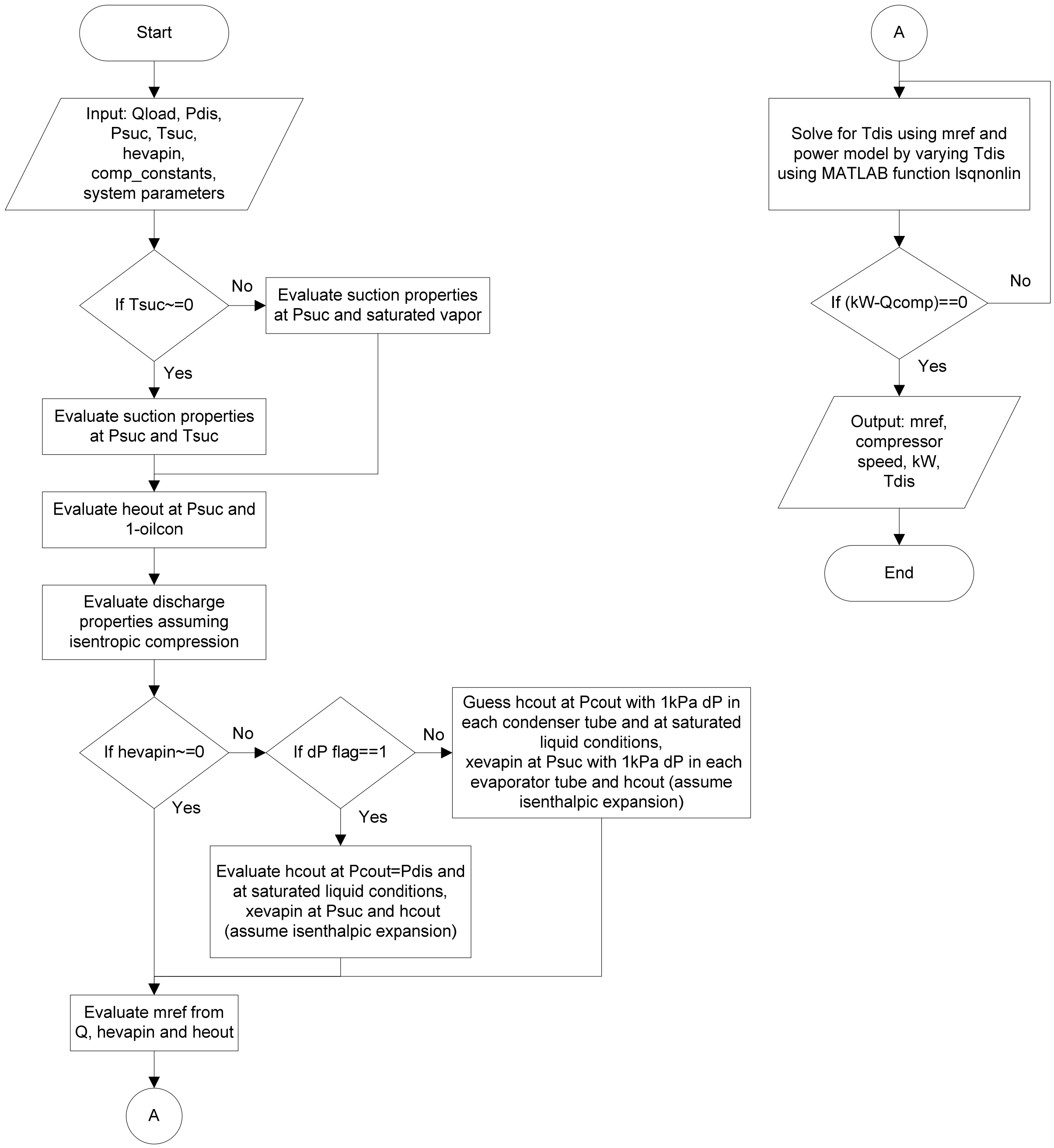


Figure 3.6: Compressor model flow chart

### 3.4 Fan-Coil Heat Exchanger Model

In this study, the tube-by-tube approach is used to model heat transfer and pressure drop in the HX. The HX is discretized according to the number of tubes in a loop and then heat transfer and pressure drop calculations are carried out in a progressive manner. For the transition between single-phase and two-phase heat transfer, the element length is changed to accurately identify the location of the transition. For the transition from single-phase to two-phase, the transition location is calculated to within ±0.01K accuracy while transition from two-phase to single-phase is calculated to within 1% of vapor quality. The lowest vapor quality in case of condenser is zero while in case of evaporator the maximum vapor quality is considered as ($1-\omega_{oil}$). The ±0.01K accuracy is considered due to limitation of refrigerant property calculation software.

In (Chen, C.-C. Wang, & S. Y. Lin, 2004; Chen, Wu, Chang, & C.-C. Wang, 2007), it is reported that the pressure drop in a U-bend is strongly influenced by the curvature of the U-bend characterized by two times the radius of curvature divided by diameter of tube *'2R/D'*. The pressure drop for U-bend with 2R/D equals to 3.91 (similar to the Fan-coil HX in our study whose '2R/D' equals 3.21) and has a circumferential length of 20mm is reported to be 2.5-3.5 times more than the pressure drop encountered in a straight section of 337mm for mass velocities of 300-400kg/$m^2$/s in the two-phase region (Chen et al., 2004). For our fan-coil HX, a pressure drop of 2.78kPa is incurred at a vapor quality of 90% for a mass velocity of 288kg/$m^2$/s in a straight section of 866mm which is 3.2Pa/mm. If we consider three times the pressure drop in the U-bends of our HX which has circumferential length of 33mm, the pressure drop in the U-bend is 0.3kPa which is only 10% of the total pressure drop occurring in a length of 866mm. No appreciable enhancement in the heat transfer coefficient was observed for U-bends with *'2R/D'* equals to 2.61 as reported in (Cho & Tae, 2001). Therefore, effect of U-bends on pressure drop and heat transfer is neglected in the present study.

The fan-coil HX considered in the present study are made up of round copper tubes with stamped aluminum plain fins joined together by mechanically expanding the tube as explained in ("The benefits of Aluminum in HVAC&R Heat Exchangers," 2011). In (Jeong, C. N. Kim, & Youn, 2006), contact resistance between different fan-coil HX is estimated. The different fan-coil HX consisted on different fin-types, methods of attaching fins to round tubes and whether a hydrophilic coating was applied to them. It was found that for all the 22 different cases, the contact resistance comprised of on average around 20% of the total heat transfer resistance which included the tube resistance, fin resistance and cold and hot-side single-phase water resistance. In case of two-phase heat transfer, the share of contact resistance in the total heat transfer resistance will further reduce. Therefore, in this study the effect of contact resistance is neglected.

The effects of physical arrangement of HX circuitry to the air flow are also neglected. The assumptions that are made for the fan-coil HX model are as follows:

- Uniform ambient/zone temperature
- Uniform air distribution over the HX
- Effect of U-bends on heat transfer and pressure drop is negligible
- Contact resistance between tube and fins is negligible
- Effect of air-side pressure drop on heat transfer is negligible
- HX circuitry arrangement effects on air-side heat transfer are negligible
- Radiation heat transfer effects are negligible
- Condensation or frosting on the outside of tubes is not considered

### 3.4.1 Fin Efficiency and Air-Side Heat Transfer Coefficient

The air-side heat transfer consists of outside air convection and heat transfer through fins. The mass flow velocity of air through an element is calculated from the total mass flow rate by using the surface area of the element which consists of fin and tube surface areas. Equation 3.4.1 is used for calculation of surface area:

$$A_{min_{air}} = P_{transverse} * L_{element} - \frac{L_{element}}{P_{fin}} * t_{fin} * P_{transverse} - D_c * L_{element} \qquad (3.4.1)$$

For calculating the fin efficiency, Schmidt method is used as suggested in (Perrotin & Clodic, 2003). In this method, the fin efficiency is calculated by considering an equivalent circular fin radius. Correlations are used to find the efficiency of the equivalent circular fin having the same efficiency as rectangular fin. The correlation for the rectangular fin is given in Equations 3.4.2-3.4.5:

$$\Psi = \left(\frac{R_{eq}}{r} - 1\right) * \left(1 + 0.35 * \ln\left(\frac{R_{eq}}{r}\right)\right) \qquad (3.4.2)$$

$$\frac{R_{eq}}{r} = 1.28 * \frac{X_m}{\frac{D_c}{2}} * \left(\frac{X_l}{X_m} - 0.2\right)^{0.5} \qquad (3.4.3)$$

$$X_l = \frac{P_{longitudinal}}{2} \qquad (3.4.4)$$

$$X_m = \frac{P_{transverse}}{2} \qquad (3.4.5)$$

The total surface efficiency for the element is then calculated through Equation 3.4.6:

$$\eta_{surf} = 1 - \frac{L_{element}}{P_{fin}} * \frac{A_{fin}}{A_{surf_{total}}} * \left(1 - \eta_{fin}\right) \qquad (3.4.6)$$

where,

$$\eta_{fin} = \tanh\left(\Psi * m * \left(\frac{D_c}{2}\right)\right) / \left(\Psi * m * \left(\frac{D_c}{2}\right)\right) \tag{3.4.7}$$

$$m = \left(\frac{2 * h_{conv_{out}}}{k_{fin} * t_{fin}}\right)^{0.5} \tag{3.4.8}$$

$$A_{tube_{in}} = \pi * D_{in} * L_{element} \tag{3.4.9}$$

$$A_{tube_{out}} = \pi * D_c * L_{element} \tag{3.4.10}$$

$$A_{fin} = 2 * \left(P_{transverse} * \left(P_{longitudinal} + \frac{t_{fin}}{2}\right) - \pi * \left(\frac{D_c}{2}\right)^2\right) \tag{3.4.11}$$

$$A_{surf_{total}} = A_{fin} * \frac{L_{element}}{P_{fin}} + A_{tube_{out}} \tag{3.4.12}$$

The air-side heat transfer coefficient is calculated from the correlation of Grey and Webb (Gray & Webb, 1986) which is given in Equation 3.4.13:

$$h_{conv_{out}} = j1 * G_{air} * cp_{air} / Pr_{air}^{\frac{2}{3}} \tag{3.4.13}$$

where,

$$j = 0.14 * Re^{-0.328} * \left(\frac{P_{transverse}}{P_{longitudinal}}\right)^{-0.502} * \left(\frac{P_{fin}}{D_c}\right)^{0.0312} \tag{3.4.14}$$

$$j1 = 0.991 * \left(2.24 * Re^{-0.092} * \left(\frac{tube_{row}}{4}\right)^{-0.031}\right)^{0.607} * (4 - tube_{row}) * j \tag{3.4.15}$$

### 3.4.2 Single-Phase Refrigerant Side Heat Transfer

The single-phase heat transfer at the refrigerant side is evaluated using Equation 3.4.16 or Equation 3.4.17:

$$Q = \varepsilon * C_{min} * dT \tag{3.4.16}$$

$$Q = \dot{m} * cp * (T_{out} - T_{in}) \tag{3.4.17}$$

where,

$$dT = T_{tube_{in}} - T_x \text{ (for condenser)} \tag{3.4.18}$$

$$dT = T_z - T_{tube_{in}} \text{ (for evaporator)} \tag{3.4.19}$$

$$C = \dot{m} * cp \tag{3.4.20}$$

$$\varepsilon = 1 - \exp\left(\frac{1}{C_r} * NTU^{0.22} * (\exp(-1 * C_r * NTU^{0.78}) - 1)\right) \tag{3.4.21}$$

$$C_r = C_{min}/C_{max} \tag{3.4.22}$$

$$NTU = UA/C_{min} \tag{3.4.23}$$

$$UA = \left(\frac{1}{h_{conv_{in}} * A_{tube_{in}}} + \frac{\log\left(\frac{D_c}{D_{in}}\right)}{2 * \pi * k_{tube} * L} + \frac{1}{\eta_{surf} * h_{conv_{out}} * A_{surf_{total}}}\right)^{-1} \tag{3.4.24}$$

The single-phase heat transfer coefficient for the refrigerant side is calculated based on turbulent flow correlation. The heat transfer coefficient is calculated from Equation 3.4.25 (Gnielinski, 1976):

$$h_{conv_{in}} = \frac{\frac{f}{2} * (Re - 1000) * Pr_{\,ref-oil}}{1 + 12.7 * \left(\frac{f}{2}\right)^{0.5} * \left(Pr_{ref-oil}^{\frac{2}{3}} - 1\right)} * \frac{k_{ref-oil}}{D_{in}} \tag{3.4.25}$$

### 3.4.3 Single-Phase Refrigerant-Side Pressure Drop

The single-phase pressure drop is calculated through the Darcy-Weisbach equation which is given in Equation 3.4.26:

$$\frac{dp}{dx} = 2 * f * L_{element} * \frac{G^2}{D * \rho} \tag{3.4.26}$$

where, friction factor '$f$' is calculated using Equation 3.4.27 (Gnielinski, 1976):

$$f = (1.58 * \log(Re) - 3.28)^{-2} \tag{3.4.27}$$

### 3.4.4 Flow Pattern Map

The flow pattern map developed for refrigerants by (Wojtan, Ursenbacher, & Thome, 2005a) is used to calculate the heat transfer coefficient and pressure drop for two-phase flow. Figure 3.7 shows the different two-phase flow regimes for a heat flux of 5kW/$m^2$, mass velocity of 300kg/$m^2$/s and saturation temperature of 24°C. It is to be noted that during condensation phase there is no dryout or mist region.

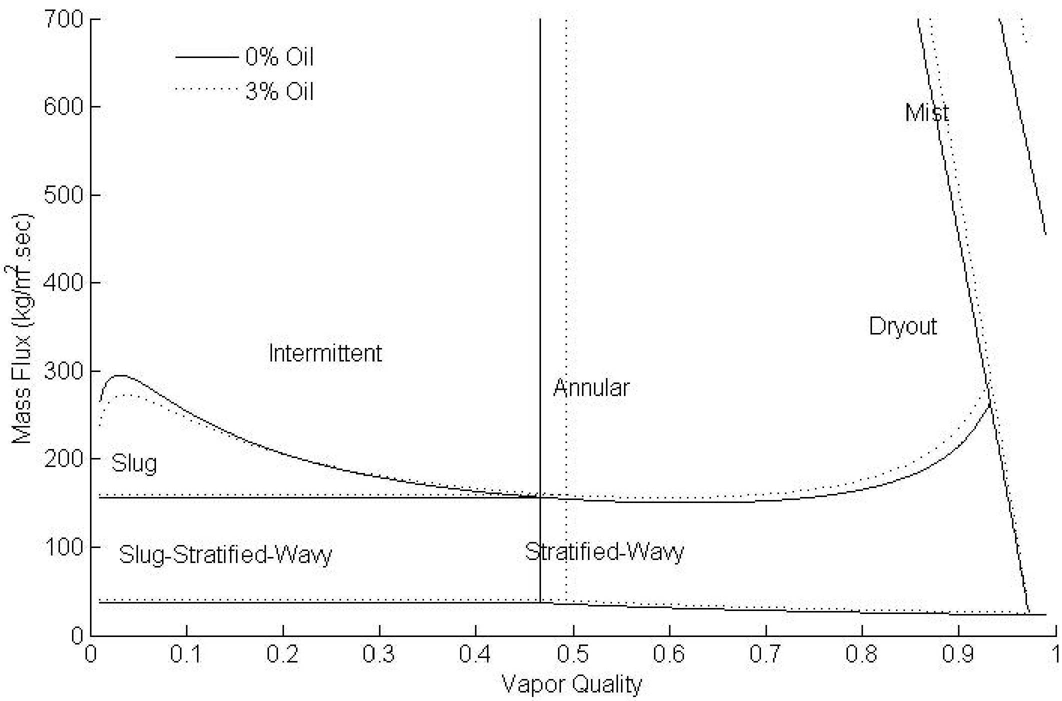


Figure 3.7: Two-phase flow pattern map (Wojtan, Ursenbacher, & Thome, 2005a)

To describe the properties of refrigerant in the two-phase flow, void fraction is calculated using the Rouhani-Axelsson drift flux model. This void fraction determines the ratio of volumetric rate of vapor passing through an area to the rate of fluid passing through it (Thome, 2004). Equation 3.4.28 is used to calculate the void fraction:

$$e = \frac{x_{in}}{\rho_{ref_g}} * \left( \left(1 + 0.12 * (1 - x_{in})\right) * \left(\frac{x_{in}}{\rho_{ref_g}} + \frac{1 - x_{in}}{\rho_{ref_{liq}}}\right) + \frac{1.18 * (1 - x_{in}) * \left(9.8 * \sigma_{ref} * \left(\rho_{ref_{liq}} - \rho_{ref_g}\right)\right)^{0.25}}{G_{ref} * \rho_{ref_{liq}}^{0.5}} \right)^{-1} \tag{3.4.28}$$

The liquid and vapor velocities, dimensionless areas, heights and stratification angle are calculated from Equation 3.4.29-3.4.34:

$$v_{liq} = \frac{G_{ref}}{\rho_{ref_{liq}}} * \frac{1 - x_{in}}{1 - e} \tag{3.4.29}$$

$$v_g = \frac{G_{ref}}{\rho_{ref_g}} * \frac{x_{in}}{e} \tag{3.4.30}$$

$$A_{liqD} = (1 - e) * \frac{\pi}{4} \tag{3.4.31}$$

$$A_{gD} = e * \frac{\pi}{4} \tag{3.4.32}$$

$$h_{liqD} = 0.5 * \left(1 - \cos\left(\frac{2\pi - \theta_{strat}}{2}\right)\right) \tag{3.4.33}$$

$$\theta_{strat} = 2\pi - 2 * \left(\pi(1 - e) + \left(\frac{3\pi}{2}\right)^{\frac{1}{3}} * \left(1 - 2 * (1 - e) + (1 - e)^{\frac{1}{3}} - e^{\frac{1}{3}}\right) - \frac{1}{200} * (1 - e) * e * \left(1 - 2 * (1 - e)\right) * \left(1 + 4 * ((1 - e)^2 + e^2)\right)\right) \tag{3.4.34}$$

The boundaries shown in Figure 3.7 are identified using mass fluxes and vapor quality. Equations 3.4.35-3.4.39 are used to calculate the mass flux boundaries:

$$G_{strat} = \left(\frac{226.3^2 * A_{liqD} * A_{gD}^2 * \rho_{ref_g} * \left(\rho_{ref_{liq}} - \rho_{ref_g}\right) * \mu_{ref_{liq}} * 9.8}{x_{in}^2 * (1 - x_{in}) * \pi^3}\right)^{\frac{1}{3}} \tag{3.4.35}$$

If $x_{in} < x_{IA}, G_{strat} = G_{strat}(x_{IA})$

$$G_{wavy} = \left( \left( \frac{16 * A_{gD}^3 * 9.8 * D_{in} * \rho_{ref_{liq}} * \rho_{ref_g}}{x_{in}^2 * \pi^2 * \left(1 - \left(2 * h_{liqD} - 1\right)^2\right)^{0.5}} \right) * \left( \frac{\pi^2}{25 * h_{liqD}^2} * \left(WeFr_{liq}\right)^{-1} + 1 \right) \right)^{0.5} + 50 \quad (3.4.36)$$

where,

$$WeFr_{liq} = 9.8 * D_{in}^2 * \frac{\rho_{ref_{liq}}}{\sigma_{ref}} \quad (3.4.37)$$

$$G_{dryout} = \left( \frac{1}{0.235} * \left( \ln\left(\frac{0.58}{x_{in}}\right) + 0.52 \right) * \left( \frac{D_{in}}{\rho_{ref_g} * \sigma_{ref}} \right)^{-0.17} * \left(9.8 * D_{in} * \rho_{ref_g} * \left(\rho_{ref_{liq}} - \rho_{ref_g}\right)\right)^{0.37} * \left(\frac{\rho_{ref_g}}{\rho_{ref_{liq}}}\right)^{-0.25} * \left(\frac{q_{flux}}{q_{crit}}\right)^{-0.7} \right)^{0.926} \quad (3.4.38)$$

If $G_{strat} > G_{dryout}$, $G_{dryout} = G_{strat}$; If $G_{wavy} > G_{dryout}$, $G_{dryout} = G_{wavy}$

$$G_{mist} = \left( \frac{1}{0.0058} * \left( \ln\left(\frac{0.61}{x_{in}}\right) + 0.57 \right) * \left( \frac{D_{in}}{\rho_{ref_g} * \sigma_{ref}} \right)^{-0.38} * \left(9.8 * D_{in} * \rho_{ref_g} * \left(\rho_{ref_{liq}} - \rho_{ref_g}\right)\right)^{0.15} * \left(\frac{\rho_{ref_g}}{\rho_{ref_{liq}}}\right)^{0.09} * \left(\frac{q_{flux}}{q_{crit}}\right)^{-0.27} \right)^{0.943} \quad (3.4.39)$$

where,

$$q_{crit} = 0.131 * \rho_{ref_g}^{0.5} * h_{fg_{ref}} * \left(9.8 * \left(\rho_{ref_{liq}} - \rho_{ref_g}\right) * \sigma_{ref}\right)^{0.25} \quad (3.4.40)$$

If $G_{dryout} > G_{mist}$, $G_{mist} = G_{dryout}$

The formula for calculation of intermittent-annular transition vapor quality is given by Equation 3.4.41:

$$x_{IA} = \left(\left(0.2914 * \left(\frac{\rho_{\mathrm{ref_g}}}{\rho_{\mathrm{ref_{liq}}}}\right)^{-\left(\frac{1}{1.75}\right)} * \left(\frac{\mu_{\mathrm{ref_{liq}}}}{\mu_{\mathrm{ref_g}}}\right)^{-\left(\frac{1}{7}\right)}\right) + 1\right)^{-1} \quad (3.4.41)$$

The vapor quality to identify start of dryout region is calculated by Equation 3.4.42:

$$\mathrm{x_{dryout_{start}}} = 0.58 * \exp\left(0.52 - 0.235 * \mathrm{We_g^{0.17}} * \mathrm{Fr_g^{0.37}} * \left(\frac{\rho_{\mathrm{ref_g}}}{\rho_{\mathrm{ref_{liq}}}}\right)^{0.25} * \left(\frac{\mathrm{q_{flux}}}{\mathrm{q_{crit}}}\right)^{0.7}\right) \quad (3.4.42)$$

where,

$$\mathrm{We_g} = \mathrm{G_{ref}^2} * \frac{\mathrm{D_{in}}}{\rho_{\mathrm{ref_g}} * \sigma_{\mathrm{ref}}} \quad (3.4.43)$$

$$\mathrm{Fr_g} = \frac{\mathrm{G_{ref}^2}}{9.8 * \mathrm{D_{in}} * \rho_{\mathrm{ref_g}}^2} \quad (3.4.44)$$

The vapor quality to identify end of dryout region is calculated by Equation 3.4.45:

$$\mathrm{x_{dryout_{end}}} = 0.61 * \exp\left(0.57 - 5.8 * 10^{-3} * \mathrm{We_g^{0.38}} * \mathrm{Fr_g^{0.15}} * \left(\frac{\rho_{\mathrm{ref_g}}}{\rho_{\mathrm{ref_{liq}}}}\right)^{-0.09} * \left(\frac{\mathrm{q_{flux}}}{\mathrm{q_{crit}}}\right)^{0.27}\right) \quad (3.4.45)$$

These equations are then used to identify the flow regimes shown in Figure 3.7 based on the following:

– Slug

$$\mathrm{G_{ref}} > \mathrm{G_{wavy}}(\mathrm{x_{IA}})$$

– Slug-Stratified-Wavy

$$\mathrm{G_{ref}} > \mathrm{G_{wavy}}(\mathrm{x_{IA}}) \text{ and } \mathrm{x_{in}} < \mathrm{x_{IA}} \text{and } \mathrm{G_{ref}} > \mathrm{G_{strat}}$$

– Stratified-Wavy

$$x_{in} > x_{IA}$$

– Stratified

$$G_{ref} > G_{strat}$$

– Intermittent

$$G_{ref} > G_{wavy} \text{ and } x_{in} < x_{IA}$$

– Annular

$$G_{ref} > G_{wavy} \text{ and } x_{in} > x_{IA}$$

– Dryout

$$G_{ref} > G_{dryout} \text{ and } x_{in} > x_{dryout_{start}}$$

– Mist

$$G_{ref} > G_{mist} \text{ and } x_{in} > x_{dryout_{end}}$$

### 3.4.5 Two-Phase Refrigerant-Side Heat Transfer

The two-phase heat transfer at the refrigerant side is evaluated using Equation 3.4.16 or Equation 3.4.46:

$$Q = \dot{m} * h_{fg_{ref}} * (x_{out} - x_{in}) \tag{3.4.46}$$

The terms in Equation 3.4.16 for two-phase heat transfer are described in Equations 3.4.47-3.4.49:

$$dT = T_{bulb} - T_x \text{ (for condenser)} \tag{3.4.47}$$

$$dT = T_z - T_{bulb} \text{ (for evaporator)} \tag{3.4.48}$$

$$\varepsilon = 1 - \exp(-\mathrm{NTU}) \tag{3.4.49}$$

The heat transfer coefficient for different flow regimes during condensation is calculated using Equations 3.4.50-3.4.52:

$$h_{conv_{in}} == \frac{h_{filmcond} * \theta_{strat-wavy} + \left(2 * \pi - \theta_{strat-wavy}\right) * h_{annular}}{2 * \pi} \tag{3.4.50}$$

$$h_{filmcond} = 0.655 * \left(\rho_{ref_{liq}} * \left(\rho_{ref_{liq}} - \rho_{ref_g}\right) * 9.8 * h_{fg_{ref}} * \frac{k_{ref_{liq}}^3}{\mu_{ref_{liq}} * D_{in} * q_{flux}}\right)^{\frac{1}{3}} \tag{3.4.51}$$

$$h_{annular} = 0.003 * Re_{liq}\,\hat{}\,0.74 * Pr_{ref_{liq}}^{0.5} * \frac{k_{ref_{liq}}}{\delta_{liqfilm}} * f_i \tag{3.4.52}$$

where,

$$Re_{liq} = 4 * G_{ref} * (1 - x_{in}) * \frac{\delta_{liqfilm}}{(1 - e) * \mu_{ref_{liq}}} \tag{3.4.53}$$

$$\delta_{liqfilm} = \frac{D_{in}}{2} - \left(\left(\frac{D_{in}}{2}\right)^2 - \frac{2 * A_{liqD} * D_{in}^2}{2 * \pi - \theta_{strat-wavy}}\right)^{0.5} \tag{3.4.54}$$

If $\delta_{liqfilm} > D_{in}/2, \delta_{liqfilm} = D_{in}/2$

$$f_i = 1 + \left(\frac{v_g}{v_{liq}}\right)^{0.5} * \left(\left(\rho_{ref_{liq}} - \rho_{ref_g}\right) * 9.8 * \frac{\delta_{liqfilm}^2}{\sigma_{ref}}\right)^{0.25} \tag{3.4.55}$$

If $G_{ref} < G_{strat}, f_i = f_i * (G_{ref}/G_{strat})$

The heat transfer coefficient for different flow regimes during evaporation excluding dryout and mist flow regimes is calculated using Equations 3.4.56-3.4.60:

$$h_{conv_{in}} = \frac{h_{vapor} * \theta_{strat-wavy} + \left(2 * \pi - \theta_{strat-wavy}\right) * h_{liq}}{2 * \pi} \tag{3.4.56}$$

$$h_{vapor} = 0.023 * \left(G_{ref} * x_{in} * \frac{D_{in}}{e * \mu_{ref_g}}\right)^{0.8} * Pr_{ref_g}^{0.4} * \frac{k_{ref_g}}{D_{in}} \tag{3.4.57}$$

$$h_{liq} = \left((0.8 * h_{nucboil})^3 + h_{convboil}^3\right)^{\frac{1}{3}} \tag{3.4.58}$$

$$h_{nucboil} = 55 * P_{reduced}^{0.12} * \left(-\log10(P_{reduced})\right)^{-0.55} * M^{-0.5} * q_{flux}^{0.67} \tag{3.4.59}$$

$$h_{convboil} = 0.0133 * Re_{liq}^{0.69} * Pr_{ref_{liq}}^{0.4} * \frac{k_{ref_{liq}}}{\delta_{liqfilm}} \tag{3.4.60}$$

where,

$$P_{reduced} = \frac{P_{sat}}{P_{critical}} \tag{3.4.61}$$

For $R - 410a$: $P_{critical} = 4.9MPa$; $M = 72.585 g/mol$

The $\theta_{strat\text{-}wavy}$ for different flow regimes excluding dryout and mist flow regimes is given as:

- Slug

$$\theta_{strat-wavy} = 0$$

- Slug-Stratified-Wavy

$$\theta_{strat-wavy} = \theta_{strat} * \frac{x_{in}}{x_{IA}} * \left(\frac{G_{wavy} - G_{ref}}{G_{wavy} - G_{strat}}\right)^{0.61}$$

- Stratified-Wavy

$$\theta_{strat-wavy} = \theta_{strat} * \left(\frac{G_{wavy} - G_{ref}}{G_{wavy} - G_{strat}}\right)^{0.61}$$

- Stratified

$$\theta_{strat-wavy} = \theta_{strat}$$

- Intermittent

$$\theta_{strat-wavy} = 0$$

– Annular

$$\theta_{\mathrm{strat-wavy}} = 0$$

For the mist flow regime, the heat transfer coefficient is given by Equation 3.4.62:

$$\mathrm{h}_{\mathrm{conv_{in}}} = 0.0117 * \mathrm{Re}_{\mathrm{Homo}}^{.79} * \mathrm{Pr}_{\mathrm{ref_g}}^{1.06} * \mathrm{Y}^{-1.83} * \frac{\mathrm{k}_{\mathrm{ref_g}}}{\mathrm{D}_{\mathrm{in}}} \tag{3.4.62}$$

where,

$$\mathrm{Re}_{\mathrm{Homo}} = \mathrm{G}_{\mathrm{ref}} * \frac{\mathrm{D}_{\mathrm{in}}}{\mu_{\mathrm{ref_g}}} * \left(\mathrm{x}_{\mathrm{in}} + \frac{\rho_{\mathrm{ref_g}}}{\rho_{\mathrm{ref_{liq}}}} * (1 - \mathrm{x}_{\mathrm{in}})\right) \tag{3.4.63}$$

$$\mathrm{Y} = 1 - 0.01 * \left(\left(\frac{\rho_{\mathrm{ref_{liq}}}}{\rho_{\mathrm{ref_g}}} - 1\right) * (1 - \mathrm{x}_{\mathrm{in}})\right)^{0.4} \tag{3.4.64}$$

For the dryout flow regime, the heat transfer coefficient is calculated using Equation 3.4.65:

$$\begin{aligned} \mathrm{h}_{\mathrm{conv_{in}}} = \mathrm{h}_{\mathrm{conv_{in}}}\left(\mathrm{x}_{\mathrm{dryout_{start}}}\right) - \frac{\mathrm{x}_{\mathrm{in}} - \mathrm{x}_{\mathrm{dryout_{start}}}}{\mathrm{x}_{\mathrm{dryout_{end}}} - \mathrm{x}_{\mathrm{dryout_{start}}}} \\ * \left(\mathrm{h}_{\mathrm{conv_{in}}}\left(\mathrm{x}_{\mathrm{dryout_{start}}}\right) - \mathrm{h}_{\mathrm{conv_{in}}}\left(\mathrm{x}_{\mathrm{dryout_{end}}}\right)\right) \end{aligned} \tag{3.4.65}$$

$\mathrm{h}_{\mathrm{conv_{in}}}\left(\mathrm{x}_{\mathrm{dryout_{start}}}\right)$ is evaluated from the $\mathrm{h}_{\mathrm{conv_{in}}}$ applicable to flow regimes other than mist while $\mathrm{h}_{\mathrm{conv_{in}}}\left(\mathrm{x}_{\mathrm{dryout_{end}}}\right)$ is evaluated from the $\mathrm{h}_{\mathrm{conv_{in}}}$ applicable to mist flow regime.

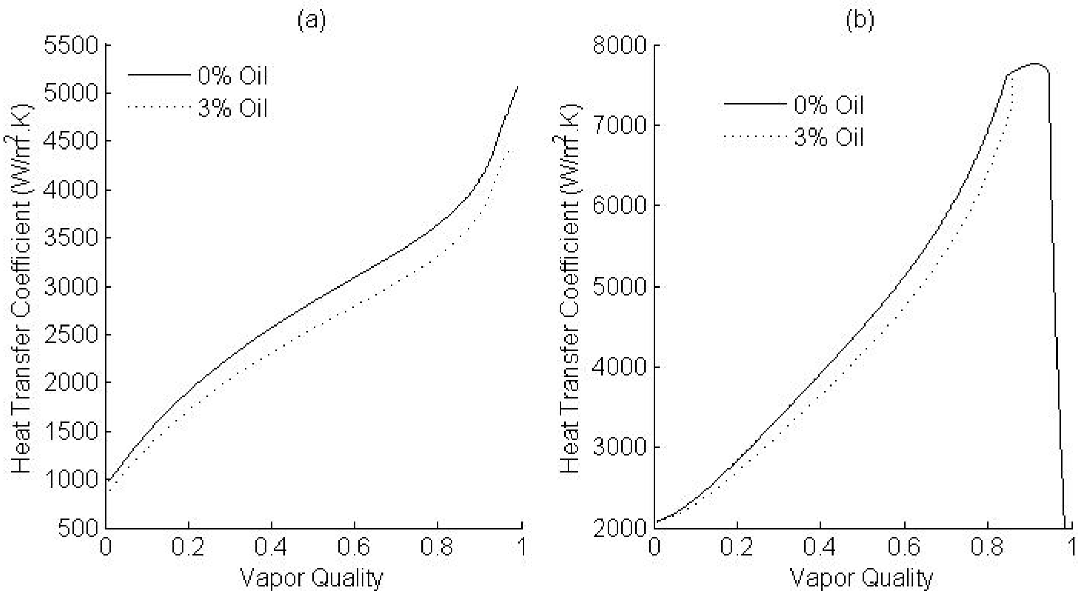


Figure 3.8: (a) Condensation heat transfer model (b) Evaporation heat transfer model

The heat transfer coefficient variation over the two-phase region along with oil effect on heat transfer coefficient is illustrated in Figure 3.8 for condensation and evaporation for a heat flux of 5kW/m$^2$, mass velocity of 300kg/m$^2$/s and saturation temperature of 24°C. The heat transfer coefficients for the dryout and mist flow regimes illustrated in Figure 3.8 are for pure refrigerant.

### 3.4.6 Two-Phase Refrigerant-Side Pressure Drop

The two-phase pressure drop is calculated using the correlation developed by (Moreno Quibén & Thome, 2007b). The equations for the different flow regimes are given as:

– Slug

$$\frac{dP}{dx} = 2 * f_{liq} * L_{element} * \frac{(G_{ref})^2}{D_{in} * \rho_{ref_{liq}}} * \left(1 - \frac{e}{e(x_{IA})}\right)^{0.25} + 2 * f_{annular} * L_{element} * \rho_{ref_g} * \frac{v_g^2}{D_{in}} * \left(\frac{e}{e(x_{IA})}\right)^{0.25} \tag{3.4.66}$$

where,

$$f_{liq} = \left(1.58 * \ln\left(Re_{liq}\right) - 3.28\right)^{-2} \tag{3.4.67}$$

$$f_{annular} = 0.67 * \left(\frac{\delta_{liqfilmannular}}{D_{in}}\right)^{1.2} * \left(\left(\rho_{ref_{liq}} - \rho_{ref_g}\right) * 9.8 * \frac{\delta_{liqfilmannular}^2}{\sigma_{ref}}\right)^{-0.4} * \left(\frac{\mu_{ref_g}}{\mu_{ref_{liq}}}\right)^{0.08} * We_{liq}{}^{-0.034} \tag{3.4.68}$$

$$\delta_{liqfilmannular} = D_{in} * \frac{1 - e}{4 * \pi} \tag{3.4.69}$$

$$We_{liq} = \rho_{ref_{liq}} * v_{liq}^2 * \frac{D_{in}}{\sigma_{ref}} \tag{3.4.70}$$

– Slug-Stratified-Wavy

$$\frac{dP}{dx} = 2 * f_{liq} * \frac{L_{element}}{D_{in} * \rho_{ref_{liq}}} * (G_{ref})^2 * \left(1 - \frac{e}{e(x_{IA})}\right)^{0.25} + 2 * f_{strat-wavy} * L_{element} * \rho_{ref_g} * \frac{v_g^2}{D_{in}} * \left(\frac{e}{e(x_{IA})}\right)^{0.25} \tag{3.4.71}$$

$$f_{strat-wavy} = \frac{\theta_{strat-wavy}}{2 * \pi} * f_g + \left(1 - \frac{\theta_{strat-wavy}}{2 * \pi}\right) * f_{annular} \tag{3.4.72}$$

$$f_g = \frac{0.079}{Re_g^{0.25}} \tag{3.4.73}$$

$$Re_g = G_{ref} * \frac{D_{in}}{\mu_{ref_g}} * \frac{x_{in}}{e} \tag{3.4.74}$$

– Stratified-Wavy

$$\frac{dP}{dx} = 2 * f_{stratwavy} * L_{element} * \rho_{ref_g} * \frac{v_g^2}{D_{in}} \tag{3.4.75}$$

– Stratified

$$\frac{dP}{dx} = 2 * f_{strat} * L_{element} * \rho_{ref_g} * \frac{v_g^2}{D_{in}} \tag{3.4.76}$$

$$f_{strat} = \frac{\theta_{strat}}{2 * \pi} * f_g + \left(1 - \frac{\theta_{strat}}{2 * \pi}\right) * f_{annular} \tag{3.4.77}$$

If $x_{in} < x_{IA}$

$$\frac{dP}{dx} = 2 * f_{liq} * \frac{L_{element}}{D_{in} * \rho_{ref_{liq}}} * (G_{ref})^2 * \left(1 - \frac{e}{e(x_{IA})}\right)^{0.25} + 2 * f_{strat-wavy} * L_{element} * \rho_{ref_g} * \frac{v_g^2}{D_{in}} * \left(\frac{e}{e(x_{IA})}\right)^{0.25} \tag{3.4.78}$$

– Intermittent

$$\frac{dP}{dx} = 2 * f_{liq} * L_{element} * \frac{(G_{ref})^2}{D_{in} * \rho_{ref_{liq}}} * \left(1 - \frac{e}{e(x_{IA})}\right)^{0.25} + 2 * f_{annular} * L_{element} * \rho_{ref_g} * \frac{v_g^2}{D_{in}} * \left(\frac{e}{e(x_{IA})}\right)^{0.25} \tag{3.4.79}$$

– Annular

$$\frac{dP}{dx} = 2 * f_{annular} * L_{element} * \rho_{ref_g} * \frac{v_g^2}{D_{in}} \tag{3.4.80}$$

– Mist

$$\frac{dP}{dx} = 2 * f_{mist} * L_{element} * \frac{G_{ref}^2}{D_{in} * \rho_{ref_{homo}}} \tag{3.4.81}$$

$$\rho_{ref_{homo}} = \rho_{ref_{liq}} * (1 - e_h) + \rho_{ref_g} * e_h \tag{3.4.82}$$

$$e_h = \frac{1}{1 + \left(\frac{1 - x_{in}}{x_{in}} * \left(\frac{\rho_{ref_g}}{\rho_{ref_{liq}}}\right)\right)} \tag{3.4.83}$$

$$f_{mist} = \frac{0.079}{Re_{mist}^{0.25}} \tag{3.4.84}$$

$$Re_{mist} = G_{ref} * \frac{D_{in}}{x_{in} * \mu_{ref_g} + (1 - x_{in}) * \mu_{ref_{liq}}} \tag{3.4.85}$$

– Dryout

$$\frac{dP}{dx} = \frac{dP}{dx}\left(x_{dryout_{start}}\right) - \frac{x_{in} - x_{dryout_{start}}}{x_{dryout_{end}} - x_{dryout_{start}}}\left(\frac{dP}{dx}\left(x_{dryout_{start}}\right) - \frac{dP}{dx}\left(x_{dryout_{end}}\right)\right) \tag{3.4.86}$$

$\frac{dP}{dx}\left(x_{dryout_{start}}\right)$ is evaluated from the $\frac{dP}{dx}$ applicable to annular flow regime while $\frac{dP}{dx}\left(x_{dryout_{end}}\right)$ is evaluated from the $\frac{dP}{dx}$ applicable to mist flow regime.

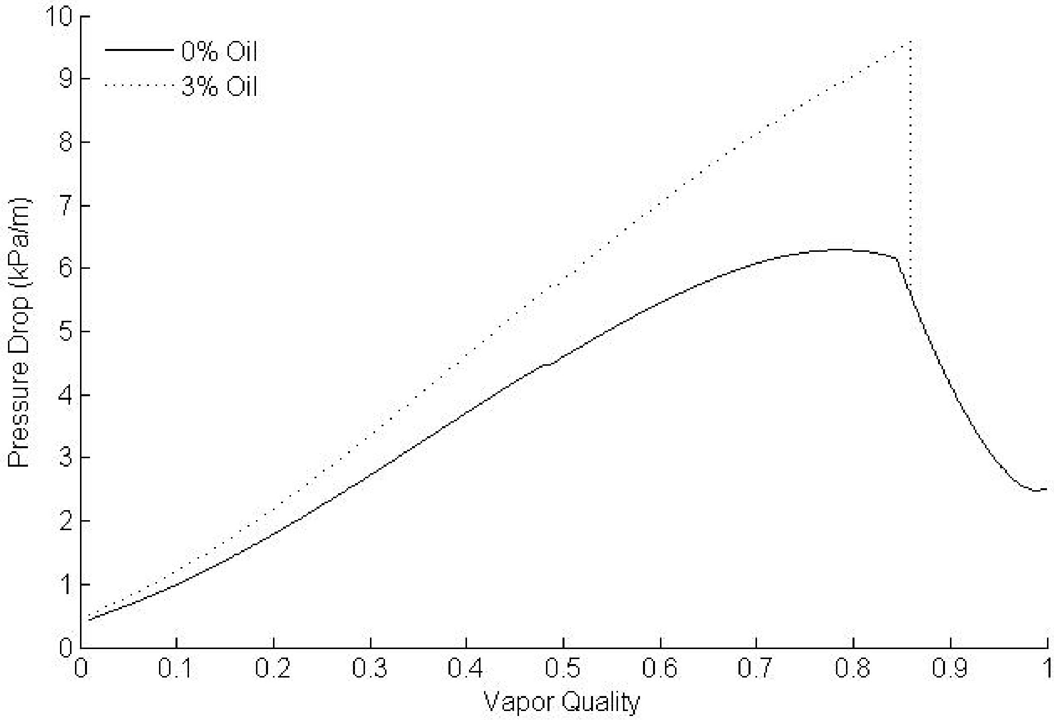


Figure 3.9: Pressure drop model

Figure 3.9 illustrates the variation in pressure drop in the two-phase region for evaporation along with effect of oil for a heat flux of $5kW/m^2$, mass velocity of $300kg/m^2/s$ and saturation temperature of 24°C. The pressure drop for the dryout and mist flow regimes illustrated in Figure 3.9 is for pure refrigerant.

### 3.4.7 Condenser Model Description

The input and output parameters that are required for the condenser model is given in Table 3.4 and

Table 3.5:

Table 3.4: Condenser model parameters

| **Input** | **Output** |
|---|---|
| $\dot{m}_{ref}$ | $\dot{V}_{air_{cond}}$ |
| $Q_{load}$ | $T_{cond_{out}}$ |
| kW | $P_{cond_{out}}$ |
| $T_{dis}$ | De-superheating zone fraction |
| $P_{dis}$ | Condensation zone fraction |
| Condenser details | Condenser Effectiveness |
| System details | Estimated $P_{evap_{in}}$, $T_{evap_{in}}$, $x_{evap_{in}}$ |

Table 3.5: Condenser details required

| | |
|---|---|
| Tube diameter | Tube thermal conductivity |
| Tube thickness | Fin thickness |
| Tube length | Fin width |
| Tube transversal pitch | Fin pitch |
| Total number of tubes | Fin thermal conductivity |
| Number of stream divisions | Condenser height |
| Number of tubes after streams merge | Condenser length |
| Number of tube rows | |

The system details are listed in section 3.6. For the given set of input parameters, $\dot{V}_{air_{cond}}$ is searched between its maximum and minimum limits using MATLAB function *'fmincon'* until convergence. The maximum and minimum limits in the present study are taken from the experimental data. The limits are:

Maximum $\dot{V}_{air_{cond}}$: 0.67 $m^3$/sec

Minimum $\dot{V}_{air_{cond}}$ : 0.2 $m^3$/sec

Convergence is achieved by satisfying Equation 3.4.87:

$$\text{Balance} = Q_{\text{load}} + \text{Compressor Power} - \text{sum}(Q_{\text{element}}) \qquad (3.4.87)$$

A multi-start point search algorithm is used to attain global minimum. In this algorithm, *'fmincon'* is supplied a set of linearly varying initial points defined between the maximum and minimum limits. The minimum of the balance from these points is taken as the final solution. The flow chart of the condenser model is given in Figure 3.10.

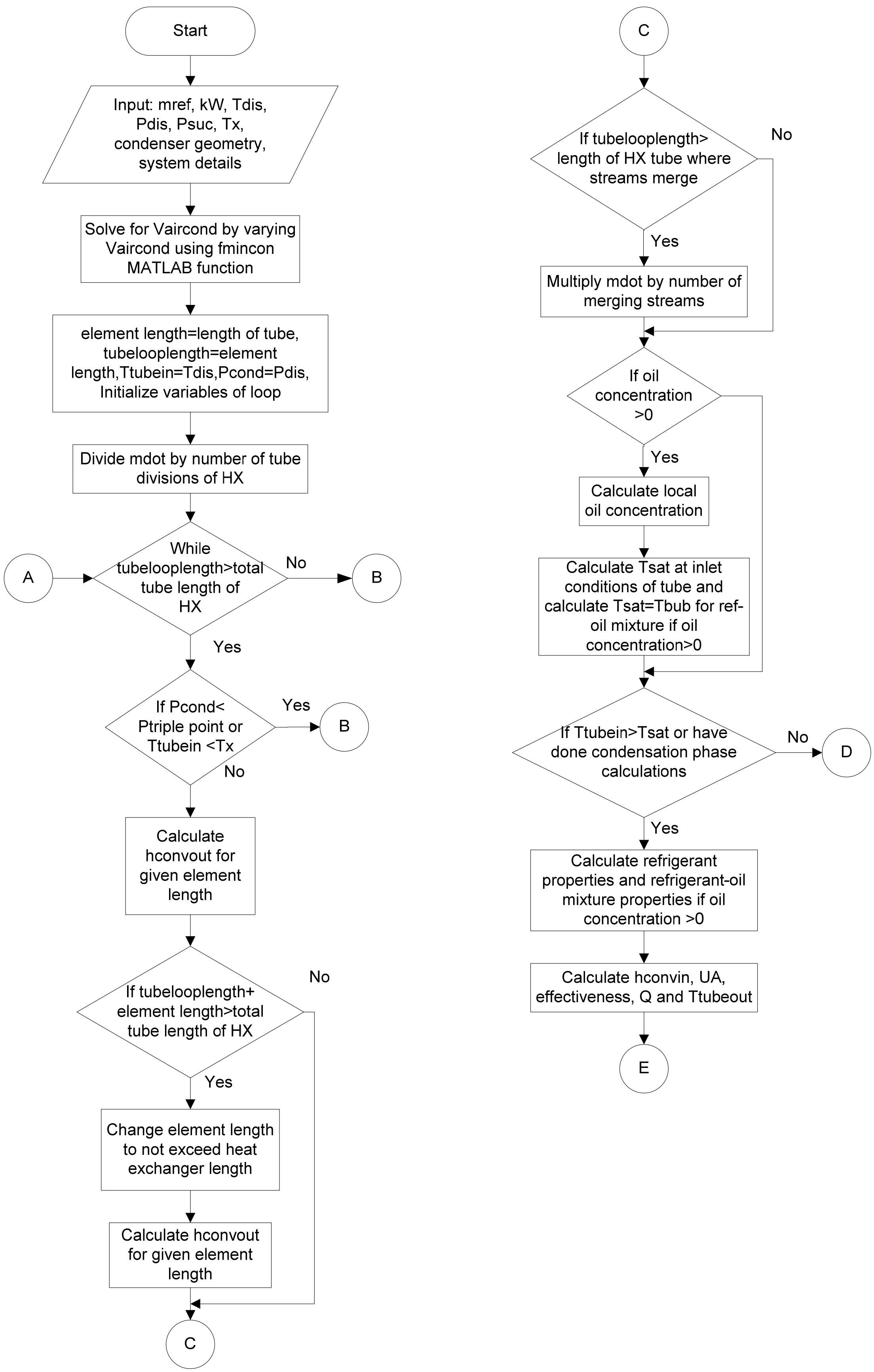
Start
Input: mref, kW, Tdis, Pdis, Psuc, Tx, condenser geometry, system details
Solve for Vaircond by varying Vaircond using fmincon MATLAB function
element length=length of tube, tubelooplength=element length,Ttubein=Tdis,Pcond=Pdis, Initialize variables of loop
Divide mdot by number of tube divisions of HX
A
While tubelooplength>total tube length of HX
No
B
Yes
If Pcond< Ptriple point or Ttubein <Tx
Yes
B
No
Calculate hconvout for given element length
If tubelooplength+ element length>total tube length of HX
No
Yes
Change element length to not exceed heat exchanger length
Calculate hconvout for given element length
C
C
If tubelooplength> length of HX tube where streams merge
No
Yes
Multiply mdot by number of merging streams
If oil concentration >0
Yes
Calculate local oil concentration
Calculate Tsat at inlet conditions of tube and calculate Tsat=Tbub for ref-oil mixture if oil concentration>0
If Ttubein>Tsat or have done condensation phase calculations
No
D
Yes
Calculate refrigerant properties and refrigerant-oil mixture properties if oil concentration >0
Calculate hconvin, UA, effectiveness, Q and Ttubeout
E

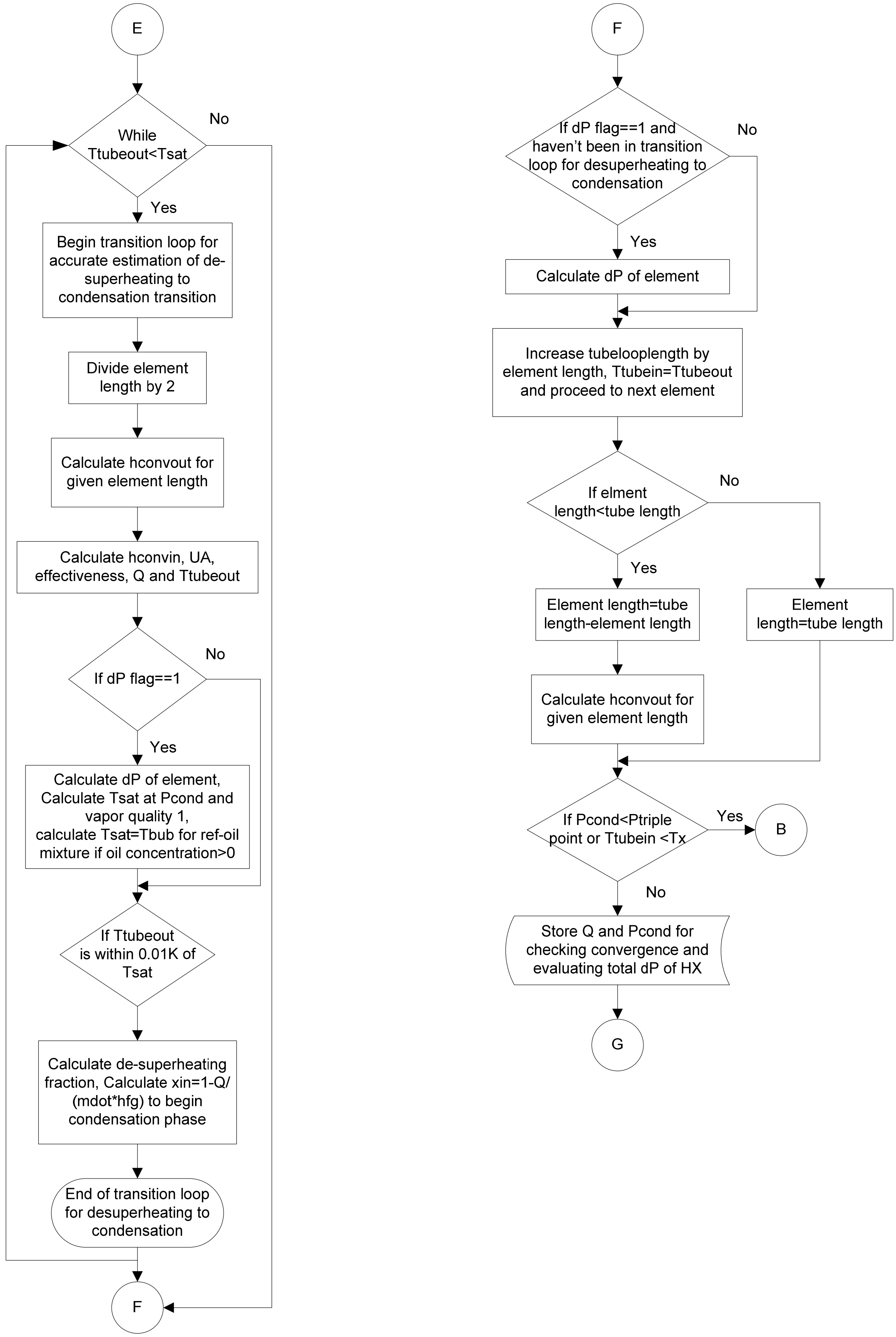
E
While Ttubeout<Tsat
No
Yes
Begin transition loop for accurate estimation of de-superheating to condensation transition
Divide element length by 2
Calculate hconvout for given element length
Calculate hconvin, UA, effectiveness, Q and Ttubeout
If dP flag==1
No
Yes
Calculate dP of element, Calculate Tsat at Pcond and vapor quality 1, calculate Tsat=Tbub for ref-oil mixture if oil concentration>0
If Ttubeout is within 0.01K of Tsat
Calculate de-superheating fraction, Calculate xin=1-Q/(mdot*hfg) to begin condensation phase
End of transition loop for desuperheating to condensation
F
F
If dP flag==1 and haven't been in transition loop for desuperheating to condensation
No
Yes
Calculate dP of element
Increase tubelooplength by element length, Ttubein=Ttubeout and proceed to next element
If elment length<tube length
No
Yes
Element length=tube length-element length
Element length=tube length
Calculate hconvout for given element length
If Pcond<Ptriple point or Ttubein <Tx
Yes
B
No
Store Q and Pcond for checking convergence and evaluating total dP of HX
G

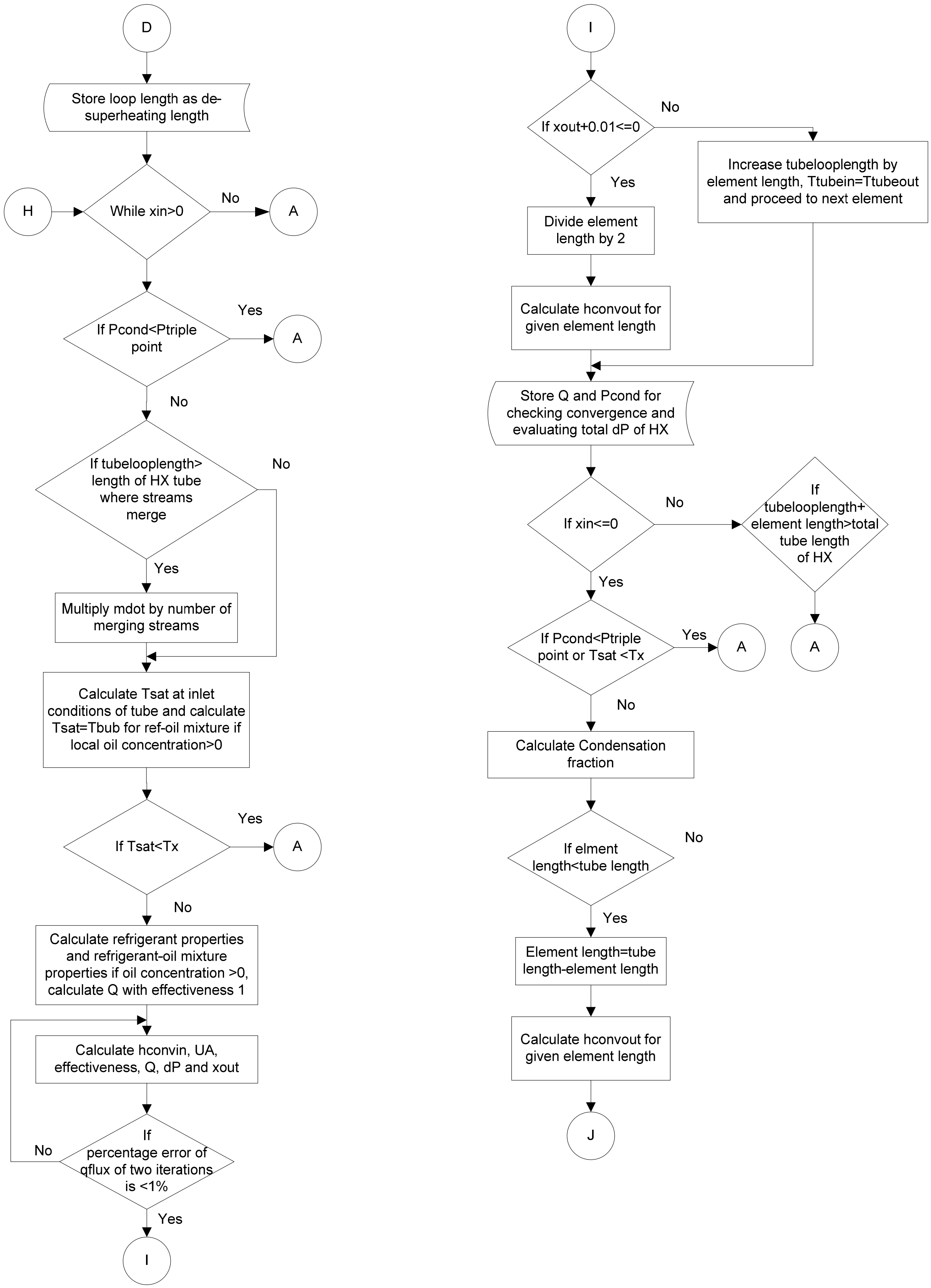
D
Store loop length as de-superheating length
H
While xin>0
No
A
If Pcond<Ptriple point
Yes
A
No
If tubelooplength> length of HX tube where streams merge
No
Yes
Multiply mdot by number of merging streams
Calculate Tsat at inlet conditions of tube and calculate Tsat=Tbub for ref-oil mixture if local oil concentration>0
If Tsat<Tx
Yes
A
No
Calculate refrigerant properties and refrigerant-oil mixture properties if oil concentration >0, calculate Q with effectiveness 1
Calculate hconvin, UA, effectiveness, Q, dP and xout
If percentage error of qflux of two iterations is <1%
No
Yes
I
I
If xout+0.01<=0
No
Increase tubelooplength by element length, Ttubein=Ttubeout and proceed to next element
Yes
Divide element length by 2
Calculate hconvout for given element length
Store Q and Pcond for checking convergence and evaluating total dP of HX
If xin<=0
No
If tubelooplength+ element length>total tube length of HX
A
Yes
If Pcond<Ptriple point or Tsat <Tx
Yes
A
No
Calculate Condensation fraction
If elment length<tube length
No
Yes
Element length=tube length-element length
Calculate hconvout for given element length
J

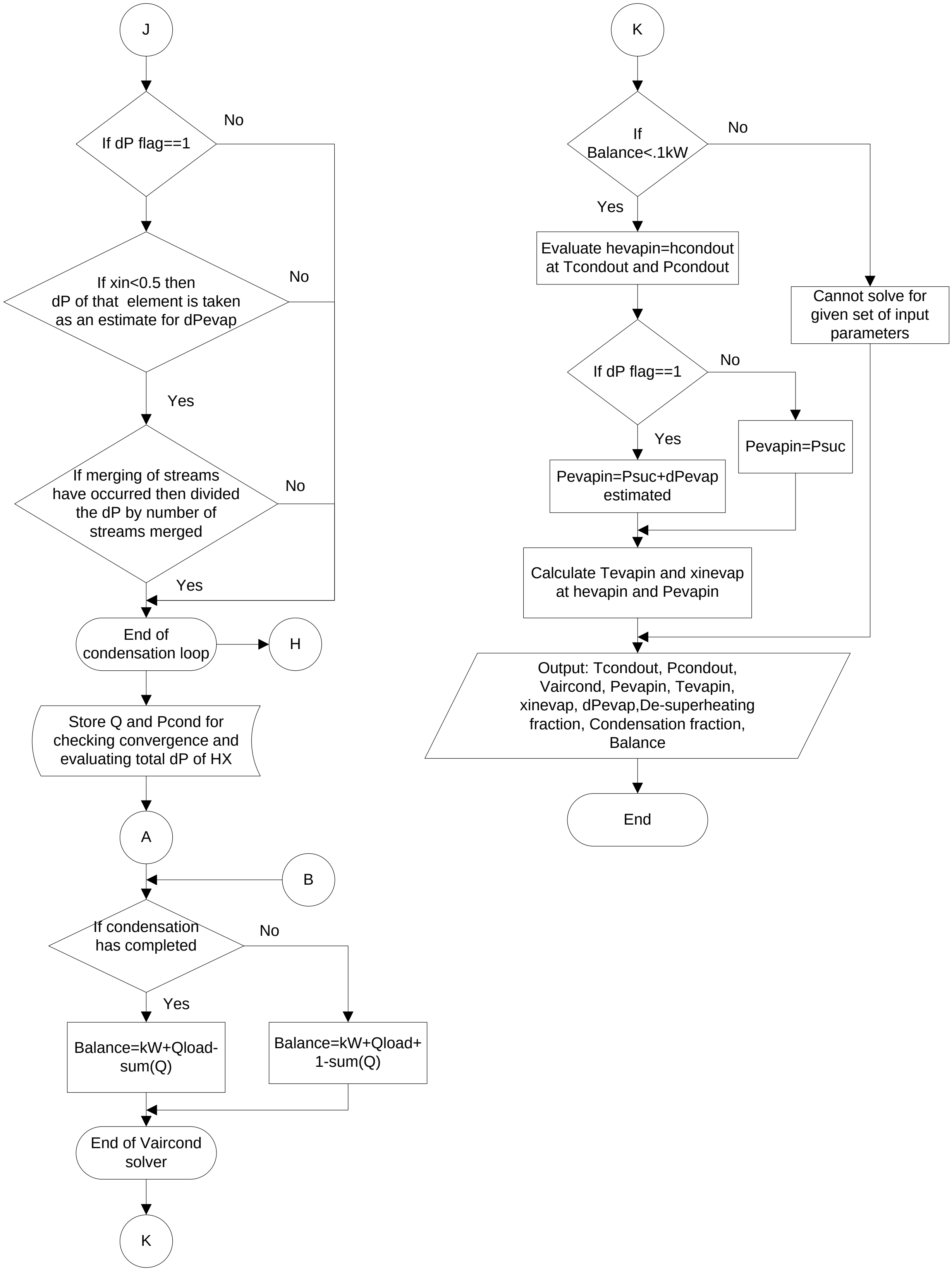


Figure 3.10: Condenser model flow chart

### 3.4.8 Fan-Coil Evaporator Model Description

The input and output parameters that are required for the evaporator model is given in Table 3.6 and Table 3.7:

Table 3.6: Fan-coil evaporator model parameters

| **Input** | **Output** |
|---|---|
| $\dot{m}_{ref}$ | $\dot{V}_{air_{evap}}$ |
| $Q_{load}$ | $T_{evap_{out}}$ |
| $P_{evap_{in}}$ | $P_{evap_{out}}$ |
| $T_{evap_{in}}$ | Evaporation zone fraction |
| $x_{evap_{in}}$ | $dP_{evap}$ |
| Evaporator details | Evaporator Effectiveness |
| System details | |

Table 3.7: Fan-coil evaporator details required

| | |
|---|---|
| Tube diameter | Tube thermal conductivity |
| Tube thickness | Fin thickness |
| Tube length | Fin width |
| Tube transversal pitch | Fin pitch |
| Total number of tubes | Fin thermal conductivity |
| Number of stream divisions | Evaporator height |
| Number of tube rows | Evaporator length |

The system details are listed in section 3.6. For the given set of input parameters, $\dot{V}_{air_{evap}}$ is searched between its maximum and minimum limits using MATLAB function *'fmincon'* until convergence. The maximum limit in the present study is taken from the Mitsubishi Mr. Slim manual of MSZ-A09NA. The limits are:

Maximum $\dot{V}_{air_{evap}}$ : 0.13 m$^3$/sec

Minimum $\dot{V}_{air_{evap}}$ : 0.18 m$^3$/sec

Convergence is achieved by satisfying the Equation 3.4.88:

$$\text{Balance} = Q_{load} - \text{sum}(Q_{element}) \tag{3.4.88}$$

A multi-start point search algorithm is used to attain global minimum. In this algorithm, *'fmincon'* is supplied a set of linearly varying initial points defined between the maximum and minimum limits. The minimum of the balance from these points is taken as the final solution. The flow chart of the fan-coil evaporator model is given in Figure 3.11.

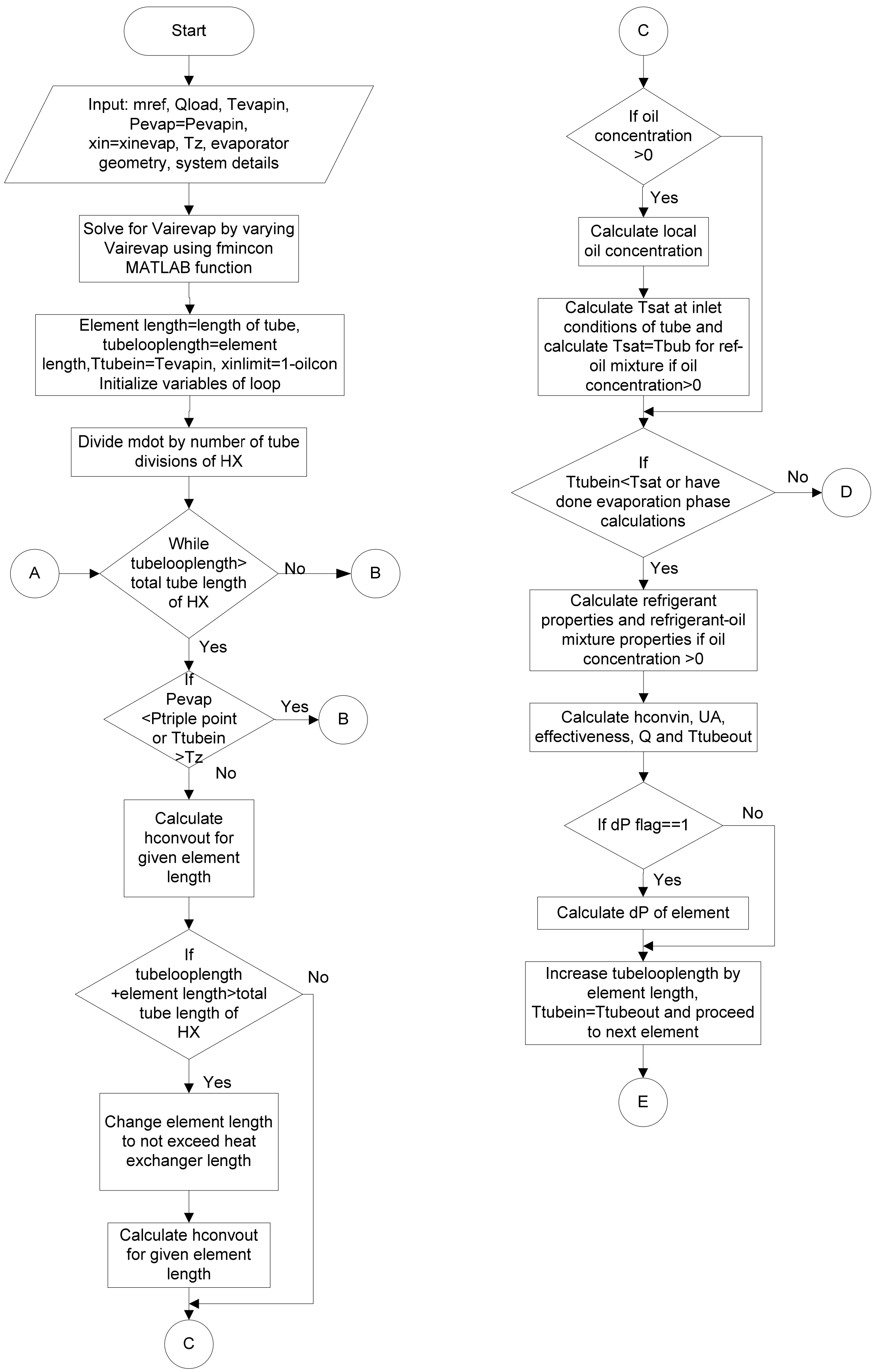

Start
Input: mref, Qload, Tevapin, Pevap=Pevapin, xin=xinevap, Tz, evaporator geometry, system details
Solve for Vairevap by varying Vairevap using fmincon MATLAB function
Element length=length of tube, tubelooplength=element length,Ttubein=Tevapin, xinlimit=1-oilcon Initialize variables of loop
Divide mdot by number of tube divisions of HX
A
While tubelooplength> total tube length of HX
No
B
Yes
If Pevap <Ptriple point or Ttubein >Tz
Yes
B
No
Calculate hconvout for given element length
If tubelooplength +element length>total tube length of HX
No
Yes
Change element length to not exceed heat exchanger length
Calculate hconvout for given element length
C
C
If oil concentration >0
Yes
Calculate local oil concentration
Calculate Tsat at inlet conditions of tube and calculate Tsat=Tbub for ref-oil mixture if oil concentration>0
If Ttubein<Tsat or have done evaporation phase calculations
No
D
Yes
Calculate refrigerant properties and refrigerant-oil mixture properties if oil concentration >0
Calculate hconvin, UA, effectiveness, Q and Ttubeout
If dP flag==1
No
Yes
Calculate dP of element
Increase tubelooplength by element length, Ttubein=Ttubeout and proceed to next element
E

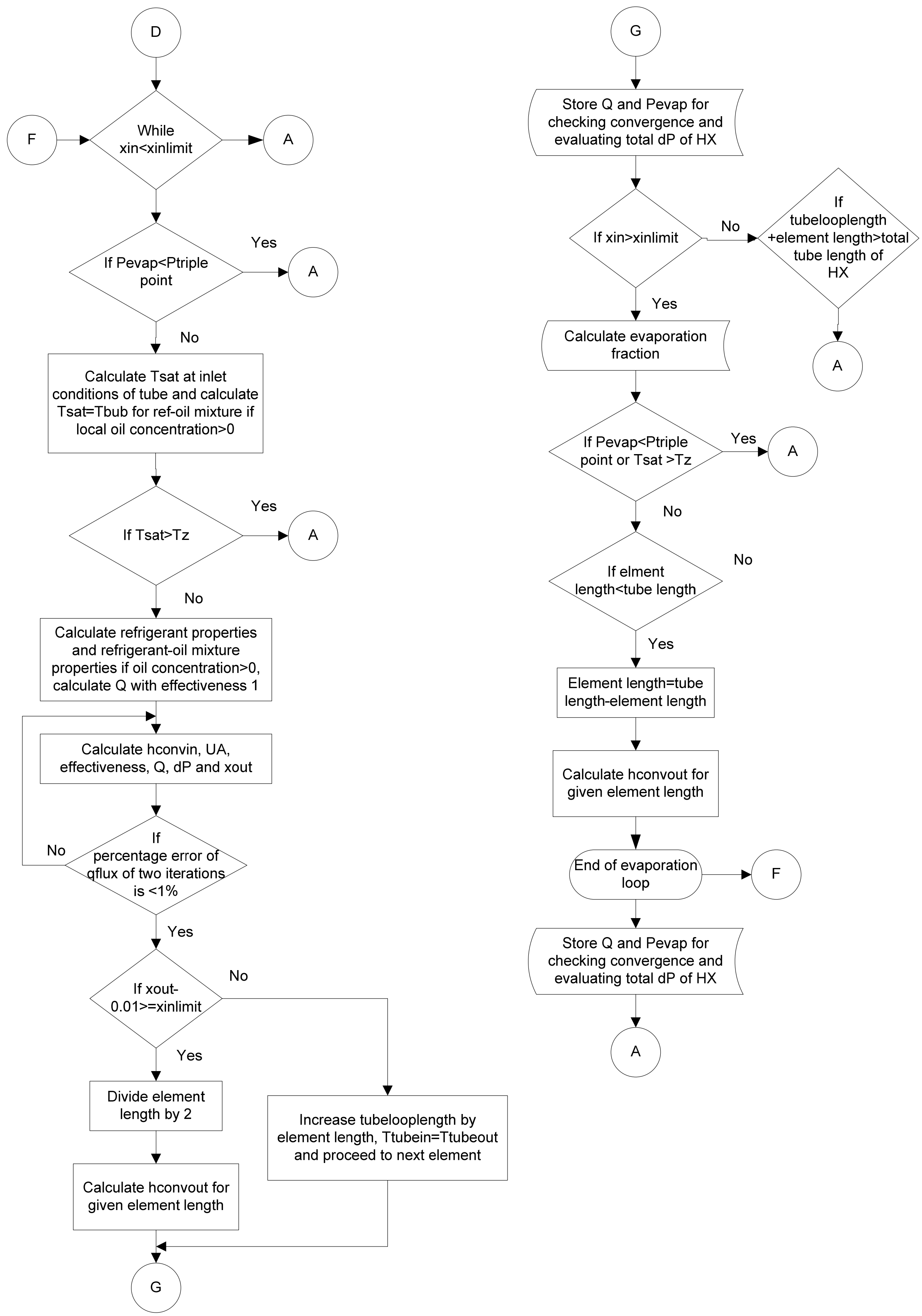
D
F
While xin<xinlimit
A
If Pevap<Ptriple point
Yes
A
No
Calculate Tsat at inlet conditions of tube and calculate Tsat=Tbub for ref-oil mixture if local oil concentration>0
If Tsat>Tz
Yes
A
No
Calculate refrigerant properties and refrigerant-oil mixture properties if oil concentration>0, calculate Q with effectiveness 1
Calculate hconvin, UA, effectiveness, Q, dP and xout
No
If percentage error of qflux of two iterations is <1%
Yes
If xout-0.01>=xinlimit
No
Yes
Divide element length by 2
Increase tubelooplength by element length, Ttubein=Ttubeout and proceed to next element
Calculate hconvout for given element length
G
G
Store Q and Pevap for checking convergence and evaluating total dP of HX
If xin>xinlimit
No
If tubelooplength +element length>total tube length of HX
A
Yes
Calculate evaporation fraction
If Pevap<Ptriple point or Tsat >Tz
Yes
A
No
If elment length<tube length
No
Yes
Element length=tube length-element length
Calculate hconvout for given element length
End of evaporation loop
F
Store Q and Pevap for checking convergence and evaluating total dP of HX
A

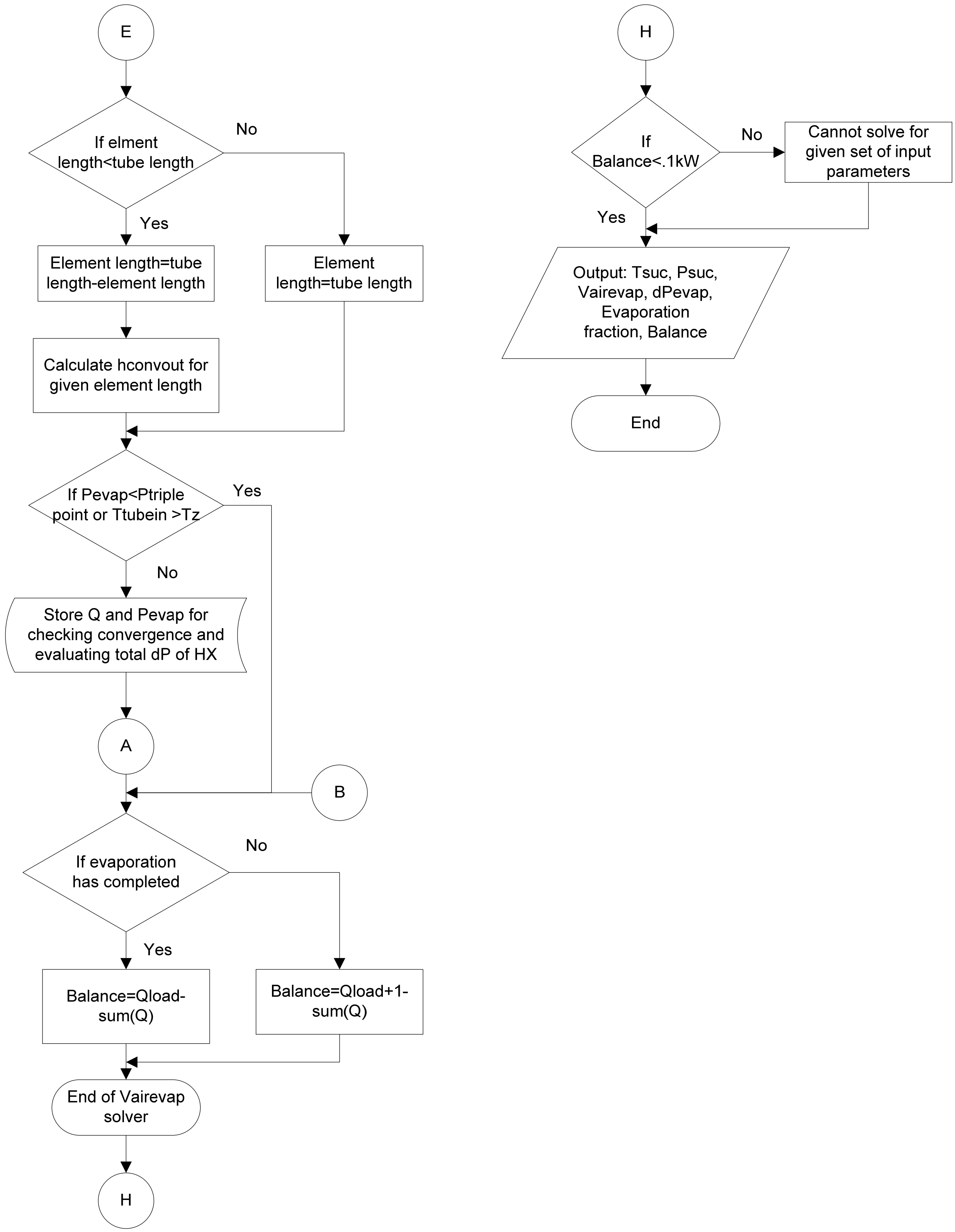


Figure 3.11: Fan-coil evaporator model flow chart

## 3.5 Brazed-Plate Heat Exchanger Model

The brazed-plate HX model is used to model the evaporation process in chiller mode. The mass flow rates are divided by the number of plates in the brazed-plate HX. The plate of the HX is then discretized into a finite number of elements and heat transfer and pressure drop calculations are evaluated in a progressive manner. For the transition between single-phase and two-phase heat transfer, the element length is changed to accurately identify the location of the transition. The transition from two-phase to single-phase is calculated to within 1% of vapor quality. The maximum vapor quality is considered as ($1-\omega_{oil}$) for the brazed-plate evaporator.

The following assumptions are made for the model:

– Uniform water and refrigerant distribution over the number of plates
– Effect of water-side pressure drop on heat transfer is negligible
– Radiation heat transfer effects are negligible

### 3.5.1 Single-Phase Refrigerant Side Heat Transfer

The single-phase heat transfer at the refrigerant side is evaluated using Equation 3.4.16 or Equation 3.4.17. The terms in Equation 3.4.16 in the case of brazed-plate HX are described in Equations 3.5.1-3.5.3:

$$dT = T_{water_{in}} - T_{ref_{in}} \tag{3.5.1}$$

$$\varepsilon = \frac{1 - \exp\left(-NTU * (1 - C_r)\right)}{1 - C_r * \exp\left(-NTU * (1 - C_r)\right)} \tag{3.5.2}$$

$$UA = \left(\frac{1}{h_{conv_{in}}} + \frac{t_{plate}}{k_{plate}} + \frac{1}{h_{conv_{out}}}\right)^{-1} * L_{element} * \text{wetted perimeter} \tag{3.5.3}$$

The heat transfer coefficient for single-phase heat transfer is calculated based on Reynolds number. For Reynolds number less than 1000, the heat transfer coefficient is calculated using Equations 3.5.4 as (Wanniarachchi, Ratnam, Tilton, & Dutta-Roy, 1995):

$$h_{conv} = \left(Nu_{laminar}^3 + Nu_{turbulent}^3\right)^{\frac{1}{3}} * Pr^{\frac{1}{3}} * \left(\frac{\mu}{\mu_{wall}}\right)^{0.17} * \frac{k}{D_{eq}} \tag{3.5.4}$$

where,

$$Nu_{laminar} = 3.65 * \beta^{-0.455} * \phi^{0.661} * Re^{0.339} \tag{3.5.5}$$

$$Nu_{turbulent} = 12.6 * \beta^{-1.142} * \phi^{1-m} * Re^{m} \tag{3.5.6}$$

$$m = 0.646 + 0.0011 * \beta \tag{3.5.7}$$

For Reynolds number greater than or equal to 1000, the heat transfer coefficient is calculated using Equation 3.5.8 (Muley & Manglik, 1999):

$$\begin{aligned} h_{conv} = {} & \left(0.2668 - 0.006967 * \beta + 7.244 * 10^{-5} * \beta^2\right) \\ & * (20.78 - 50.94 * \phi + 41.16 * \phi^2 - 10.51 * \phi^3) \\ & * Re^{0.728+0.0543*\sin\left(\pi*\frac{\beta}{45}+3.7\right)} * Pr^{\frac{1}{3}} * \left(\frac{\mu}{\mu_{wall}}\right)^{0.14} * \frac{k}{D_{eq}} \end{aligned} \tag{3.5.8}$$

### 3.5.2 Single-Phase Refrigerant-Side Pressure Drop

The single-phase pressure drop is calculated through Equation 3.4.26. For Reynolds number less than 1000, the friction factor '*f*' is calculated using Equation 3.5.9 (Wanniarachchi et al., 1995):

$$f = \left(f_{laminar}^3 + f_{turbulent}^3\right)^{\frac{1}{3}} \tag{3.5.9}$$

where,

$$f_{laminar} = 1774 * \beta^{-1.026} * \phi^2 * Re^{-1} \tag{3.5.10}$$

$$f_{turbulent} = 46.6 * \beta^{-1.08} * \phi^{1+p} * Re^{-p} \tag{3.5.11}$$

$$p = 0.00423 * \beta + 0.0000223 * \beta^2 \tag{3.5.12}$$

For Reynolds number greater than or equal to 1000, the friction factor '*f*' is calculated using Equation 3.5.13 (Muley & Manglik, 1999):

$$\begin{aligned} f = & \left(2.917 - 0.1277 * \beta + 2.016 * 10^{-3} * \beta^2\right) \\ & * (5.474 - 19.02 * \phi + 18.93 * \phi^2 - 5.341 * \phi^3) \\ & * Re^{-\left(0.2+0.0577*\sin\left(\pi*\frac{\beta}{45}+2.1\right)\right)} \end{aligned} \tag{3.5.13}$$

The gravitational pressure drop is also added to the frictional pressure drop. The gravitational pressure drop is given in Equation 3.5.14:

$$\left(\frac{dp}{dx}\right)_{gravity} = \rho * 9.8 * L_{element} \tag{3.5.14}$$

### 3.5.3 Two-Phase Refrigerant-Side Heat Transfer

The refrigerant side heat transfer in the two-phase region is calculated using Equation 3.4.14 or Equation 3.4.45. The terms in Equation 3.4.16 for two-phase heat transfer are described in Equations 3.5.15-3.5.16:

$$dT = T_{water_{in}} - T_{bulb} \tag{3.5.15}$$

$$\varepsilon = 1 - \exp(-NTU) \tag{3.5.16}$$

The heat transfer coefficient for two-phase heat transfer is calculated using Equation 3.5.17 (Hsieh & T. F. Lin, 2003):

$$h_{conv_{in}} = E * h_{conv_{liq}} + S * h_{conv_{pool}} \tag{3.5.17}$$

where,

$$h_{conv_{pool}} = 55 * P_{reduced}^{0.12} * \left(-1 * \log10(P_{reduced})\right)^{-0.55} * M^{-0.5} * q_{flux}^{0.67} \tag{3.5.18}$$

$$h_{conv_{liq}} = 0.023 * Re_{liq}^{\frac{4}{5}} * Pr_{liq}^{0.4} * \frac{k_{liq}}{D_{eq}} \tag{3.5.19}$$

$$X_{tt} = \left(\frac{1 - x_{in}}{x_{in}}\right)^{0.9} * \left(\frac{\rho_g}{\rho_{liq}}\right)^{0.5} * \left(\frac{\mu_{liq}}{\mu_g}\right)^{0.1} \tag{3.5.20}$$

$$E = 1 + 24000 * \left(\frac{q_{flux}}{G * h_{fg}}\right)^{1.16} + 1.37 * \left(\frac{1}{X_{tt}}\right)^{.86} \tag{3.5.21}$$

$$S = \left(1 + 1.15e - 6 * E^2 * Re_{liq}^{1.17}\right)^{-1} \tag{3.5.22}$$

### 3.5.4 Two-Phase Refrigerant-Side Pressure Drop

The two-phase pressure drop is calculated using Equation 3.4.26. The friction factor '*f*' is calculated using Equation 3.5.23 (Hsieh & T. F. Lin, 2003):

$$f = 23820 * Re_{eq}^{-1.12} \tag{3.5.23}$$

where,

$$Re_{eq} = G_{eq} * \frac{D_{eq}}{\mu_{liq}} \tag{3.5.24}$$

$$G_{eq} = G * \left( (1 - x_{in}) + x_{in} * \left( \frac{\rho_{liq}}{\rho_g} \right)^{0.5} \right) \tag{3.5.25}$$

The gravitational and acceleration pressure drop are also added to the frictional pressure drop. The acceleration pressure drop is given in Equation 3.5.26 (Han et al., 2003):

$$\left( \frac{dp}{dx} \right)_{acceleration} = G_{eq}^2 * \frac{x_{out}}{\rho_{liq} - \rho_g} - G_{eq}^2 * \frac{x_{in}}{\rho_{liq} - \rho_g} \tag{3.5.26}$$

### 3.5.5 Port Pressure Drop

The pressure drop at the ports of the brazed-plate HX is given in Equation 3.5.27 (Han et al., 2003):

$$\left( \frac{dp}{dx} \right)_{port} = 1.4 * \frac{\left( \frac{\dot{m}}{\frac{\pi}{4} * D_{port}^2} \right)^2}{2 * \rho_g} \tag{3.5.27}$$

### 3.5.6 Brazed-Plate Evaporator Model Description

The input and output parameters that are required for the brazed-plate evaporator model is given in Table 3.8 and

Table 3.9:

Table 3.8: Brazed-plate evaporator model parameters

| **Input** | **Output** |
|---|---|
| $\dot{m}_{ref}$ | $\dot{V}_{water_{evap}}$ |
| $Q_{load}$ | $T_{evap_{out}}$ |
| $P_{evap_{in}}$ | $P_{evap_{out}}$ |
| $T_{evap_{in}}$ | Evaporation zone fraction |
| $x_{evap_{in}}$ | $dP_{evap}$ |
| Evaporator details | Evaporator Effectiveness |
| System details | |

Table 3.9: Brazed-plate evaporator details required

| | |
|---|---|
| Plate length | Number of plates |
| Plate thickness | Enlargement factor |
| Plate width | Corrugation pitch |
| Channel thickness | Chevron angle |
| Port diameters | |

The system details are listed in section 3.6. For the given set of input parameters, $\dot{V}_{water_{evap}}$ is searched between its maximum and minimum limits using MATLAB function *'fmincon'* until convergence. The maximum and minimum limits in the present study are taken from the experimental data.

The limits are:

Maximum $\dot{V}_{water_{evap}}$ : 0.28e-3 $m^3$/sec

Minimum $\dot{V}_{water_{evap}}$ : 0.12e-3 $m^3$/sec

Convergence is achieved by satisfying Equation 3.5.28:

$$\text{Balance} = Q_{load} - \text{sum}(Q_{element}) * \text{No. of Plates} \tag{3.5.28}$$

A multi-start point search algorithm is used to attain global minimum. In this algorithm, *'fmincon'* is supplied a set of linearly varying initial points defined between the maximum and minimum limits. The minimum of the balance from these points is taken as the final solution. The flow chart of the brazed-plate evaporator model is given in Figure 3.12.

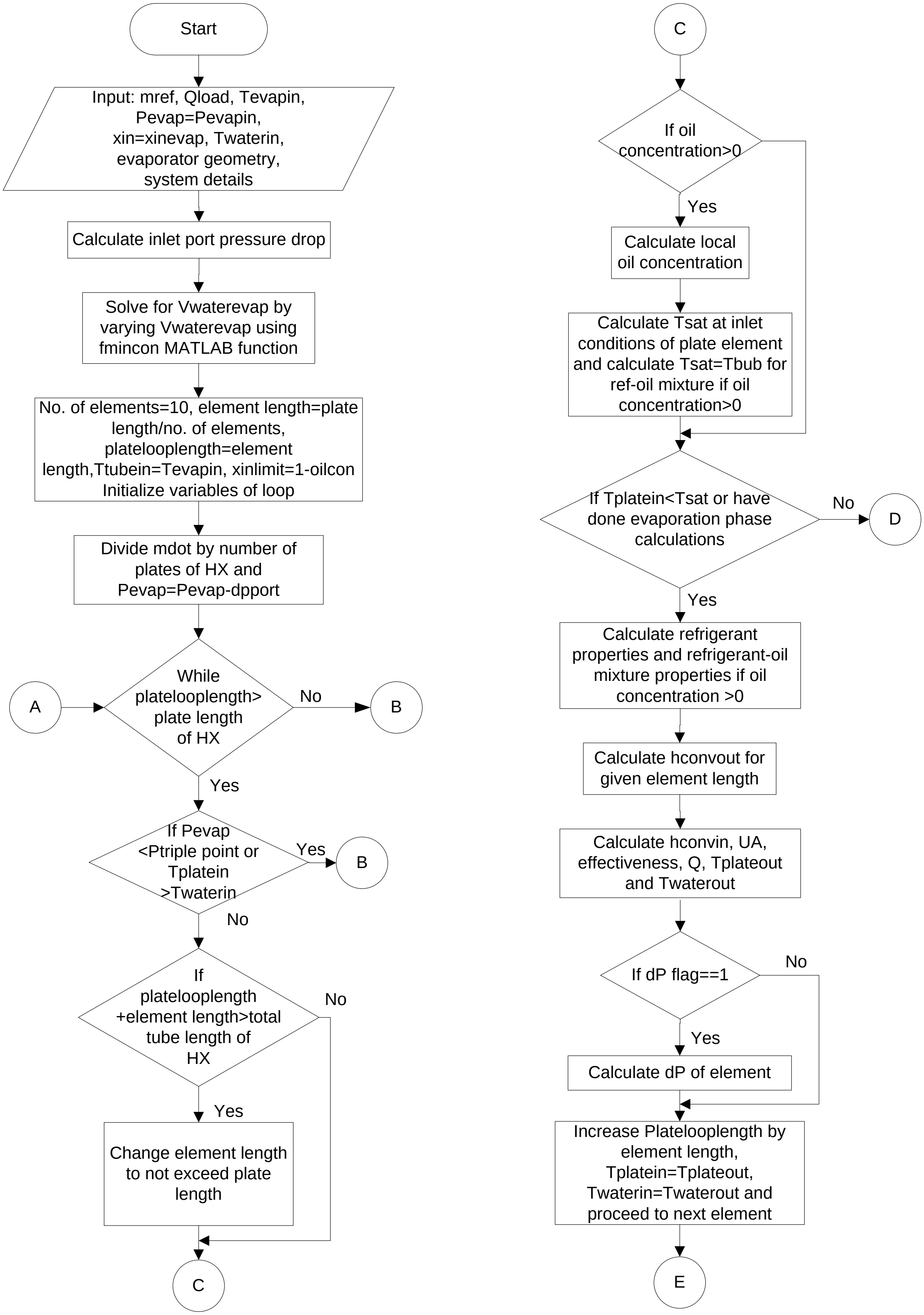
Start
Input: mref, Qload, Tevapin, Pevap=Pevapin, xin=xinevap, Twaterin, evaporator geometry, system details
Calculate inlet port pressure drop
Solve for Vwaterevap by varying Vwaterevap using fmincon MATLAB function
No. of elements=10, element length=plate length/no. of elements, platelooplength=element length,Ttubein=Tevapin, xinlimit=1-oilcon Initialize variables of loop
Divide mdot by number of plates of HX and Pevap=Pevap-dpport
A
While platelooplength> plate length of HX
No
B
Yes
If Pevap <Ptriple point or Tplatein >Twaterin
Yes
B
No
If platelooplength +element length>total tube length of HX
No
Yes
Change element length to not exceed plate length
C
C
If oil concentration>0
Yes
Calculate local oil concentration
Calculate Tsat at inlet conditions of plate element and calculate Tsat=Tbub for ref-oil mixture if oil concentration>0
If Tplatein<Tsat or have done evaporation phase calculations
No
D
Yes
Calculate refrigerant properties and refrigerant-oil mixture properties if oil concentration >0
Calculate hconvout for given element length
Calculate hconvin, UA, effectiveness, Q, Tplateout and Twaterout
If dP flag==1
No
Yes
Calculate dP of element
Increase Platelooplength by element length, Tplatein=Tplateout, Twaterin=Twaterout and proceed to next element
E

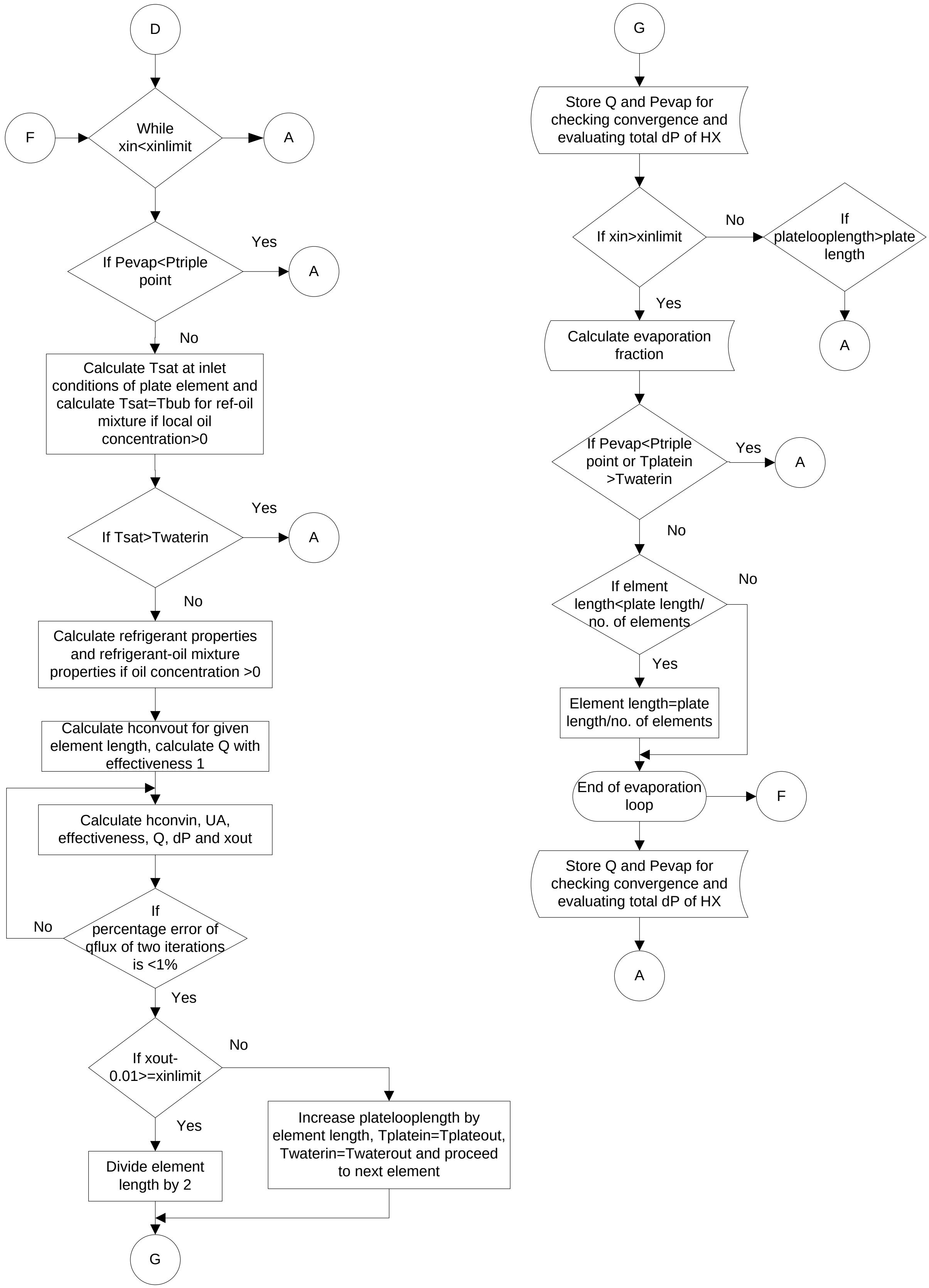
D
F
While xin<xinlimit
A
If Pevap<Ptriple point
Yes
A
No
Calculate Tsat at inlet conditions of plate element and calculate Tsat=Tbub for ref-oil mixture if local oil concentration>0
If Tsat>Twaterin
Yes
A
No
Calculate refrigerant properties and refrigerant-oil mixture properties if oil concentration >0
Calculate hconvout for given element length, calculate Q with effectiveness 1
Calculate hconvin, UA, effectiveness, Q, dP and xout
If percentage error of qflux of two iterations is <1%
No
Yes
If xout-0.01>=xinlimit
No
Yes
Divide element length by 2
Increase platelooplength by element length, Tplatein=Tplateout, Twaterin=Twaterout and proceed to next element
G
G
Store Q and Pevap for checking convergence and evaluating total dP of HX
If xin>xinlimit
No
If platelooplength>plate length
A
Yes
Calculate evaporation fraction
If Pevap<Ptriple point or Tplatein >Twaterin
Yes
A
No
If elment length<plate length/ no. of elements
No
Yes
Element length=plate length/no. of elements
End of evaporation loop
F
Store Q and Pevap for checking convergence and evaluating total dP of HX
A

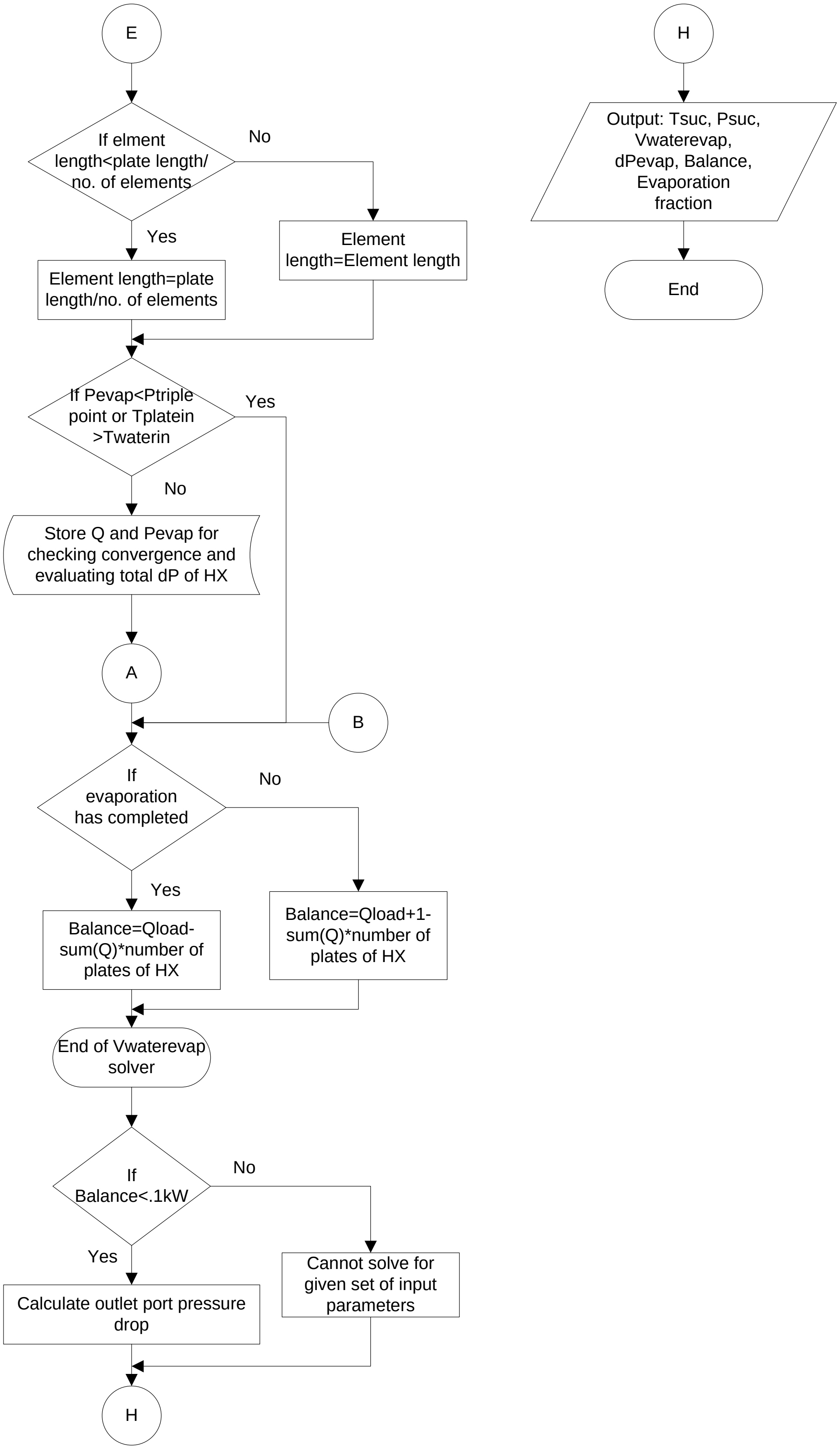


Figure 3.12: Brazed-plate evaporator model flow chart

## 3.6 System Model

The system model is developed to estimate the different parameters of the system for a given set of $T_x$, $T_z$, $Q_{load}$, $P_{dis}$ and $P_{suc}$.

The system model consists of compressor model, condenser model and evaporator model. The evaporator model can be either fan-coil HX evaporator model or brazed-plate HX evaporator model depending on mode of operation. The expansion valve is modeled as an isenthalpic expansion process. The input and output parameters required for the system model is given in Table 3.10 and

Table 3.11:

Table 3.10: System model parameters

| **Input** | **Output** |
|---|---|
| $P_{dis}$ | Component model results |
| $P_{suc}$ | System power |
| System details | |

Table 3.11: System details required

| | |
|---|---|
| Ambient pressure | Maximum temperature of refrigerant |
| $T_x$ | Maximum Pressure of refrigerant |
| $T_z$ | Critical pressure of refrigerant |
| $Q_{load}$ | Triple point pressure of refrigerant |
| Refrigerant type | Oil concentration |
| Molar mass of refrigerant | Fan/pump power curve constants |
| Minimum temperature of refrigerant | Ambient fluid type |

The system power is evaluated using the compressor power from compressor model and fan/pump power curves for the given amount of volumetric flow rate of air from condenser model and fan-coil HX evaporator model in case of DX unit operation. For chiller unit operation volumetric flow rate of water from brazed-plate HX evaporator model is used. System power is calculated using Equation 3.6.1 or Equation 3.6.2:

For DX unit:

$$\text{System Power (W)} = \text{kW} * 1\text{e}3 + \text{fan}_{\text{cond}}\text{C}_1 * \dot{\text{V}}_{\text{air}_{\text{cond}}}^{\text{fan}_{\text{cond}}\text{C}_2} + \text{fan}_{\text{evap}}\text{C}_1 * \dot{\text{V}}_{\text{air}_{\text{evap}}}^{\text{fan}_{\text{evap}}\text{C}_2} \tag{3.6.1}$$

For Chiller:

$$\begin{aligned}\text{System Power (W)}& \\ &= \text{kW} * 1\text{e}3 + \text{fan}_{\text{cond}}\text{C}_1 * \dot{\text{V}}_{\text{air}_{\text{cond}}}^{\text{fan}_{\text{cond}}\text{C}_2} + \text{pump}_{\text{evap}}\text{C}_1 * \dot{\text{V}}_{\text{water}_{\text{evap}}}^{\text{pump}_{\text{evap}}\text{C}_2} \\ &+ \text{pump}_{\text{evap}}\text{C}_3\end{aligned} \tag{3.6.2}$$

The fan or pump power model is derived from the basic fan laws in which the power is described as a cubic of the volumetric flow rate of air through the fan. Due to electrical and mechanical conversion losses, the exponent of the power model deviates from the ideal flow-power curve. The fan-power curve for the condenser is determined through flow hood testing. The evaporator fan-power curve is obtained using experimental data of power at different speeds and air flow data at those speeds given in the manufacturer manual. The fan and pump power curve coefficients and RMSE are given in Table 3.12.

Table 3.12: Fan and Pump Power Coefficients and RMSE

| | **Condenser Fan** | **DX Evaporator Fan** | **Chiller evaporator pump** |
|---|---|---|---|
| $C_1$ | 383.126 | 431 | 2.758e+006 |
| $C_2$ | 3.27 | 1.792 | 1.493 |
| $C_3$ | — | — | 18.63 |
| RMSE (W) | 0.8595 | 0.7109 | 0.6045 |

For a given set of $T_x$, $T_z$, $Q_{load}$, $P_{dis}$ and $P_{suc}$, compressor model is called to solve for compressor output conditions, refrigerant mass flow rate, compressor speed and compressor power. The output conditions are then supplied to the condenser model to solve for condenser air mass flow rate and HX outlet conditions. It recalculates the $\dot{m}_{ref}$ by calling the compressor model again, as the evaporator inlet enthalpy is known. If $\dot{m}_{ref}$ of the previous iteration and the current iteration is within 1%, it calls the evaporator model. The evaporator model evaluates the evaporator air or water mass flow rate and HX outlet conditions. $dP_{evap}$ is then recalculated as the condenser model provides an estimate of $dP_{evap}$. If $dP_{evap}$ of the previous and current iteration is within 1%. Recalculation of compressor, condenser and evaporator parameters is done as suction temperature is known which affects calculation of $\dot{m}_{ref}$ as described in Figure 3.6. If suction temperature the previous and current iteration is within 1%, system power is calculated using Equation 3.6.1 or Equation 3.6.2 depending on mode of operation. The flow chart of the system model is given in Figure 3.13.

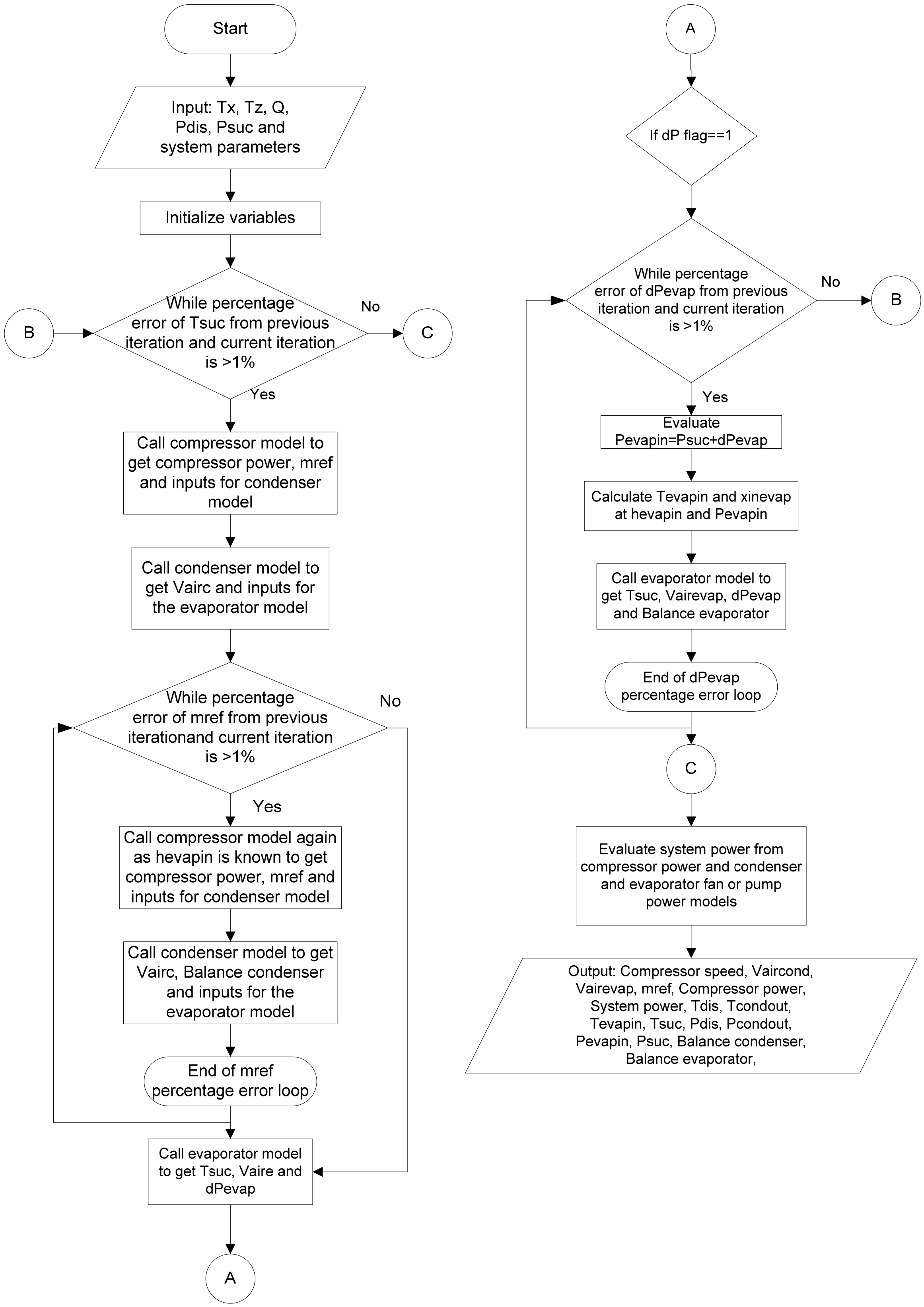


Figure 3.13: System model flow chart

# CHAPTER 4

# Experimental Setup and Instrumentation

This study is part of the low-lift, radiant-cooling with pre-cooling control project being carried out at Masdar Institute (MI). A test stand has been built from a Mitsubishi split unit MUZA09NA-1 for validation of the vapor compression equipment components models described in Chapter 3. A test chamber has also been built as part of the project to investigate the savings of low-lift cooling with pre-cooling control over conventional DX units. This chapter describes the test stand and its instrumentation, the test chamber details and the sensors installed within, air-tightness of the test chamber, Linear Expansion Valve (LEV) control accuracy, test stand instrumentation accuracy and experimentation details.

## 4.1 Test Stand Description

Figure 4.1 describes the instrumentation and different fluid circuits on the test stand. Refrigerant circuits during DX operation and chiller operation are also shown. Details of the individual components and sensors installed on the test stand are provided in Appendix A.

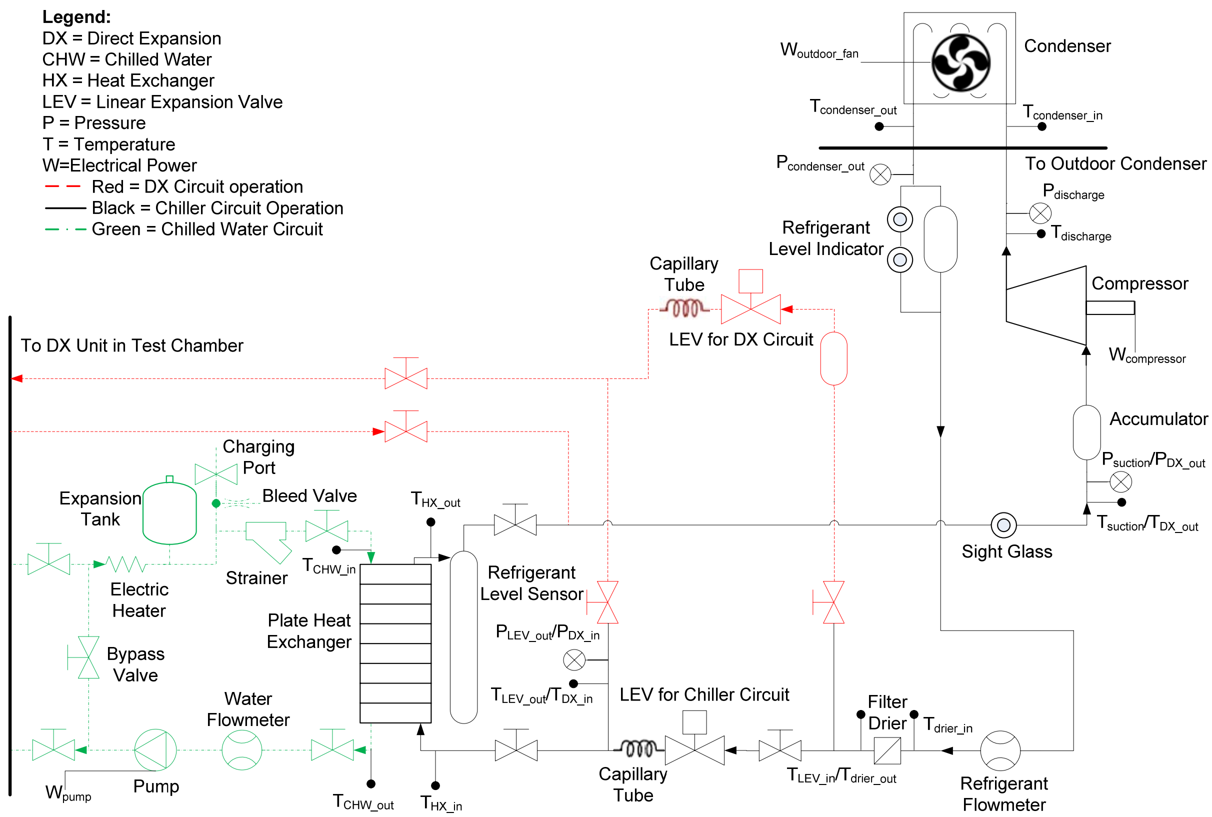


Figure 4.1: Test stand component schematic

A refrigerant level indicator is built using two sight glasses and a liquid receiver to observe the refrigerant liquid level after exit from the condenser. This is required to maintain a certain refrigerant level head prior to the refrigerant flow meter because the flow meter measures liquids. If a refrigerant level head is not maintained, flashing of the refrigerant occurs in the flow meter due to pressure drop across the flow meter. The amount of refrigerant charges for DX mode and chiller mode of operation used in experimentation are given in Table 4.1:

Table 4.1: Refrigerant charge for DX and Chiller modes of operation

| **Operation Mode** | **Refrigerant charge** |
|---|---|
| DX | 0.907kg (2lb) |
| Chiller | 1.077 (2lb 6oz) |

A Y-strainer is installed at the inlet to the brazed-plate HX to prevent fouling of the HX. An expansion tank is installed in the chilled water circuit to accommodate for water volume changes with temperature. Four pressure transducers are installed to measure pressures at the inlet and outlet of the compressor, outlet of condenser and at inlet to the evaporator. The pressure at the condenser inlet is taken equal to the discharge pressure and the pressure at compressor suction is taken equal to the outlet of evaporator. In DX mode, the temperature at suction is taken as the temperature at evaporator outlet. This results in higher residuals for the corresponding parameters estimated by the models as can be seen in the results presented in Chapter 5.

For determining the accuracy of instrumentation of test stand, a bypass valve is installed in the chiller circuit to bypass the test chamber. An electric heating element is installed to provide the heating load and maintain a constant chilled water temperature. The purpose of maintaining a constant chilled water temperature is to achieve steady state. Evacuation and refilling of refrigerant is carried out every time switching is made between DX operation and chiller operation. CR1000 is used to record the data and for controlling the LEV, compressor and outdoor fan speed. The program for CR1000 is provided in Appendix B.

## 4.2 Test Chamber Description

The test chamber components, sensors and their locations are described in Figure 4.2. The test chamber is a modular room with walls made of two painted steel sheets with 6cm fiberglass insulation between them. The west and south walls are exposed to the surroundings while north and east walls are the internal walls of the building. A window is located on the south wall with blinds on the outside. The internal walls and the ceiling are insulated by a 10cm thick polystyrene insulation to isolate the room from the internal temperatures of the building. The installation of insulation reduced the heat transfer by 66%. The calculations are provided in Appendix C. 5cm thick polystyrene insulation is also installed around the slab and 25cm thick polystyrene insulation is placed beneath the slab to eliminate end heat transfer losses and isolate the slab from the ground.

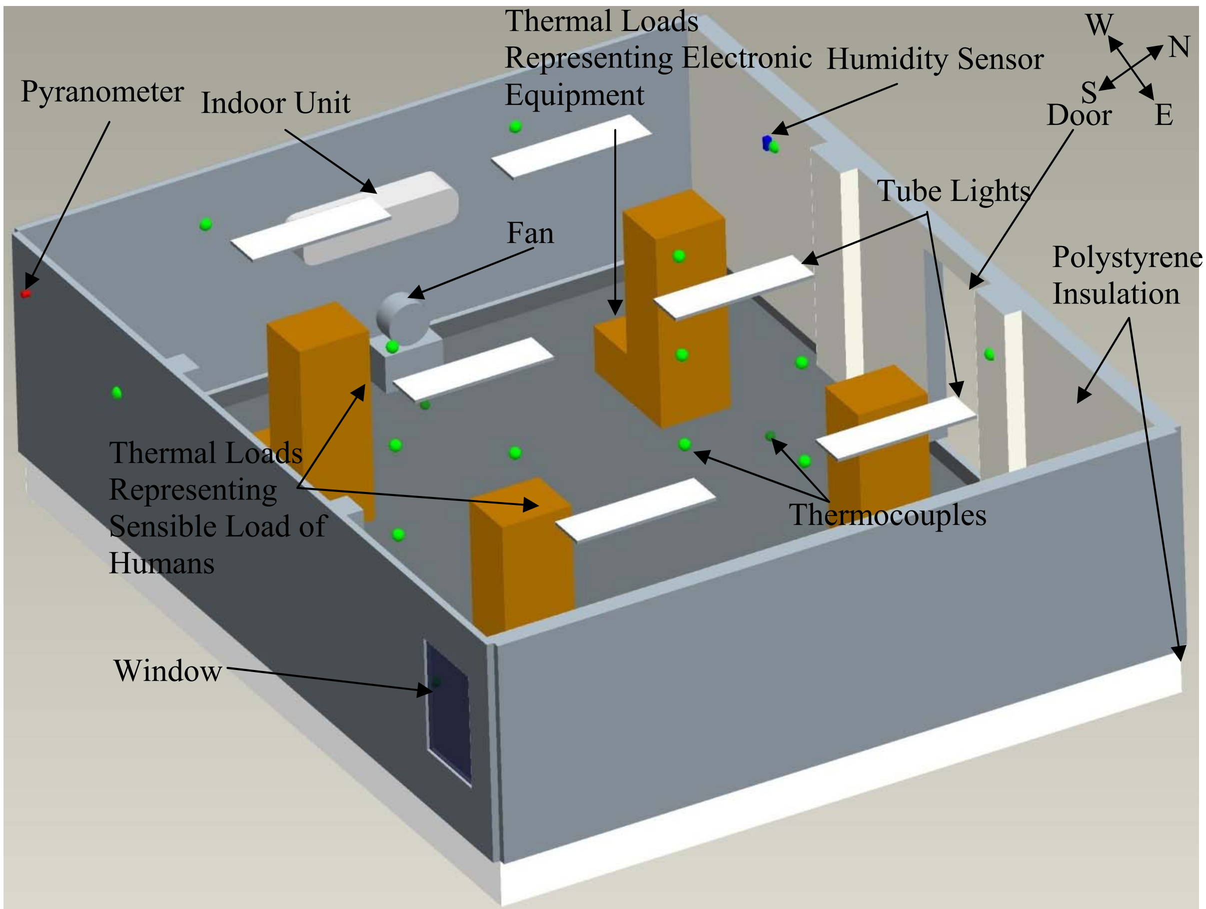


Figure 4.2: Test chamber with instrumentation

Prior to installation of insulation in the test chamber, caulking was carried out to seal the cracks and crevices of the modular room. Acrylic caulk and spray foam insulation was used to make the room air-tight. This reduced the infiltration load of the room. This will help in estimating the savings of low-lift radiant cooling system accurately as the technology only handles sensible cooling load. After caulking and installing of the insulation, blower door testing was performed to quantify the air-tightness of the test chamber. The leakage of the room is identified as 40.9cm$^2$ (±0.3%) Canadian Equivalent Area@10Pa and an Air Change per Hour (ACH) of 1.29@50Pa. The details of the test are provided in Appendix D.

A total of 20 thermocouples are installed in the test chamber, represented by green spheres in Figure 4.2, to measure the internal temperature distribution. A 4x3 grid of 12 thermocouples is installed in the slab at a height of 5cm above the 25cm polystyrene insulation. Two vertical arrays of three additional thermocouples are installed in the slab at a distance of 2.5cm from each other at two locations. Two pyranometers are also installed on the exposed walls to measure the solar radiation falling on them. A humidity sensor is installed in the room for monitoring the specific humidity and the dew point temperature. The detail of thermocouple locations and test chamber components is presented in Appendix E.

In addition to the sensors, thermal loads are placed inside the room to simulate an office room. The thermal loads consists of fluorescent tube lights, thermal de-stratification fan and cloth covered stands representing human sensible load and thermal load of electronic equipment such as laptops. The detail of the thermal loads is presented in Table 4.2.

Table 4.2: Test Chamber Thermal Loads Description

| Item | Description | Load (W) | Load Density (W/m$^2$) |
|---|---|---|---|
| Fluorescent Tube Lights | 6 tube light fixtures with 2 tube lights of 28W in each | 336 | 8.118 |
| Human | 4 stands with 60W incandescent bulbs | 240 | 5.798 |
| Electronic Equipment | 4 stands with 100W incandescent bulbs | 400 | 9.664 |
| Thermal De-stratification Fan | 14inch diameter fan | 60 | 1.450 |
| DX Unit Fan | Used in DX operation | 15 | 0.386 |
| | Total | 1051 | 25.416 |

## 4.3 Experimental Data Set

The experimental data set consists of the data obtained from the test stand built at MI and the test stands used in (Gayeski, 2010; Gayeski et al., 2010). The data sets of (Gayeski, 2010; Gayeski et al., 2010) are used because of similar vapor compression system. Their data sets are represented by “MIT DX” and “MIT Chiller” while the data sets obtained from the test stand at MI are represented by “MI DX” and “MI Chiller” depending on mode of operation. It is to be noted that a constant heat load was maintained for data sets “MIT DX” and “MIT Chiller” by using a resistive heater. However, the heat load on the evaporator varied in the case of “MIT Chiller” and “MI DX” data sets depending on simulated or real outdoor conditions. The steady state was assumed to be attained by observing the temperatures and pressures of the system over a period of 30 minutes after any change in compressor or condenser fan speed in the case of “MIT Chiller” data set while a duration of 15-20 minutes was used in the case of “MI DX” data set.

### 4.4 Calibration of Pressure Transducers

The pressure transducers that were installed on the test stand sensors drifted from the manufacturer end-point curve due to continuous and sometimes pulsating exposure to high pressures over more than a year. Therefore, calibration of the transducers was performed using the Mensor CPB5000 dead weight tester. A least squares curve was fitted on the experimental data. The coefficients for conversion from voltage to pressure along with their accuracy for the pressure transducers installed on the test stand are given in Table 4.3.

Table 4.3: Conversion coefficients for the pressure transducers

| **Location** | **Name** | **Voltage Output** | **Multiplier (Psi/mV)** | **Offset (Psi)** | **RMSE (Psi)** |
|---|---|---|---|---|---|
| $P_{dis}$ | Measurement Specialties SSI-500 | 0-100mV | 4.977 | 1.55 | 0.695 |
| $P_{cond_{out}}$ | Honeywell MLH-500 | 0-5000mV | 123.9 | -63.1 | 0.646 |
| $P_{evap_{in}}$ | Honeywell MLH-500 | 0-5000mV | 124.7 | -63.83 | 0.718 |
| $P_{suc}$ | Measurement Specialties SSI-500 | 0-100mV | 4.945 | -6.467 | 0.719 |

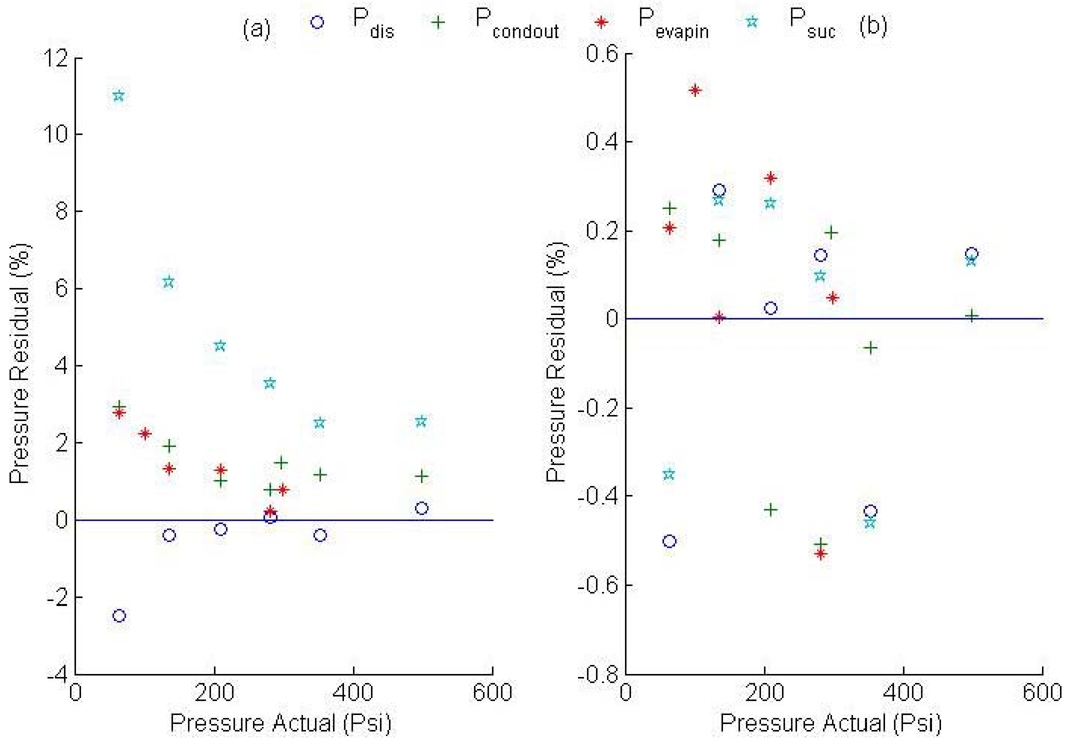


Figure 4.3: (a) Pressure residuals before calibration (b) Pressure residuals after calibration

It can be observed from Figure 4.3(a) that the measurement error in the readings of the suction and evaporator inlet transducers was around 5% or more which increases with increasing pressure. After calibration these errors have been minimized to within ±1%. The procedure for calibration is described in Appendix F.

## 4.5 Condenser Fan Characterization

Flow hood testing on the variable speed condenser fan was performed using TSI air flow hood. The purpose was to accurately determine the fan curves for air flow and power as a function of condenser fan speed. An infra-red sensor from Banner Engineering was used to detect each pass of marked fan blade. Yokogawa 1600 was used to measure three phase power with the flow hood placed on the outlet of the condenser fan.

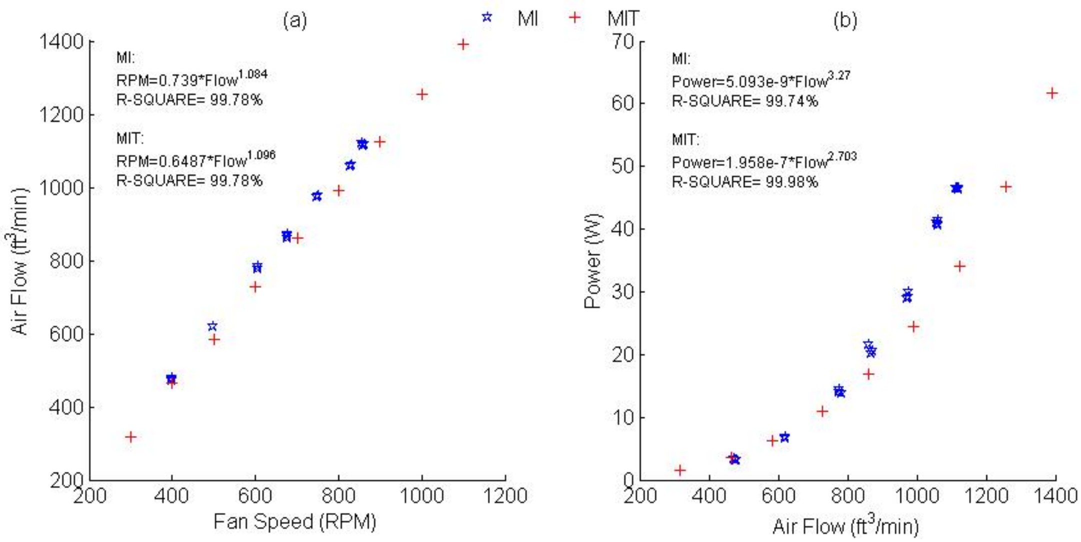


Figure 4.4: Condenser fan characterization

A comparison with the fan flow and power data of (Gayeski, 2010) is shown in Figure 4.4. It can be observed that the air flow for a given condenser fan speed is higher for the condenser fan installed in the test stand.

## 4.6 LEV Control Verification

Experimental data was acquired for testing LEV control effectiveness for a range of compressor speeds. The LEV control is achieved using a 12V stepper motor provided with the outdoor unit. The stepper motor is controlled by a microcontroller which sends pulses to the motor. The microcontroller in turn is commanded from the CR1000 using time-based digital signal. It is estimated that the time for the expansion valve to move from its full open to full close position or vice versa is 965msec for pulse frequency of 333.33Hz or pulse period of 3msec.

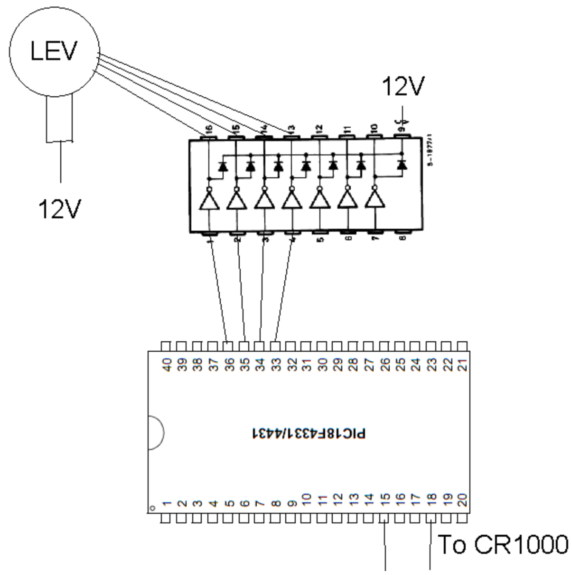


Figure 4.5: LEV control circuit schematic (Arslan Khalid, 2011)

Figure 4.5 describes the LEV control circuit schematic. The CR1000 sends the direction signal to the microcontroller for a certain time determined by the control algorithm. The valve is brought to its desired position through the amount of time the signal is ON. No signal is sent by the CR1000 if the error corresponds to 3msec or less as the pulse period of the microcontroller is 3msec. Proportional, Integral and Derivative (PID) control was implemented using Zeigler-Nichols method with a sampling control time (CT) of 2sec. The PID control equation described in (Willingham, 2009) is given in Equation 4.6.1:

$$\text{Change in Valve Position } u(t) = K_c * \left(e(t) + \frac{1}{T_i} * S(t) + \frac{T_d}{CT} * \big(e(t) - e(t-1)\big)\right. \quad (4.6.1)$$

where,

$$e(t) = T_{superheat_{set}} - T_{superheat} \quad (4.6.2)$$

$$T_{superheat} = T_{suc} - T_{suc_{sat}} \quad (4.6.3)$$

$$S(t) = S(t-1) + CT * e(t) \quad (4.6.4)$$

The term S(t) is the integrator or sum of errors at time 't'. A problem encountered in PI or PID control is of integral windup. Integral windup occurs when the valve is at its maximum or minimum position but the error is still non-zero. This causes the integral to keep on summing the errors. When the sign of the error changes the change in valve position due to summing causes the valve to start oscillating between its extremes resulting in unstable control. In the current control algorithm, the integral term is set to zero whenever the valve is at its extremes i.e. the value of u(t) is 965 or zero. Note that after some hours of operation, the actual position may drift from the calculated value. Therefore, the valve is closed periodically to eliminate the drift.

Experimentation in chiller mode was conducted to determine the parameters for the PID control equation. The steady state during the experiment for determining control parameters and testing the accuracy of LEV control was established by maintaining a constant chilled water outlet temperature by varying heating load. The heating load is varied using a variable power supply which controls the power of the electrical resistor. Following the Ziegler-Nicholas method of tuning, the ultimate gain was found to be 8.5 while the ultimate period was around 90sec. The coefficients of the PID control equation are given in Table 4.4:

Table 4.4: PID control parameters

| | |
|---|---|
| Proportional Constant ($K_c$) | 5 |
| Integral Time ($T_i$) | 45 |
| Derivative Time ($T_d$) | 11.25 |

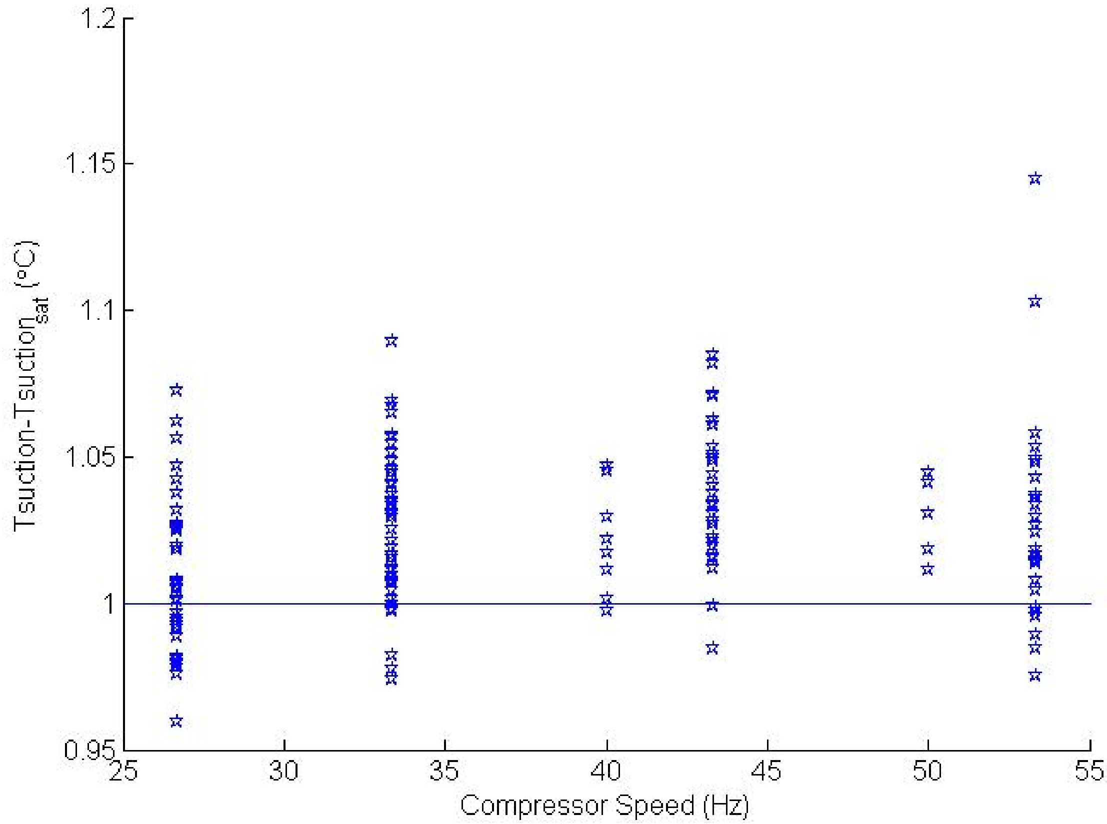


Figure 4.6: LEV control accuracy with suction superheat as control variable

Figure 4.6 shows the accuracy of maintaining a constant suction superheat for a range of compressor speeds. We can observe that the control error is less than 0.1°C for majority of the data points for a suction superheat set point of 1°C.

### 4.7 DX Mode Operation for Component Models Verification

The test stand was operated under DX mode to acquire data for validation of component models over a range of compressor speeds, outdoor fan speed and zone temperatures. A superheat of 0K was maintained through the LEV control within an error of ±0.5K. The error in the superheat for DX mode was higher because the control time was 5sec which was later changed to 2sec in chiller mode of operation. The steady state after change of compressor speed was attained by observing the superheat. The steady state after change of outdoor fan speed was attained by observing the discharge temperature. The steady discharge temperature was observed to be within ±0.5K. The steady state time after change of compressor speed was approximately 15-20 minutes. The steady state was achieved within 10-15 minutes after change in outdoor fan speed. The data from the experiment is provided in Appendix G.

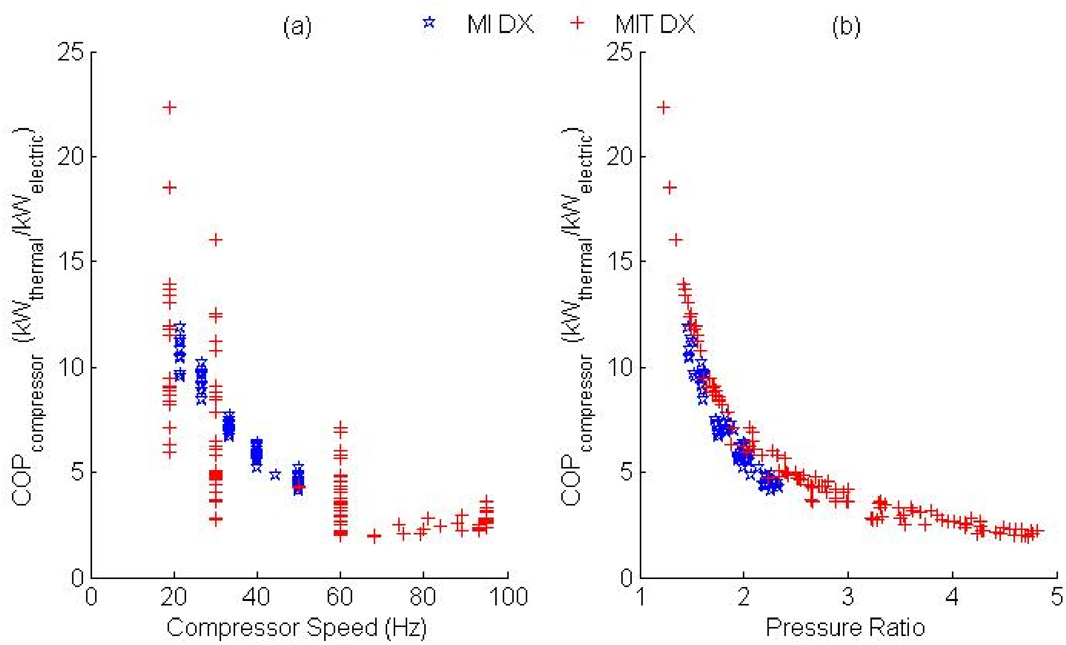


Figure 4.7: System COP plotted against (a) Compressor speed and (b) Pressure ratio

Figure 4.7(a) presents the system COP for a range of compressor speeds. The COP of system increases considerably at lower speeds. The increase in system COP with pressure ratio as shown in Figure 4.7(b) follows a more distinct profile than as a function of speed because COP is a strong function of pressure ratio.

## 4.8 Chiller Mode Operation for Component Models Verification

The test stand was operated under DX mode to acquire data for validation of component models over a range of compressor speeds, outdoor fan speed and zone temperatures. A superheat of 1K was maintained through the LEV control within an error of ±0.2K. The steady state after change of compressor speed was attained by observing the superheat. The steady state after change of outdoor fan speed was attained by observing the discharge temperature. The steady state discharge temperature error was observed to be within ±0.5K.

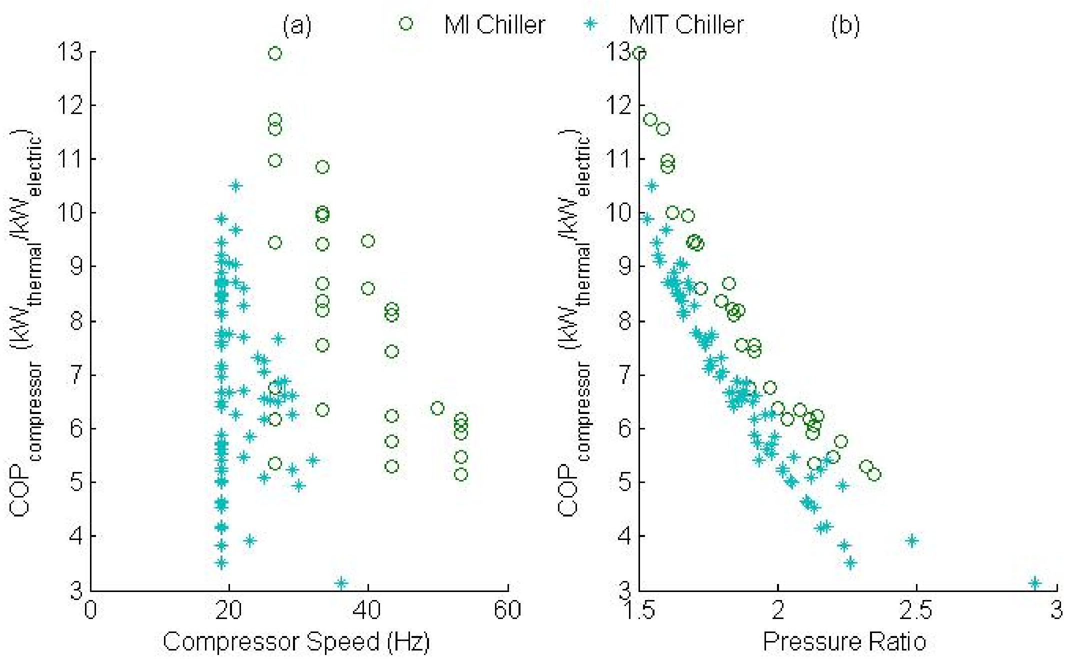


Figure 4.8: System COP plotted against (a) Compressor speed and (b) Pressure ratio

Figure 4.8 presents the system COP for a range of compressor speeds and pressure ratios. The data from the experiment is provided in Appendix H.

### 4.9 Energy Balance Check for the Experimental Data Set

For testing instrumentation accuracy and steady state condition of the system for a given set of conditions, energy balance was performed on the experimental data set. The energy balance check was carried out on individual components of the system and on the whole system. Energy balance check was not performed on the fan-coil evaporator for MI DX data set due to unavailability of $\Delta T_{evap_{air}}$ for the experimental data acquired from the test stand. Energy balance on condenser for the MI DX data set was not performed due to inaccurate estimation of condenser fan speed in DX mode of operation. The compressor power shown in the figures is the three phase electrical compressor power after the variable frequency drive. The mass flow rate of refrigerant for "MIT DX" data set is calculated from the refrigerant side energy balance on the evaporator. The oil concentration is taken as 1% in the enthalpy mixture model as mentioned in ("Hermetic Compressors," 2011) for small hermetic rotary compressors. The discharge and suction enthalpies are calculated using Equation 3.2.14 while condenser outlet, evaporator inlet and evaporator outlet enthalpies are calculated using Equation 3.2.13. The energy balance equations for the individual components and for the system are given in Equations 4.9.1-4.9.4:

For compressor:

$$\text{Compressor Power} = \dot{m}_{ref-oil} * (h_{dis} - h_{suc}) \tag{4.9.1}$$

For condenser:

$$\dot{m}_{ref-oil} * \left(h_{dis} - h_{cond_{out}}\right) = \dot{m}_{air_{cond}} * cp_{air@T_x,P_{amb}} * dT_{cond_{air}} \tag{4.9.2}$$

For fan-coil evaporator:

$$\dot{m}_{ref-oil} * \left(h_{evap_{out}} - h_{evap_{in}}\right) = \dot{m}_{air_{evap}} * cp_{air@T_z,P_{amb}} * dT_{cond_{air}} \tag{4.9.3}$$

For brazed-plate evaporator:

$$\dot{m}_{ref-oil} * \left(h_{evap_{out}} - h_{evap_{in}}\right) = \dot{m}_{water} * (h_{water_{in}} - h_{water_{out}}) \qquad (4.9.4)$$

For system:

$$\dot{m}_{ref-oil} * \left(h_{dis} - h_{cond_{out}}\right) = \dot{m}_{ref-oil} * (h_{dis} - h_{suc}) + \dot{m}_{ref-oil} * \left(h_{evap_{out}} - h_{evap_{in}}\right) \qquad (4.9.5)$$

### 4.9.1 DX Mode Operation

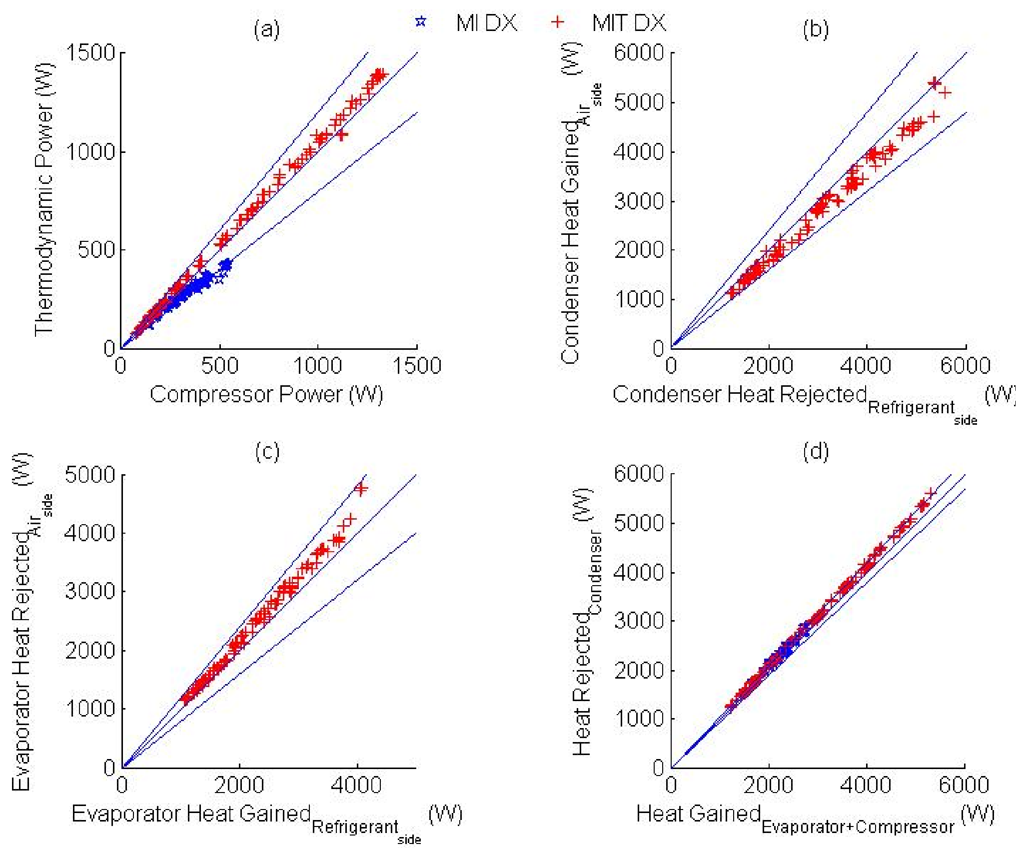


Figure 4.9: (a) Compressor energy balance check (b) Condenser energy balance check (c) Fan-coil evaporator energy balance (d) System energy balance check. Lines at ±20% are shown in (a)-(c) and at ±5% in (d)

The energy balance checks for individual components and the whole system for chiller mode operation are shown in Figure 4.9. A difference in the compressor energy balance of the two data sets is observed in Figure 4.9(a). This can be because the heat load on the evaporator varied in "MI DX" data set depending on zone temperature which was influenced by outdoor weather. In Figure 4.9(b), the heat rejected by the refrigerant is always higher than the heat gain by the air which can be attributed to error in estimation of air mass flow rate, pressure and temperature measurements or oil fraction.

In Figure 4.9(c), energy balance on the fan-coil evaporator is shown. The difference between heat rejected by air and heat gained by refrigerant can be attributed to error in pressure and temperature measurements. The comparison between heat rejected by fin-tube condenser and the system heat input presented in Figure 4.9(d) shows that the error in the system energy balance is within ±5%.

### 4.9.2 Chiller Mode Operation

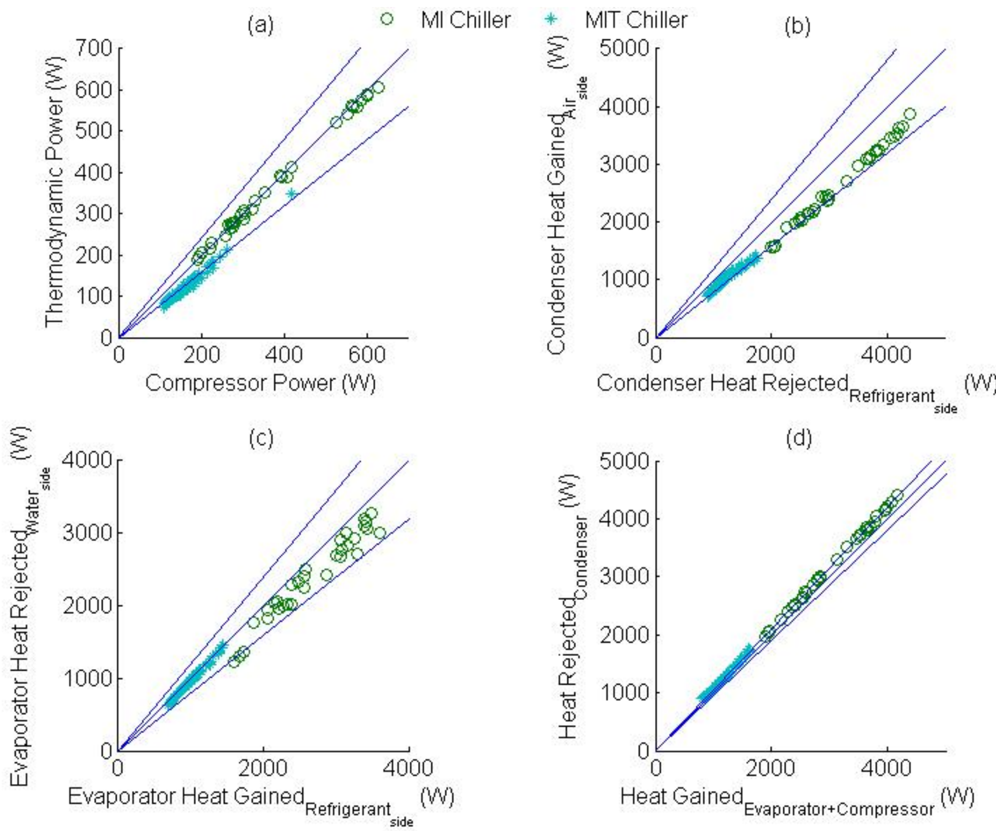


Figure 4.10: (a) Compressor energy balance check (b) Condenser energy balance check (c) Brazed-plate evaporator energy balance (d) System energy balance check. Lines at ±20% are shown in (a)-(c) and at ±5% in (d)

The energy balance checks for individual components and the whole system for chiller mode operation are shown in Figure 4.10. In Figure 4.10(a) a higher error in the energy balance can be observed because of changing evaporator load as explained in section 4.3. In Figure 4.10(b), the heat rejected by the refrigerant is always higher than the heat gain by the air which can be attributed to error in estimation of air mass flow rate, pressure and temperature measurements or oil fraction.

In Figure 4.10(c), energy balance on the brazed-plate evaporator is shown. The difference between heat rejected by water and heat gained by refrigerant can be attributed to error in measurement of water mass flow rate. Despite the errors present in the component energy balance metrics, the system energy balance is obtained to within ±5% as shown in Figure 4.10(d).

# CHAPTER 5

# Experimental Validation of Models

## 5.1 Compressor Model

In Figure 5.1(a) and (b), it can be observed that the accuracy of prediction for compressor speeds from the model is within ±15% over a range of compressor speeds. The compressor power prediction accuracy is within ±20% at lower speeds as can be observed in Figure 5.1(d) which is the area of interest for low-lift operation. However, for higher speeds the power is over-predicted by the model. This can be because the model doesn't account for heat transfer between suction and discharge which becomes significant at high discharge temperatures occurring at high compressor speeds. Due to heat transfer, the specific volume at suction increase resulting in a lower mass flow and consequently lower compressor power. However, the current model doesn't include the effect of heat transfer on suction resulting in a significant over-prediction of compressor power as can be seen in Figure 5.1(b) and (d).

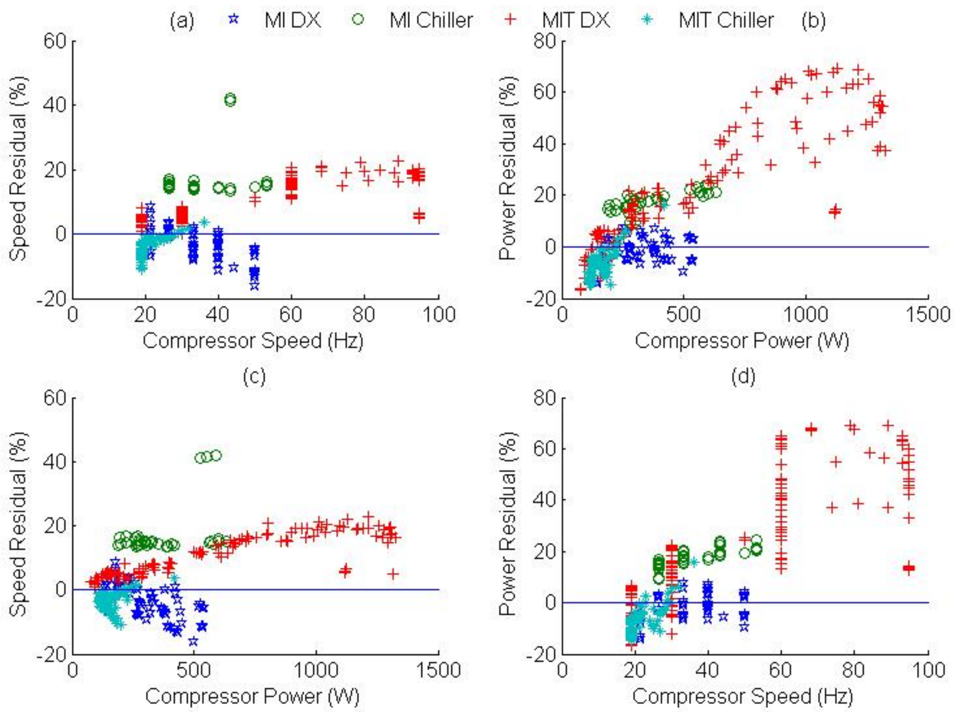


Figure 5.1: (a) Compressor speed residual vs. compressor speed (b) Compressor speed residual vs. compressor speed (c) Compressor power residuals vs. compressor power (d) Compressor power residuals vs. compressor power

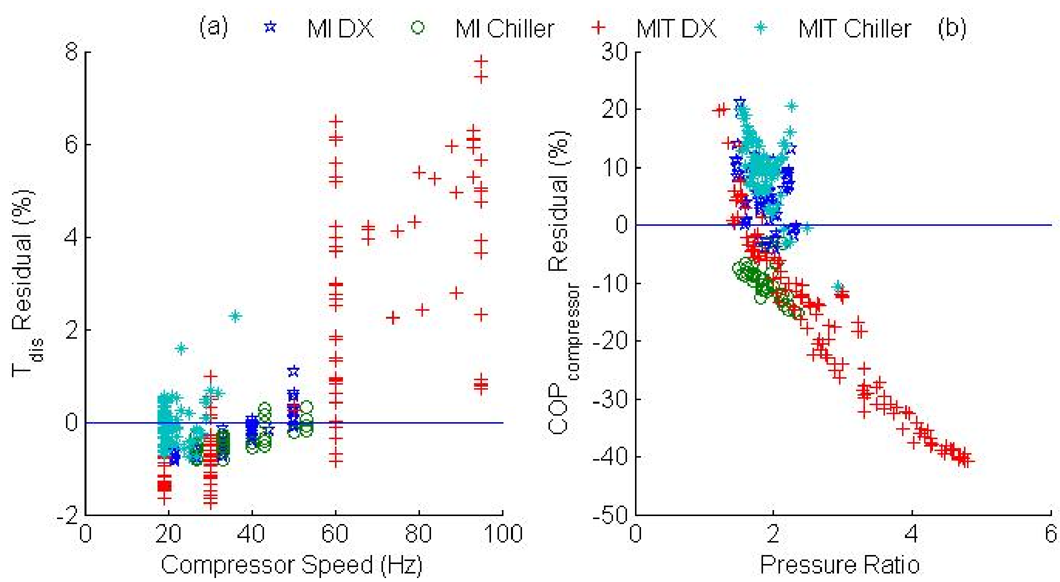


Figure 5.2: (a) $T_{dis}$ residuals vs. compressor speed (b) COP compressor residuals vs. pressure ratio

The prediction of compressor power at lower speeds can be improved by accounting for additional power due to pressure loss in the valves. Figure 5.2(a) shows that the model is able to describe discharge temperatures fairly accurately. However, for high compressor speeds, the discharge temperature is over predicted because of over-prediction of compressor power by the model.

As compressor is the main power consuming component of the system, the COP of compressor is evaluated to estimate the accuracy of estimating compressor performance at low-lift conditions. The compressor COP is evaluated from Equation 5.1.1:

$$\mathrm{COP_{compressor}} = \frac{\mathrm{Q_{load}}}{\text{Compressor Power}} \tag{5.1.1}$$

It can be observed from Figure 5.2(b) that compressor performance residuals are within ±20% for low-lift operation.

A comparison between the results obtained from the current compressor model and the compressor model presented in (Zakula, 2010) is provided in Table 5.1 in terms of Root Mean Squared Percentage Error (RMSPE) and Root Mean Squared Error (RMSE) in brackets. The current model uses the same mass flow rate and power model of (Zakula, 2010), however, the effect of oil is modeled differently. In (Zakula, 2010), a constant specific heat is taken for the oil in the compressor model while in the current study oil properties are evaluated as a function of temperature.

Table 5.1: Comparison of output parameters of current compressor model and model of (Zakula, 2010)

| | **Current Model** | | | | **Model of (Zakula, 2010)** | | | |
|---|---|---|---|---|---|---|---|---|
| **Parameter** | **MI DX RMSPE (RMSE)** | **MI Chiller RMSPE (RMSE)** | **MIT DX RMSPE (RMSE)** | **MIT Chiller RMSPE (RMSE)** | **MI DX RMSPE (RMSE)** | **MI Chiller RMSPE (RMSE)** | **MIT DX RMSPE (RMSE)** | **MIT Chiller RMSPE (RMSE)** |
| $f_{comp}$ % (Hz) | 8.565 (3.67) | 13.413 (5.53) | 12.286 (8.983) | 6.271 (1.23) | 14.016 (6.273) | 14.012 (5.808) | 20.601 (15.69) | 5.962 (1.173) |
| Compressor Power % (kW) | 6.626 (0.021) | 11.731 (0.054) | 34.627 (0.353) | 10.074 (0.016) | 15.181 (0.062) | 10.646 (0.047) | 24.803 (0.248) | 10.508 (0.016) |
| $T_{dis}$ % (K) | 0.519 (1.682) | 0.476 (1.565) | 2.947 (10.897) | 0.51 (1.704) | 2.367 (7.716) | 0.908 (3.031) | 3.22 (12.038) | 1.48 (4.866) |
| COP Compressor % (kW/kW) | 7.379 (0.591) | 10.372 (0.777) | 23.176 (0.931) | 11.422 (0.845) | 20.815 (1.159) | 9.537 (0.734) | 18.469 (0.832) | 12.001 (0.87) |

It can be observed from Table 5.1 that the accuracy in prediction of compressor parameters by the current model is better than that of model (Zakula, 2010). The higher RMSE of current model for compressor power in "MIT DX" can be attributed to the use of incorrect oil density which is calculated from property equations developed for POE/VG68. However, the oil that is used in the compressor of the experimental setup is POE/VG22. The oil density of POE/VG68 can differ from POE/VG22 at higher temperatures encountered in the data set of MIT DX. The equations for calculation of the thermodynamic properties of POE/VG22 were not found in the literature.

## 5.2 Condenser Model

Figure 5.3(a) describes the accuracy of prediction of effectiveness by the condenser model for a given set of $P_{dis}$, $T_{dis}$, $T_x$, $\dot{m}_{ref}$ and $\dot{V}_{air}$. The condenser effectiveness is calculated using Equation 5.2.1:

$$\varepsilon_{cond} = \frac{\text{Condenser Heat Rejected}}{\dot{m}_{air_{cond}} * cp_{air@T_x,P_{amb}} * (T_{dis} - T_x)} \qquad (5.2.1)$$

It can be observed that the model predicts the effectiveness within ±5% for the data sets of "MIT DX" and "MI Chiller" in which a constant heat load was applied. In Figure 5.3(b), the data sets obtained from the test stand in chiller mode are shown only. This is because the $P_{cond_{out}}$ data was not present in the DX mode operation in the data set of (Gayeski et al., 2010) and the location of $P_{cond_{out}}$ transducer in DX mode operation of the MI test stand was after the refrigerant level indicator which resulted in inaccurate measurement of condenser outlet pressure. This was later rectified in chiller mode operation. For the data set shown in Figure 5.3(b), the pressure at the condenser outlet is slightly under predicted because the pressure transducer is not located exactly at the exit of the condenser. For the MI test stand, the transducer for measuring condenser outlet pressure is located approximately 1.5m after the outlet of the condenser as shown in Figure 4.1.

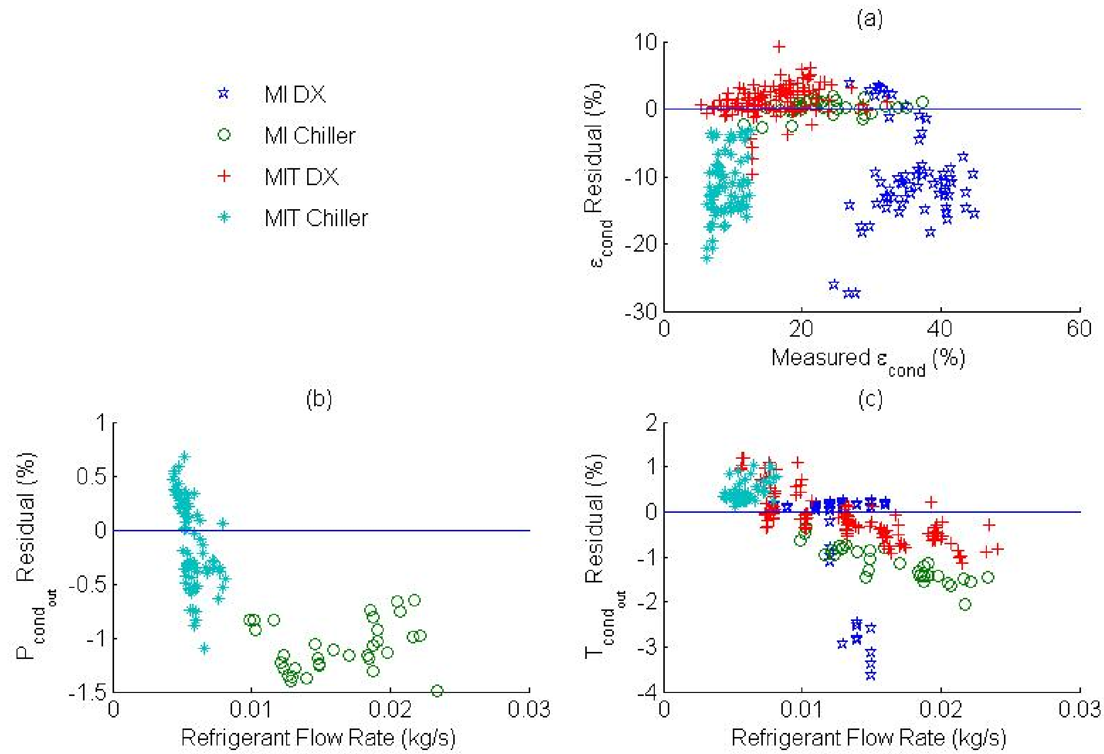


Figure 5.3: (a) $\varepsilon_{\text{cond}}$ residuals vs. measured $\varepsilon_{\text{cond}}$ (b) $P_{\text{cond}_{\text{out}}}$ residuals vs. refrigerant flow rate (c) $T_{\text{cond}_{\text{out}}}$ residuals vs. refrigerant flow rate

Figure 5.3(c) shows that the temperature at condenser outlet is under predicted by the model for majority of data points. In the experimental data obtained from the test stand, this under prediction increases substantially for some data points in the "MI DX" data set. This can be attributed to inaccurate estimation of air mass flow rate and non-uniform air flow distribution. It was found that some air was getting bypassed from the condenser coil due to leaks in the condenser frame after the coil. This was later rectified and the $T_{\text{cond}_{\text{out}}}$ residuals decreased as can be observed in the "MI Chiller" data set. Due to these experimental errors, "MI DX" is not used for assessment of condenser model performance.

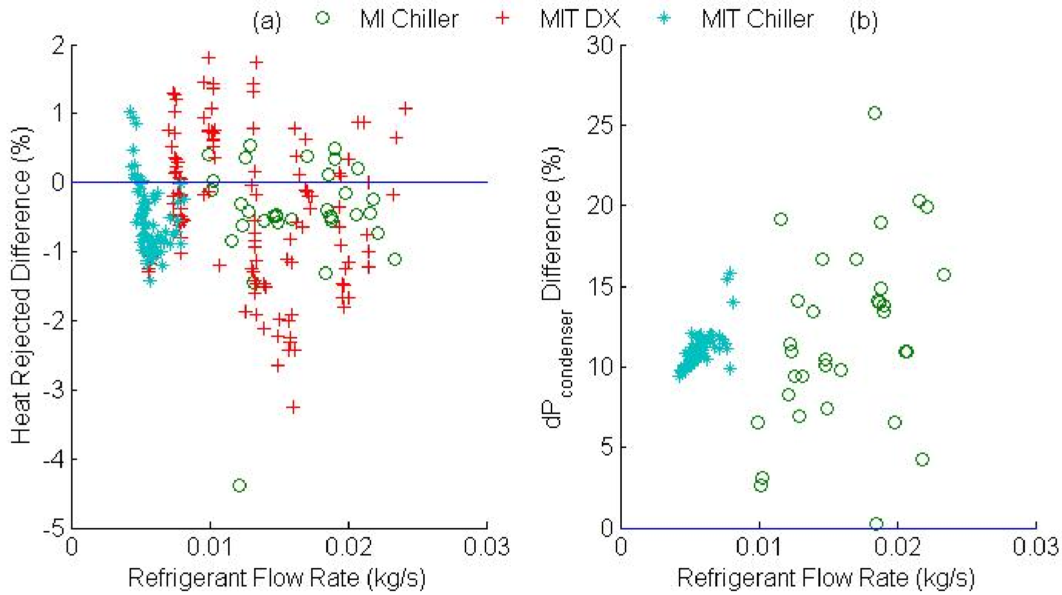


Figure 5.4: (a) Heat rejected and (b) $dP_{cond}$difference between no oil and 1% oil

Figure 5.4 shows that the condensation heat transfer is decreased when oil is included in the model for majority of the data points while increasing the pressure drop across the heat exchanger. A comparison between the results obtained from the current condenser model and the condenser model presented in (Zakula, 2010) is provided in Table 5.2. The model presented in (Zakula, 2010) adopts a zone-by-zone approach explained in Chapter 2. Therefore, a representative heat transfer coefficient and friction factor is calculated for de-superheating, condensation and sub-cooling region. The model uses film condensation correlation and Pierre's correlation for complete evaporation for modeling two-phase heat transfer. For two-phase pressure drop correlations, an improved version of Pierre's model developed by Choi, Kazerski and Domanski are used (Zakula, 2010). The effect of oil on condenser performance is accounted in calculation of pressure drop. The condenser model presented in (Zakula, 2010) solves for the condenser inlet pressure and condensation zone fraction to satisfy the energy balance while air flow rate is varied in the current model to satisfy the energy balance for the given set of input parameters described in Table 3.4.

Table 5.2: Comparison of output parameters of current condenser model and model of (Zakula, 2010)

| | **Current Model** | | | **Model of (Zakula, 2010)** | | |
|---|---|---|---|---|---|---|
| **Parameter** | **MI Chiller RMSPE (RMSE)** | **MIT DX RMSPE (RMSE)** | **MIT Chiller RMSPE (RMSE)** | **MI Chiller RMSPE (RMSE)** | **MIT DX RMSPE (RMSE)** | **MIT Chiller RMSPE (RMSE)** |
| $P_{cond_{out}}$ % (kPa) | 1.934 (47.578) | — | 0.443 (8.319) | 2.376 (62.385) | — | 3.559 (65.842) |
| $dP_{cond}$ % (kPa) | 281.756 (51.557) | — | 54.309 (8.319) | 236.265 (72.91) | — | 422.866 (65.842) |
| $T_{cond_{out}}$ % (K) | 0.773 (2.377) | 0.745 (2.256) | 0.366 (1.097) | 0.183 (0.567) | 0.316 (0.974) | 0.306 (0.92) |
| $dT_{cond}$ % (K) | 10.657 (2.377) | 8.422 (2.256) | 5.097 (1.097) | 2.354 (0.567) | 2.122 (0.974) | 4.368 (0.92) |
| $\varepsilon_{cond}$ % (%) | 2.025 (0.657) | 1.182 (0.289) | 6.969 (0.506) | 3.033 (0.642) | 2.489 (0.396) | 0.714 (0.066) |

Table 5.2 shows that the prediction accuracy of the current model is better than that of (Zakula, 2010). However, the RMSE for temperature predictions is higher. These errors can be because of using incorrect oil properties equations such as viscosity, surface tension and thermal conductivity or oil concentration. It is reported in (Hambraeus, 1995) that a miscible oil of lower viscosity increases the heat transfer coefficient as compared to a miscible oil of higher viscosity. In the test stand, VG22 oil is used while only VG68 oil properties were found in literature. The higher viscosity oils results in an under prediction of condenser outlet temperature for the data sets of "MIT DX" and "MI Chiller" in which a constant heat load was applied as can be seen in

Figure 5.3(c). The effect of oil concentration on condenser output parameters is presented in Figure 5.10.

## 5.3 Fan-Coil Evaporator Model

"MIT DX" data set is used for fan-coil evaporator model validation due to unavailability of evaporator air-side temperature measurements in the data set of "MI DX". The current model accurately predicts the heat exchanger effectiveness to within ±10% for a given set of $P_{evap_{in}}$, $T_{evap_{in}}$, $x_{evap_{in}}$, $T_z$, $\dot{m}_{ref}$ and $\dot{V}_{air}$ as shown in Figure 5.5(a).

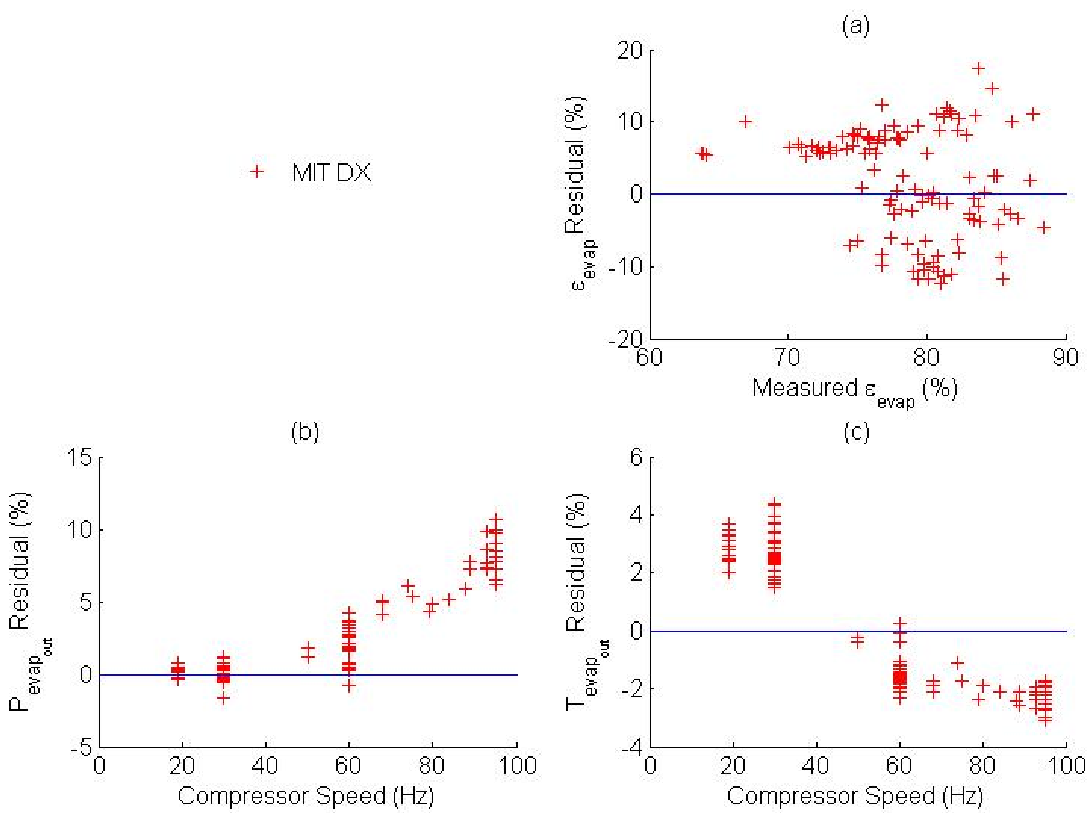


Figure 5.5: (a) $\varepsilon_{evap}$ residuals vs. measured $\varepsilon_{evap}$ (b) $P_{evap_{out}}$ residuals vs. compressor speed (c) $T_{evap_{out}}$ residuals vs. compressor speed

The evaporator effectiveness is calculated using Equation 5.3.1:

$$\text{Evaporator Effectiveness} = \frac{\text{Evaporator Heat Gained}}{\dot{m}_{\text{air}_{\text{evap}}} * cp_{\text{air@T}_z,\text{P}_{\text{amb}}} * (T_z - T_{\text{evap}_{\text{in}}})} \tag{5.3.1}$$

In Figure 5.5(b), the pressure at evaporator outlet is over predicted for majority of data points. This over prediction increases considerably for data points at and above compressor speed of 60Hz. This can be because of increase in oil concentration which results in a higher pressure drop. This phenomenon can be observed in Figure 5.5(c) as the suction temperature is under predicted by the model at higher speeds. It is to be noted that the evaporator outlet pressure and temperature are measured at compressor suction resulting in higher residuals for these parameters.

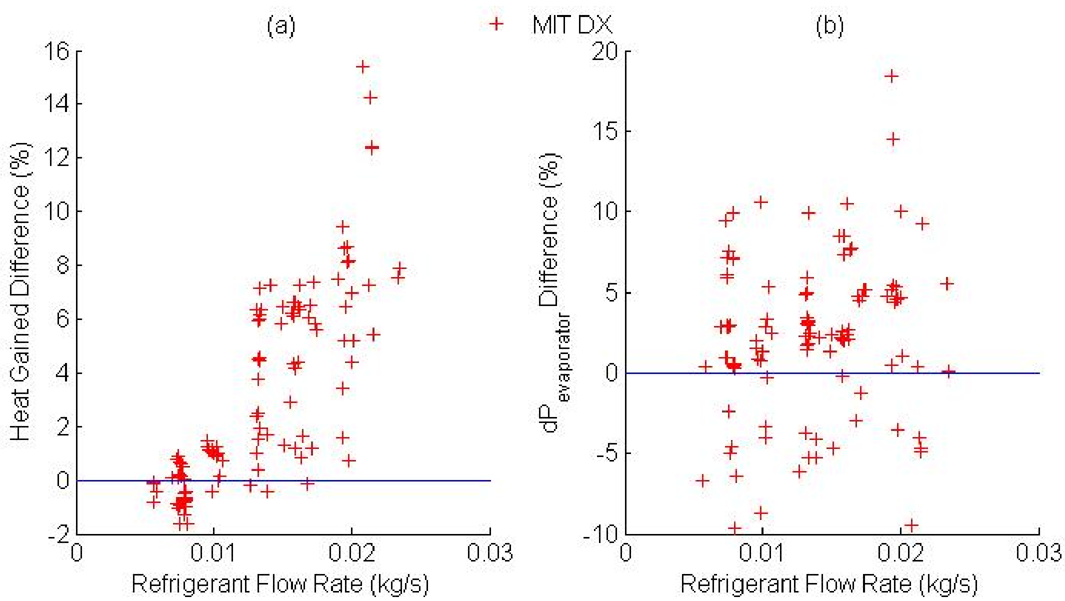


Figure 5.6: (a) Heat rejected and (b) $dP_{evap}$difference between no oil and 1% oil

In Figure 5.6(a), no distinct trend of oil is seen on evaporation heat transfer estimation by the model for low refrigerant flow rates. However, at high refrigerant flow rates an increase in heat transfer is estimated. The pressure drop was found to increase by inclusion of oil as shown in

Figure 5.6(b). The effect of oil concentration on evaporator parameters estimation is shown in Figure 5.11.

A comparison between the results obtained from the current evaporator model and the evaporator model presented in (Zakula, 2010) is provided in Table 5.3. The fan-coil evaporator model presented in (Zakula, 2010) is modeled similar to the condenser model of (Zakula, 2010). However, convergence is achieved by searching for refrigerant mass flow rate, evaporator inlet temperature and evaporation zone fraction while air flow rate is searched in the current model to satisfy the energy balance for the given set of input parameters described in Table 3.6.

Table 5.3: Comparison of output parameters of current fan-coil evaporator model and model of (Zakula, 2010)

| | **Current Model** | **Model of (Zakula, 2010)** |
|---|---|---|
| **Parameter** | **MIT DX RMSE (RMSPE)** | **MIT DX RMSE (RMSPE)** |
| $P_{evap_{out}}$ % (kPa) | 4.000 (29.631) | 4.132 (36.571) |
| $dP_{evap}$% (kPa) | 34.779 (29.631) | 101.816 (36.571) |
| $T_{evap_{out}}$% (K) | 2.309 (6.573) | 0.469 (1.324) |
| $dT_{evap}$% (K) | 884.831 (6.573) | 144.067 (1.324) |
| $\varepsilon_{evap}$ % (%) | 5.638 (4.424) | 1.285 (1.025) |

## 5.4 Brazed-Plate Evaporator Model

Figure 5.7(a) shows that the current model accurately predicts the heat exchanger effectiveness to within ±5% for majority of data points for a given set of $P_{evap_{in}}$, $T_{evap_{in}}$, $x_{evap_{in}}$, $T_{water_{in}}$, $\dot{m}_{ref}$ and $\dot{V}_{water}$. The brazed-plate evaporator effectiveness is calculated using Equation 5.4.1:

$$\varepsilon_{evap} = \frac{\text{Evaporator Heat Gained}}{\dot{m}_{water_{evap}} * cp_{water@T_{water_{in}},P_{amb}} * \left(T_{water_{in}} - T_{evap_{in}}\right)} \tag{5.4.1}$$

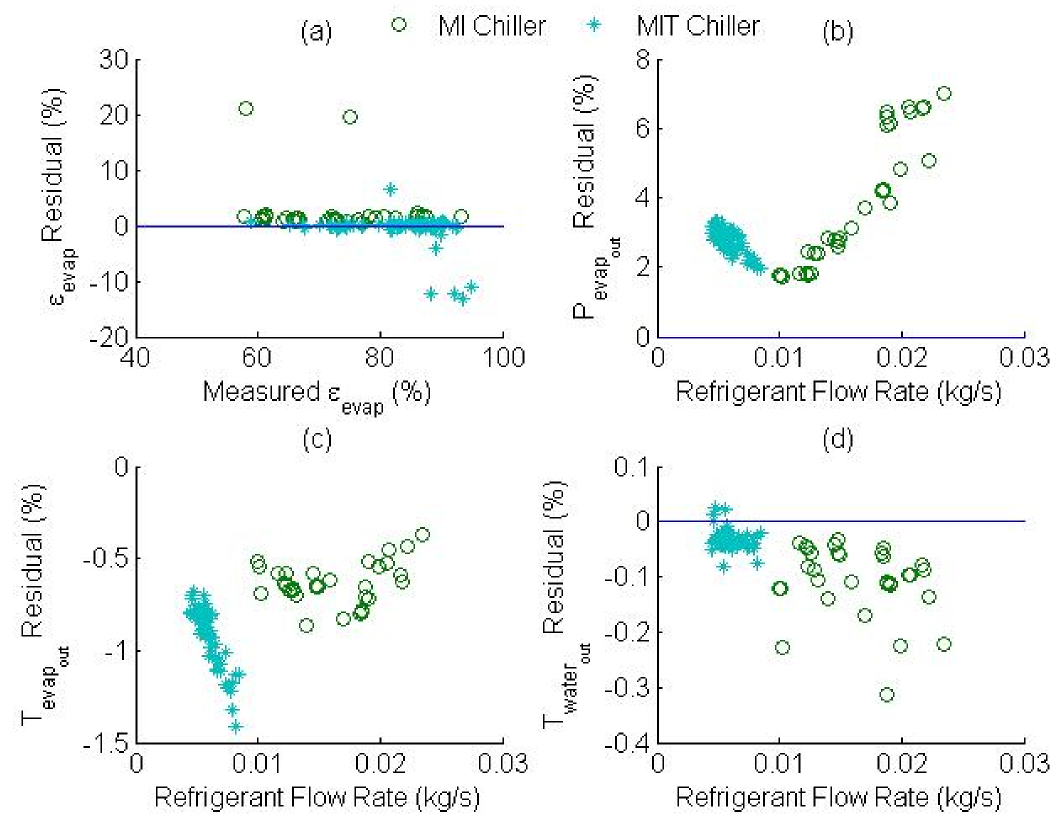


Figure 5.7: (a) $\varepsilon_{evap}$ residuals vs. measured $\varepsilon_{evap}$ (b) $P_{evap_{out}}$ residuals vs. refrigerant flow rate (c) $T_{evap_{out}}$ residuals vs. refrigerant flow rate (d) $T_{water_{out}}$ residuals vs. refrigerant flow rate

It is to be noted that the evaporator outlet pressure is measured at compressor suction resulting in higher residuals as can be seen in Figure 5.7(b).

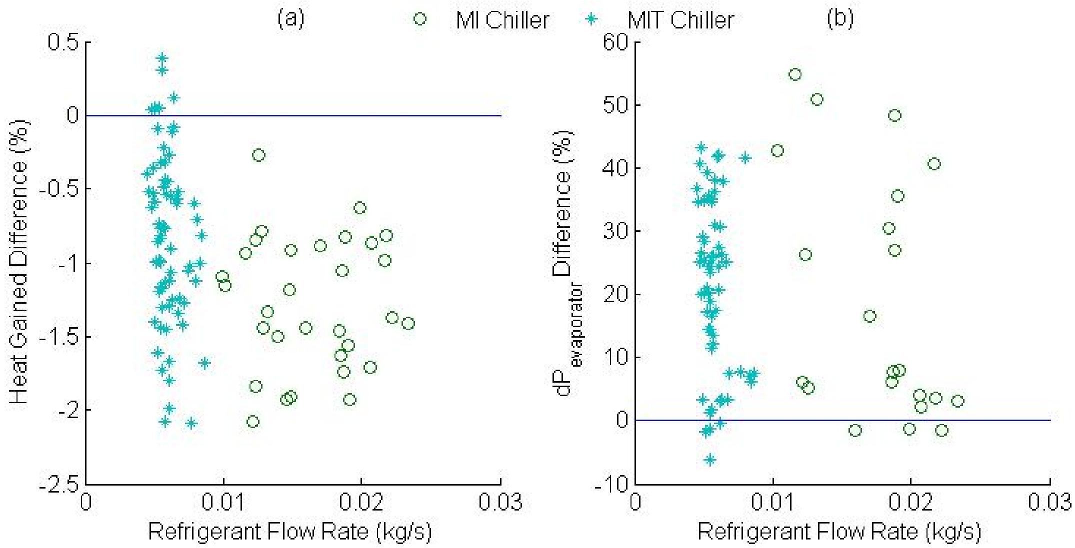


Figure 5.8: (a) Heat rejected and (b) $dP_{evap}$ difference between no oil and 1% oil

Figure 5.8 shows that heat transfer decreases with increase in pressure drop after inclusion of oil in the model. However, the contribution to the decrease in heat transfer is not that significant while increase in pressure drop is considerable. This can be attributed to the higher area density found in brazed-plate heat exchangers which eliminates the oil effect of decrease in heat transfer in the heat exchanger. However, this also increases the pressure drop due to oil in the heat exchanger.

A comparison between the results obtained from the current brazed-plate evaporator model and the brazed-plate evaporator model developed by (Zakula, 2011) is provided in Table 5.4. The brazed-plate evaporator model of (Zakula, 2011) is modeled similar to the fan-coil evaporator model of (Zakula, 2010). The correlations for single-phase heat transfer and pressure drop are the same in the current brazed-plate evaporator and the brazed-plate evaporator model of (Zakula, 2011). However, the brazed-plate evaporator model of (Zakula, 2011) uses correlation of Cooper (Cooper, 1984a) and Choi (Choi, Kedzierski, & Domański, 1999) for two-phase heat transfer and pressure drop respectively while the current model uses the correlation presented in (Hsieh & T.

F. Lin, 2002). Table 5.4 shows that the current brazed-plate evaporator model accurately predicts the parameters of the heat exchanger as compared to the model of (Zakula, 2011).

Table 5.4: Comparison of output parameters of current brazed-plate evaporator model and model of (Zakula, 2011)

| | Current Model | | Model of (Zakula, 2011) | |
|---|---|---|---|---|
| **Parameter** | **MI Chiller RMSPE (RMSE)** | **MIT Chiller RMSPE (RMSE)** | **MI Chiller RMSPE (RMSE)** | **MIT Chiller RMSPE (RMSE)** |
| $P_{evap_{out}}$% (kPa) | 4.211 (55.087) | 2.828 (28.594) | 20.787 (249.967) | 3.248 (32.258) |
| $dP_{evap}$% (kPa) | 91.995 (55.087) | 95.145 (28.594) | 357.61 (249.967) | 114.693 (32.258) |
| $T_{evap_{out}}$% (K) | 0.784 (2.299) | 0.777 (2.208) | 0.334 (0.981) | 0.325 (0.925) |
| $dT_{evap}$% (K) | 103.243 (2.299) | 80.245 (2.208) | 63.05 (0.981) | 36.003 (0.925) |
| $T_{water_{out}}$ % (K) | 0.336 (0.98) | 0.172 (0.484) | 0.247 (0.722) | 0.036 (0.103) |
| $dT_{water}$ % (K) | 50.673 (0.98) | 26.665 (0.484) | 30.573 (0.722) | 6.204 (0.103) |
| $\varepsilon_{evap}$ % (%) | 0.282 (0.211) | 0.129 (0.109) | 11.367 (5.536) | 3.082 (2.521) |

Table 5.4 shows that the prediction accuracy of the current model is better than that of (Zakula, 2010). However, the RMSE for the temperature is slightly higher. This can be because of using incorrect oil properties equations such as viscosity, surface tension and thermal conductivity which are for POE/VG68.

## 5.5 Oil Concentration Effect on Vapor Compression Components:

### 5.5.1 Compressor:

It can be observed from Figure 5.9 that in "MIT DX" data set, the errors in prediction of compressor performance decreases at higher oil concentration. It is mentioned in (Sarntichartsak et al., 2006) that oil concentration in variable speed compressor varies with compressor speed. For a hermetic rotary compressor, the oil concentration varied from 0.5% to 1% for compressor electrical frequency of 30-50Hz. However, in "MIT DX" data set the compressor electrical frequency range was 60-300Hz. Therefore, use of oil concentration equation as a function of speed may reduce the errors encountered in the component models especially for "MIT DX" data set.

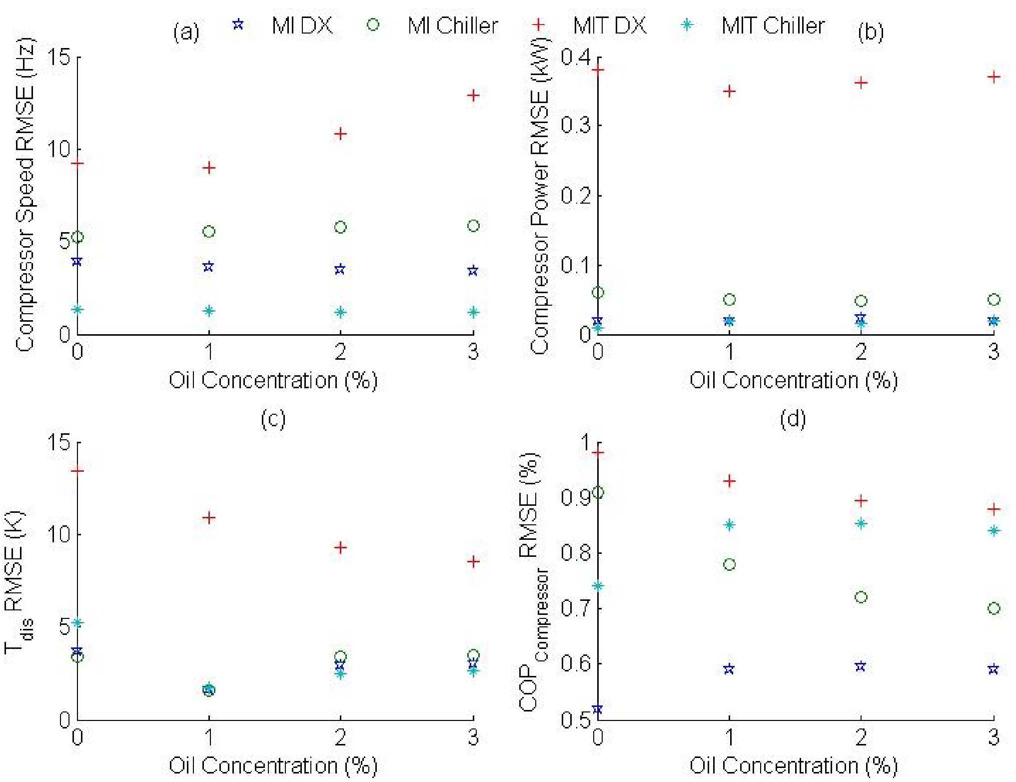


Figure 5.9: Oil concentration effect on (a) Compressor speed (b) Compressor power (c) Discharge temperature (d) Compressor COP

### 5.5.2 <u>Condenser:</u>

Figure 5.10 illustrates the effect of oil on the prediction of condenser output parameters. It can be observed from Figure 5.10(c) that an increase in oil concentration increases the effectiveness error in "MI Chiller" and "MIT DX". It was shown in Figure 5.4(a) that the heat transfer was found to decrease after inclusion of oil for majority of data points. Therefore, it can be suggested that oil tends to enhance condensation heat transfer. However at low refrigerant flow rates, oil may reduce the heat transfer slightly as can be seen by a decrease in $\varepsilon_{cond}$ RMSE in Figure 5.10(c). The error in condenser outlet pressure estimation is found to increase with oil concentration in Figure 5.10(a). This discrepancy is because of using VG68 oil properties which results in a higher pressure drop than measured. However, the effect of this is negligible at low refrigerant flow rates encountered in data set of "MIT Chiller".

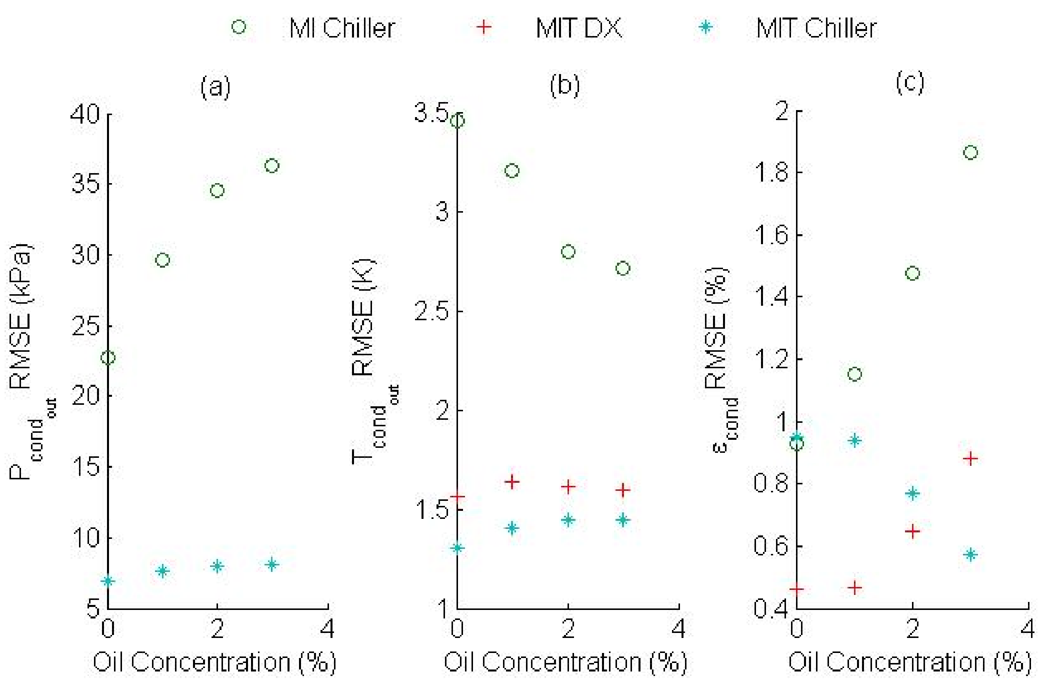


Figure 5.10: Oil concentration effect on condenser (a) Outlet pressure (b) Outlet temperature and (c) Effectiveness

### 5.5.3 Evaporator:

The effect of oil on parameter estimation by the fan-coil evaporator model and brazed-plate evaporator model is shown in Figure 5.11. For brazed-plate evaporator, the oil tends to increase heat transfer because the model predicts a decrease in heat transfer after inclusion of oil in Figure 5.8 while the effectiveness error increase with increasing oil concentration as shown in Figure 5.11(d). The effect of oil concentration on pressure drop however is negligible. The error in estimation of $\varepsilon_{evap}$ increase for the fan-coil evaporator at higher oil concentration as shown in Figure 5.11(c). However, a single oil concentration cannot represent the range of oil concentration occurring in the "MIT DX" data set as explained in section 5.5.1. Therefore, a conclusion about the effect of oil on heat transfer and pressure drop cannot be made for fan-coil evaporator.

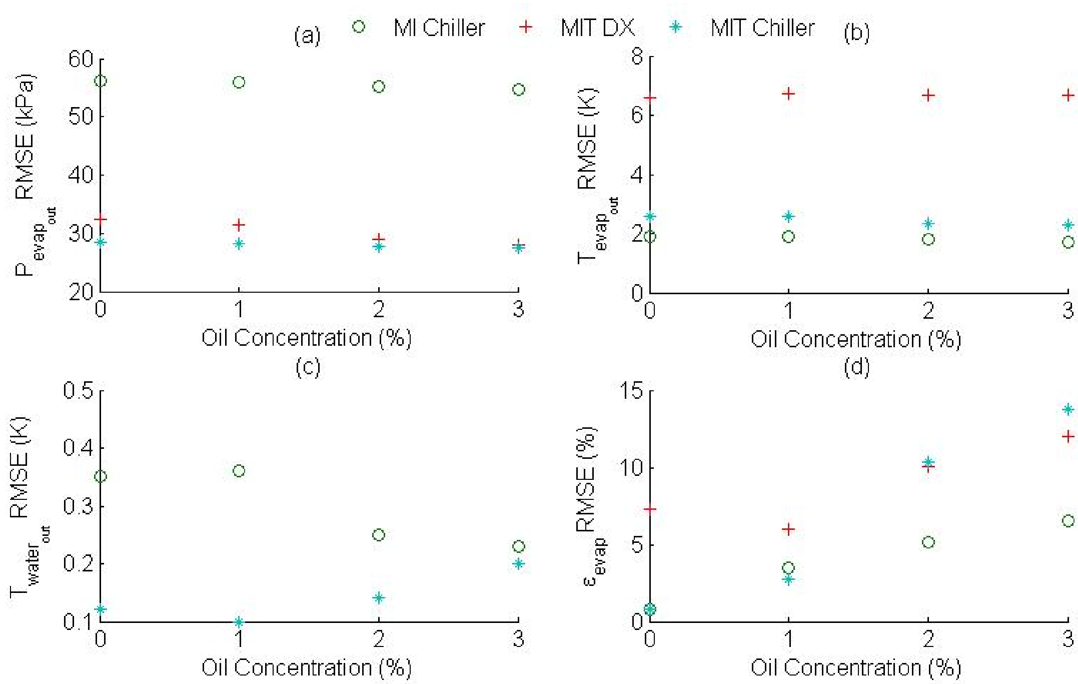


Figure 5.11: Oil concentration effect on evaporator (a) Outlet pressure (b) Outlet temperature (c) Outlet water temperature and (d) Effectiveness

## 5.6 System Model

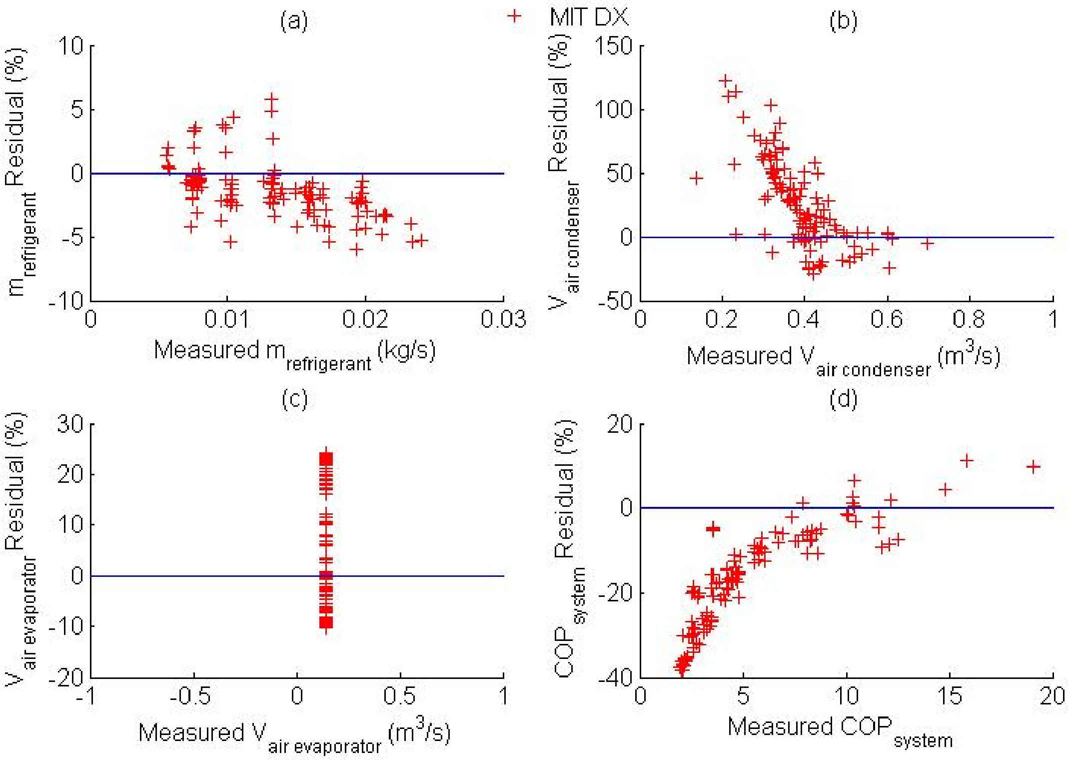


Figure 5.12: (a) Compressor speed residual vs. compressor speed (b) $\dot{V}_{air_{cond}}$ residual vs. $\dot{V}_{air_{cond}}$ (c) $\dot{V}_{air_{evap}}$ residual vs. $\dot{V}_{air_{evap}}$(d) System COP residuals vs. measured system COP

Figure 5.12 shows the accuracy of prediction of refrigerant and air flow rates by the system model. The refrigerant flow rate is predicted within an accuracy of ±5%. However, it is under-predicted for majority of data points. As shown in Figure 5.3(a) that for a given set of input parameters as described in Table 3.4 and $\dot{V}_{air}$, the condenser effectiveness is predicted within an error of ±20%. However, when the solver searches for $\dot{V}_{air}$ to satisfy the condenser energy balance, a higher $\dot{V}_{air}$ is estimated by the model resulting in over-prediction of $\dot{V}_{air}$. This over-prediction increases considerably at low air volumetric flow rates due to under-prediction of refrigerant mass flow rate and inaccuracy in prediction of compressor power by the compressor model. This is because the effect of $\dot{V}_{air}$ on heat transfer conductance given in Equation 3.4.24 is relatively smaller than the effect of $\dot{m}_{ref}$ due to two-phase heat transfer occurring on the refrigerant side. This over-prediction at lower condenser air volumetric flow rate can be also seen in Figure 5.13 (b).

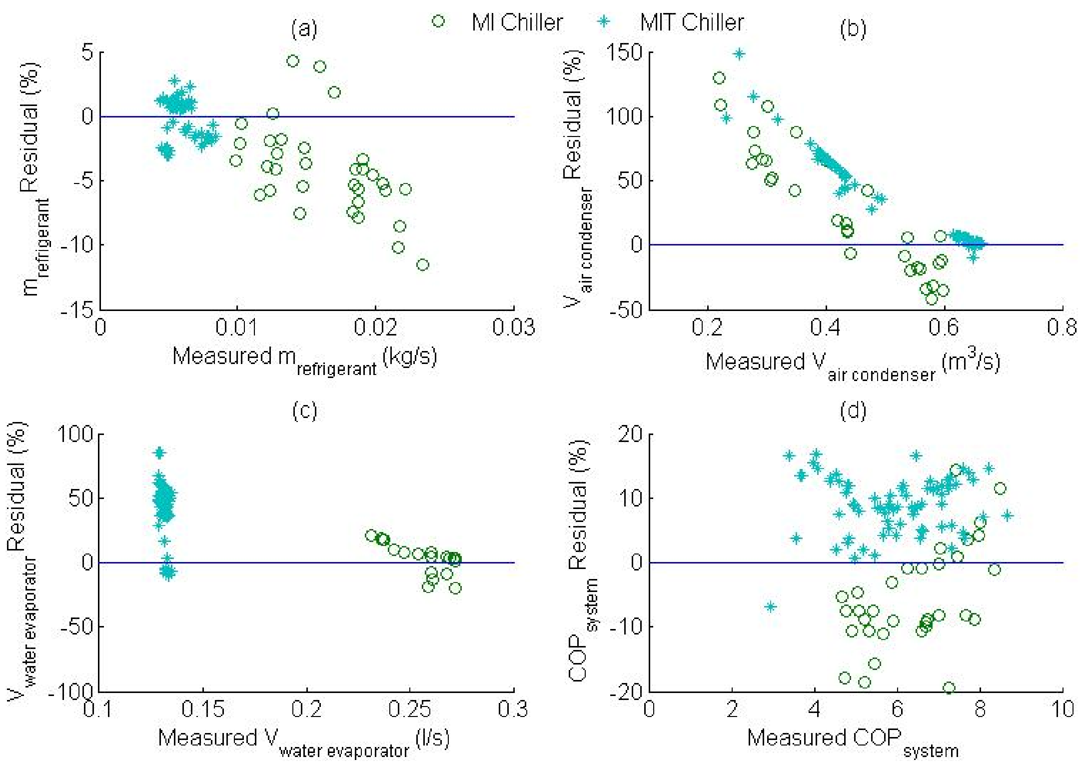


Figure 5.13: (a) Compressor speed residuals vs. measured compressor speed (b) $\dot{V}_{air_{cond}}$ residuals vs. measured $\dot{V}_{air_{cond}}$(c) $\dot{V}_{water_{evap}}$residuals vs. measured $\dot{V}_{water_{evap}}$(d) System COP residuals vs. measured system COP

Despite the higher residuals estimated at low condenser air flow rates, the system COP is predicted within ±20% for both the chiller and DX mode of operation for majority of data points as shown in Figure 5.12(d) and Figure 5.13(d). The accuracy of output parameters of system model is given in Table 5.5. Equation 5.5.1 is used for calculation of system COP:

$$\mathrm{COP_{system}} = \frac{\mathrm{Q_{load}}}{\mathrm{Compressor\ Power + Condenser\ Fan\ Power + Evaporator\ Fan/Pump\ Power}} \tag{5.5.1}$$

Table 5.5: Output parameters of system model

| Parameter | MIT DX RMSPE (RMSE) | MI Chiller RMSPE (RMSE) | MIT Chiller RMSPE (RMSE) |
|---|---|---|---|
| $f_{comp}$ % (Hz) | 9.891 (5.384) | 9.413 (3.808) | 8.703 (1.763) |
| $\dot{m}_{ref}$ % (kg/s) | 2.534 (0.0004) | 5.414 (0.001) | 1.452 (0.00008) |
| Compressor Power % (kW) | 30.223 (0.298) | 6.734 (0.027) | 12.562 (0.019) |
| $T_{dis}$ % (K) | 2.413 (8.847) | 0.904 (2.98) | 2.513 (8.157) |
| $P_{cond_{out}}$ % (kPa) | — | 1.062 (25.427) | 0.416 (7.979) |
| $dP_{cond}$ % (kPa) | — | 521.883 (25.391) | 50.087 (7.972) |
| $T_{cond_{out}}$ % (K) | 0.879 (2.661) | 1.678 (5.195) | 0.472 (1.427) |
| $dT_{cond}$ % (K) | 9.672 (2.661) | 21.118 (5.201) | 6.324 (1.453) |
| $\varepsilon_{cond}$ % (%) | 4.905 (0.008) | 0.546 (0.001) | 7.791 (0.006) |
| $T_{evap_{out}}$ % (K) | 2.351 (6.677) | 0.376 (1.102) | 0.783 (2.226) |
| $dT_{evap}$ % (K) | 747.123 (6.677) | 47.09 (1.102) | 82.726 (2.226) |
| $T_{water_{out}}$ % (K) | — | 0.142 (0.416) | 0.182 (0.512) |
| $dT_{water}$ % (K) | — | 21.776 (0.43) | 27.938 (0.516) |
| $\varepsilon_{evap}$ % (%) | 6.487 (0.052) | 14.821 (11.5) | 4.166 (3.6) |
| $\dot{V}_{air_{condenser}}$ % ($m^3/s$) | 62.862 (0.153) | 58.812 (0.175) | 69.304 (0.218) |
| $\dot{V}_{air_{evaporator}}$ % ($m^3/s$) | 14.229 (0.021) | — | — |
| $\dot{V}_{water_{evaporator}}$ % (l/s) | — | 10.564 (0.026) | 47.814 (0.063) |
| COP System % | 20.913 (0.721) | 9.235 (0.586) | 10.322 (0.606) |

## 5.7 Optimal Performance Map for Control of Compressor Speed and Outdoor Fan Speed

In order to operate the vapor compression equipment at the optimal conditions for pre-cooling control, curve fitting is performed on the data obtained from optimization presented in (Zakula, 2010). This is because the optimization time for a given set of conditions is very large and it is impractical to perform the optimization online because of the computational limitations. As shown in section 5.1-5.4 that the accuracy in prediction of output parameters of the component models presented in the current study and presented in (Zakula, 2010) is comparable. Therefore, curves for obtaining the optimum compressor speed and outdoor fan speeds were generated as a function of $T_x$, $T_z$ and $Q_{load}$ from the optimization data of (Zakula, 2010). In the current test stand speed control is not implemented over evaporator fan or pump. Therefore no curves were generated for their speed control. The optimization data of (Zakula, 2010) is used for speed control curves due to very high computational time required by the current models and failure to successfully use the optimization routines of MATLAB for system model.

Equation 5.7.1 is used to calculate the condenser fan speed from condenser volumetric flow rate. The constants in Equation 5.7.1 are determined through flow hood experiment explained in Chapter 4:

$$\text{Condenser fan speed (rpm)} = 1547 * \dot{V}_{air_{cond}}^{0.9191} \qquad (5.7.1)$$

The compressor speed obtained from the system model is converted to electrical frequency by Equation 5.7.2:

$$\text{Electrical Speed (Hz)} = \frac{\text{Shaft Speed} * \text{Number of Poles}}{2} \qquad (5.7.2)$$

Therefore, the shaft speed obtained from the model is multiplied by 3 because the compressor electric motor is of 6 poles. The equations for the optimal compressor and condenser air flow rate for DX mode and Chiller mode are given by Equation 5.7.3-5.7.6. The coefficients of Equations 5.7.3-5.7.6 are given in

Table 5.6:

### 5.7.1 DX Mode

$$f_{comp_{electrical}} = C_1 + C_2 * Q_{load} + C_3 * Q_{load} * T_x + C_4 * Q_{load} * T_z + C_5 * Q_{load}^2 + C_6 * T_x^2 + C_7 * T_z^2 + C_8 * Q_{load}^2 * T_x + C_9 * Q_{load}^2 * T_z + C_{10} * Q_{load} * T_x^2 + C_{11} * Q_{load} * T_z^2 + C_{12} * T_x * T_z^2 + C_{13} * Q_{load} * T_x * T_z + C_{14} * Q_{load}^3 + C_{15} * T_z^3 \tag{5.7.3}$$

$$rpm_{cond} = C_1 + C_2 * T_x + C_3 * T_z + C_4 * Q_{load} * T_x + C_5 * T_x * T_z + C_6 * T_x^2 + C_7 * Q_{load}^2 * T_x + C_8 * Q_{load}^2 * T_z + C_9 * Q_{load} * T_x^2 + C_{10} * T_x^2 * T_z + C_{11} * Q_{load} * T_z^2 + C_{12} * T_x * T_z^2 + C_{13} * Q_{load} * T_x * T_z + C_{14} * Q_{load}^3 \tag{5.7.4}$$

### 5.7.2 Chiller Mode

$$f_{comp_{electrical}} = C_1 + C_2 * Q_{load} + C_3 * T_x + C_4 * Q_{load} * T_x + C_5 * Q_{load} * T_z + C_6 * T_x * T_z + C_7 * Q_{load}^2 + C_8 * T_z^2 + C_9 * Q_{load}^2 * T_x + C_{10} * Q_{load}^2 * T_z + C_{11} * Q_{load} * T_x^2 + C_{12} * T_x^2 * T_z + C_{13} * Q_{load} * T_z^2 + C_{14} * T_x * T_z^2 + C_{15} * Q_{load} * T_x * T_z + C_{16} * Q_{load}^3 + C_{17} * T_x^3 + C_{18} * T_z^3 \tag{5.7.5}$$

$$\mathrm{rpm_{cond}} = C_1 + C_2 * Q_{load} + C_3 * T_z + C_4 * Q_{load} * T_z + C_5 * T_z^2 + C_6 * Q_{load}^2 * T_z + C_7 * Q_{load} * T_x^2 + C_8 * T_x^2 * T_z + C_9 * T_x * T_z^2 + C_{10} * Q_{load} * T_x * T_z + C_{11} * Q_{load}^3 + C_{12} * T_x^3 + C_{13} * T_z^3 \quad (5.7.6)$$

Table 5.6: Coefficients for optimal compressor and condenser speed control equations

| | DX Mode | | Chiller Mode | |
|---|---|---|---|---|
| **Coefficients** | $\mathbf{f_{comp_{electrical}}}$ | $\mathbf{rpm_{cond}}$ | $\mathbf{f_{comp_{electrical}}}$ | $\mathbf{rpm_{cond}}$ |
| C1 | -3.833E+02 | -3.788E+05 | -4.996E+03 | 1.198E+06 |
| C2 | 2.711E+03 | 2.494E+03 | 2.823E+03 | -4.475E+03 |
| C3 | 3.004E+00 | 1.294E+03 | 4.683E+01 | -1.243E+04 |
| C4 | -2.084E+01 | 1.512E+00 | 1.852E+00 | 3.231E+01 |
| C5 | 9.723E+01 | -8.597E+00 | -2.032E+01 | 4.299E+01 |
| C6 | -5.147E-03 | -4.023E+00 | -3.313E-01 | -3.241E-01 |
| C7 | 1.878E-02 | 3.034E-01 | 3.227E+01 | 5.562E-02 |
| C8 | 1.759E-01 | -6.073E-01 | 1.867E-01 | -7.812E-03 |
| C9 | -5.064E-01 | 4.916E-02 | 6.844E-02 | 8.384E-03 |
| C10 | 1.708E-02 | 1.375E-02 | -1.748E-01 | -1.088E-01 |

| | | | | |
|---|---|---|---|---|
| C11 | 5.777E-02 | 5.166E-02 | 1.224E-02 | 1.238E+01 |
| C12 | 4.269E-05 | 2.551E-04 | -6.687E-04 | 2.429E-03 |
| C13 | -4.503E-02 | -1.011E-01 | 4.902E-02 | -5.256E-02 |
| C14 | 1.277E+00 | 1.215E+01 | 1.291E-03 | — |
| C15 | -7.405E-05 | — | -3.070E-02 | — |
| C16 | — | — | 8.150E-02 | — |
| C17 | — | — | 2.126E-04 | — |
| C18 | — | — | -6.889E-04 | — |
| RMSE | 1.0433 (Hz) | 11.1095 (rpm) | 0.3256 (Hz) | 11.71 (rpm) |

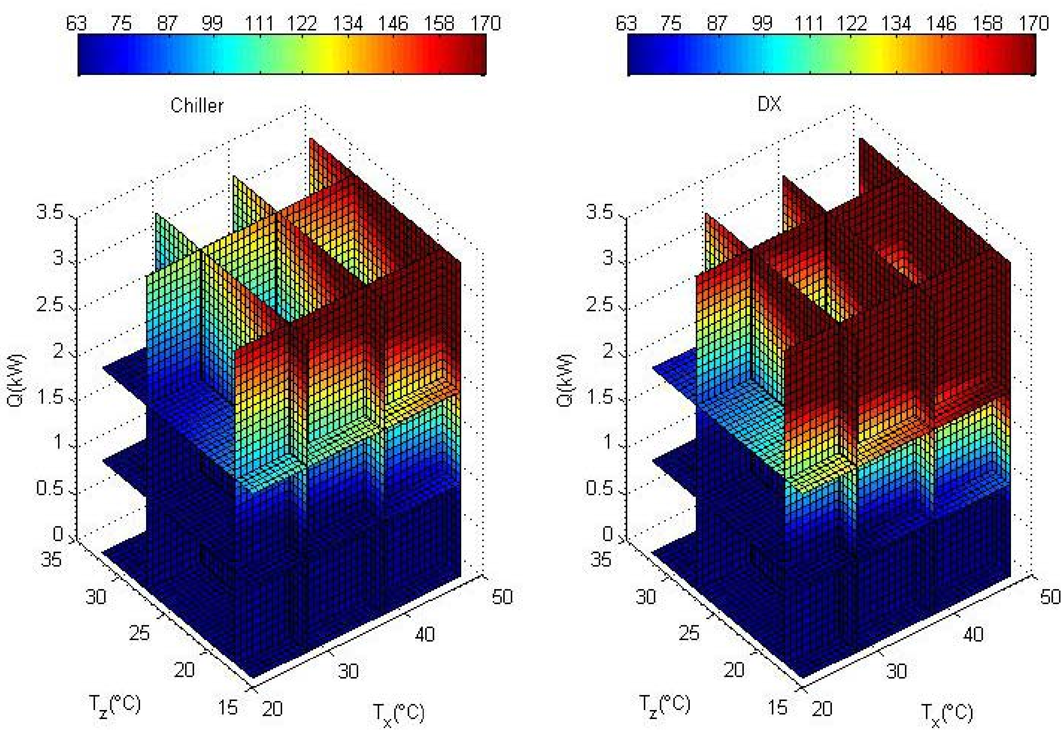


Figure 5.14: Illustration of optimal compressor speeds for DX and chiller mode operation for a given $Q_{load}$, $T_x$ and $T_z$

Figure 5.14 describes the optimal compressor speeds for a given set of $Q_{load}$, $T_x$ and $T_z$. The estimates from Equations 5.7.3-5.7.6 have been adjusted to account for the limitations of the MI test stand compressor speed and condenser fan speed limitations. It can be seen that in DX mode of operation, compressor runs at higher speeds to deliver the same amount of cooling load in relation with chiller mode operation. The operation at lower compressor speeds results in lower condenser fan speeds as can be observed in Figure 5.15. For a given set of $Q_{load}, T_x$ and $T_z$, around 17% reduction is estimated in compressor speed and around 13% reduction in condenser speed when operating in chiller mode. This reduction in compressor speed is mainly due to the water's high heat capacity as compared to air which results in energy savings during radiant cooling operation as pointed in (Feustel & Stetiu, 1995; Roth et al., 2002).

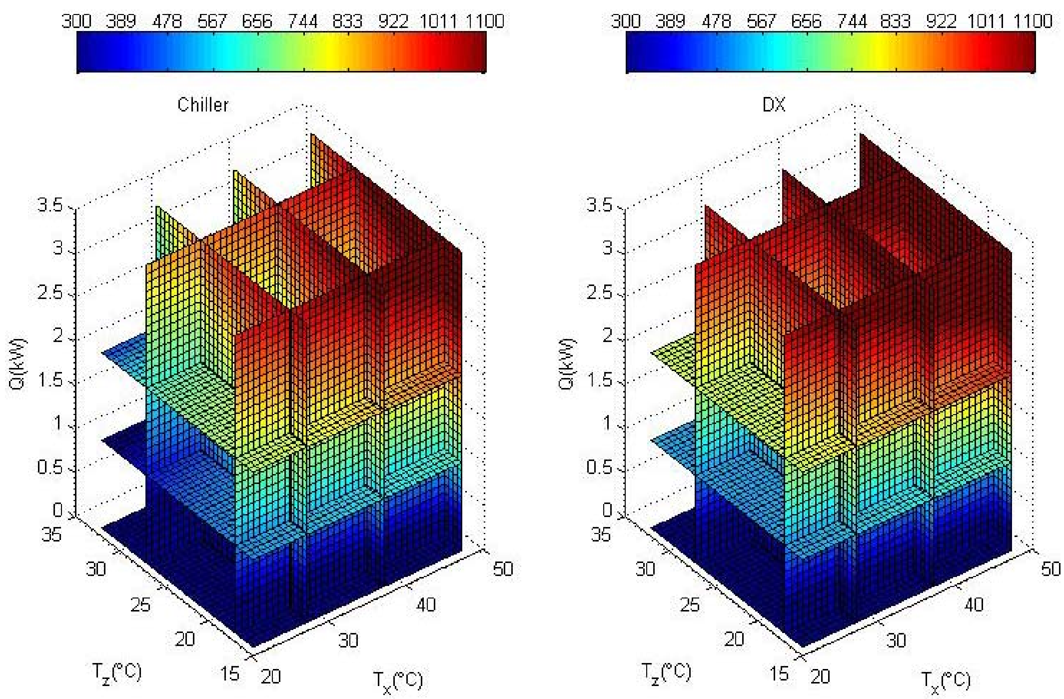


Figure 5.15: Illustration of optimal condenser fan speeds for DX and chiller mode operation for a given $Q_{load}, T_x$ and $T_z$

# CHAPTER 6

# Conclusion and Future Work

## 6.1 Conclusion

In this study models were developed for the components of a vapor compression cycle shown in Figure 3.1. A semi-empirical approach was taken for modeling of the compression process in a positive displacement compressor. The heat exchanger models were developed based on segment-by-segment approach. Flow pattern based correlation were used for modeling heat transfer and pressure drop in the two-phase region for fan-coil HX while generalized correlations were used for modeling single-phase heat transfer and pressure drop. In the case of brazed-plate HX, correlations developed for modeling heat transfer and pressure drop in chevron corrugated type brazed-plate HX using R-410a as the working fluid were used. The effect of circulating oil on component parameters was accounted for by using mixture models for calculation of thermo-physical and transport properties.

A test stand was built from a conventional air conditioning split unit to operate in either chiller mode or DX mode. A test chamber was also prepared for testing of radiant-cooling with pre-cooling control as part of the project. Sensors installed on the test stand were calibrated and instrumentation accuracy was checked by performing energy balance. Speed controls were implemented on the compressor and condenser fan to assess the savings in low-lift operation of the heat pump. Superheat control was implemented on the expansion valve to maintain any desired superheat down to 0.5K. Steady state test data was obtained for validation of the component models and a comparison with the component models presented in (Zakula, 2011, 2010) was performed. Equations for optimal compressor and condenser speeds were developed to be implemented in operation of test chamber in radiant-cooling operation with pre-cooling control.

In the compressor model, it was found that for high compressor speeds heat transfer between suction and discharge becomes important. In the condenser and brazed-plate evaporator, oil was found to increase the heat transfer due to promotion of annular flow. However, at low refrigerant flow rates, the heat transfer was found to decrease for fan-coil condenser. The tendency of oil was to increase pressure drop in HX. A comparison with the component models presented in (Zakula, 2011, 2010) showed that the current models predict the experimental data with higher accuracy in case of pressure drop while similar accuracy was estimated for heat transfer. It is to be noted that the HX models of (Zakula, 2011, 2010) doesn't take into account effect of oil on heat transfer and estimates a representative heat transfer coefficient and friction factor for the de-superheating, sub-cooling, condensation and evaporation regions. However, an inaccurate oil mass fraction significantly affects the calculation of heat transfer coefficient and friction factor in the current HX models at high vapor qualities where adverse oil effects are significant. This results in a higher prediction error as can be seen in the case of fan-coil evaporator. The data set that was used for fan-coil evaporator comprised of high compressor speeds at which high oil concentrations are likely to occur as mentioned in (Sarntichartsak et al., 2006). Use of incorrect oil properties also contribute to higher error estimation. In the case of brazed-plate evaporator, the current model was found to predict the experimental data with higher accuracy for both heat transfer and pressure drop. Therefore, use of two-phase correlations of (Hsieh & T. F. Lin, 2003) is recommended for modeling of two-phase heat transfer and pressure drop in brazed-plate HX. It was also found that solving for air volumetric flow rates for satisfying the HX energy balance in the system model results in high inaccuracies at low air volumetric flow rates despite small error in refrigerant mass flow rates. However, as the contribution of condenser fan power and evaporator fan or pump power in the system power is small, the effect on system performance prediction is minimal. The system COP is predicted to within ±20% for majority of the data points. In order to minimize errors in prediction of air volumetric flow rates solution of the properties for satisfying the HX energy balance that affects the estimation of refrigerant mass flow rate such as discharge and suction pressure is recommended which is the approach followed in (Zakula, 2010). From the optimal compressor and condenser fan speed equations, it was found that during chiller mode both compressor and condenser speeds are lower than DX mode speeds for delivering the same cooling load for a given outdoor and indoor temperature.

## 6.2 Future Work

The prediction accuracy of the compressor model over a wide range of pressure ratio and compressor speeds can be improved by using oil concentration as a function of compressor speed and incorporation of heat transfer between suction and discharge in the compressor model. Experimentation needs to be carried out to accurately estimate the oil concentration using any of the methods mentioned in (Fukuta, Yanagisawa, Miyamura, & Ogi, 2004; Lebreton, Vuillame, Morvan, & Lottin, 2001; Thome, 2004). Some of these methods are:

1. Measuring oil and refrigerant flow rates leaving an oil separator
2. Withdrawing liquid samples (ASHRAE Standard 41.4-1994)

3. Measuring refrigerant-oil mixture density through an accurate density measuring flow meter
4. Measuring speed of sound of refrigerant-oil liquid mixture through an ultrasonic sensor
5. Measuring refractive index of the refrigerant-oil mixture using a laser displacement sensor

Oil properties for POE/VG22 also should be obtained from manufacturer or experimentation to eliminate oil property errors. Formulation of refrigerant properties equations will greatly reduce time for solution and will enable the current system model to be used for optimization.

On the MI test stand, following things needs to be carried out:

– Compressor operation at higher speeds to better analyze the phenomenon involved at high pressure ratio operation and data repeatability.
– Implementation of speed control on evaporator
– Testing of pressure transducers on the dead weight tester for assessment of drift and repeatability

Implementation of radiant-cooling pre-cooling control in the test chamber using the speed equations presented in this study needs to be carried out to check the validity of the results and validation of savings estimated for hot and humid climates in (P. R. Armstrong, Jiang, Winiarski, Katipamula, & Norford, 2009).

# Appendix A

## Test Stand Components and Instrumentation Description

Table 7.1 and Table 7.2 describe the function of the components installed on the test stand and test chamber including control devices description and instrumentation details.

Table 7.1: Test stand and test chamber components description

| Name | Function | Specific Details |
|---|---|---|
| Mr. Slim compressor (KNB092FPAH) | Provide lift and refrigerant flow for cooling | 6 pole permanent magnet single rotary compressor<br>Rated motor power: 650W<br>Rotor Locked Amps (RLA): 7.8A<br>Winding resistance (@20°C): 0.49A |
| Outdoor fan coil unit MUZA09NA-1 | Air cooled condenser for rejection of heat to surroundings | Fin and tube HX with brushless DC fan motor |
| Brazed-Plate HX (GB240H-14) | Evaporator for chilled water circuit | Length:458mm<br>Width: 86mm<br>Number of plates: 14<br>Corrugation type: Chevron<br>Chevron angle: 65°<br>Corrugation amplitude: 2mm<br>Corrugation pitch: 6.8mm |
| Indoor fan coil unit MSA09NA | Evaporator for DX circuit | Fin and tube HX with DC fan motor |

| | | |
|---|---|---|
| Linear Expansion Valve (LEV) with capillary tube (20YGME-5R .4H12T) | Expansion of high pressure liquid refrigerant to provide cooling | Operated by a 12VDC stepper motor<br>Capillary tube: Outer diameter 3mm<br>Inner diameter 2mm<br>Length 240mm |
| Sight glass | Observation of refrigerant flow and quality | |
| Filter drier | Filtration of impurities such as water from refrigerant | |
| Expansion tank | Pressurization and pressure protection of chilled water circuit | Maximum pressure: 8psig<br>Burst pressure: 10psig |
| Water pump<br>(ALPHA2 L 25-40 130) | Circulation of water flow in PEX pipe embedded concrete slab | Supply voltage: 240VAC<br>Maximum head: 4m<br>Constant-pressure, proportional-pressure and constant-speed operation options |
| Fan | Thermal de-stratification | Supply voltage: 240VAC<br>355mm diameter fan with three speed settings |
| CR1000 | Data Logger and Programmable Logic Controller (PLC)<br>Used for data-logging and controlling compressor, outdoor fan and LEV | Analog measurement ports: 8(Differential), 16 (Single-Ended)<br>Pulse input ports: 2<br>Digital Input/Output ports: 8<br>Serial ports: 5<br>3 excitation ports of ±2.5V with 0.67mV resolution<br>Three 12V supply ports with maximum current limit of 900mA at 20°C<br>One Regulated 5V supply port with maximum current limit of 200mA<br>Scan rate range: 10msec-30sec |
| AM25T | Analog Voltage Measurement Peripheral for CR1000 | 25 Analog measurement ports<br>Built-in reference temperature sensor |

| | | |
|---|---|---|
| | Used for thermocouple measurement | |
| SDMAO4 | Analog voltage output peripheral for CR1000<br>Used for providing speed signal to outdoor fan | Voltage range: ±5V<br>Resolution: 2.5mV<br>Accuracy: 0.5% of Voltage+5mV |
| SDMIO16 | Digital Input/Output peripheral for CR1000<br>Used for frequency measurements and controlling LEV | Maximum frequency: 2kHz<br>Accuracy: ±0.01%<br>Output sink current: 8.6mA for 5V source<br>Maximum output current: power supply current limit |
| SDM16AC | AC/DC relay controller peripheral for CR1000<br>Used for control of test chamber thermal loads and water pump | Relay type: single pole double throw<br>Contact rating: 0.3A@ 110VDC, 5A @ 30VDC, 110VAC, 277VAC<br>Coil voltage: 9-18VDC |
| LEV Controller | Stepper motor controller | PIC14F4431 microcontroller for generating pulses for stepper motor<br>ULN2003 for switching voltage levels from 5V to 12V for stepper motor operation<br>Analog input |
| FR720S-80s VFD | Compressor speed controller | For general purpose magnetic flux control<br>Motor Constant R: 531Ω[1]<br>Rated voltage:70V<br>Rated frequency:120Hz<br>For linear V/f control V/f ratio: 1.3<br>Base frequency: 300Hz<br>Acceleration time: 3sec<br>Deceleration time:0.1sec<br>Max frequency: 300Hz<br>Starting frequency: 5Hz<br>Current limit: 8A<br>PWM carrier frequency: 15kHz |

| | | |
|---|---|---|
| | | Serial communication |
| BMC6A01 VFD | Outdoor fan speed controller | Maximum speed: 1750rpm<br>Acceleration time: 1.5sec<br>Deceleration time: 0.1sec<br>Current limit: 1.5A<br>PWM carrier frequency: 2kHz<br>Analog input |
| WT1600 | Electric power measurement device | Current range: 5mA-50A<br>Voltage range: 1.5V-1000V<br>Voltage Accuracy: 0.3% of reading + 0.1% of range<br>Current accuracy: (0.015*frequency in kHz+0.3)% of reading +0.2% of range<br>Power accuracy: (0.02*frequency in kHz+0.3)% of reading +0.2% of range<br>Analog output |

1. The values indicate the parameters value programmed into the VFD

Table 7.2: Test stand and test chamber sensors description

| Name | Function | Specific Details[1] |
|---|---|---|
| Honeywell MLH-500 | Gauge pressure transducer for refrigerant pressure measurement | Accuracy: ±5% full scale @>300psig<br>±10% full scale @100-299psig<br>Supply voltage: 5 ± 0.25VDC<br>Analog output: 0.5-4.5VDC |
| Measurement Specialties SSI-500 | Gauge pressure transducer for refrigerant pressure measurement | Accuracy: ±1% full scale<br>Supply voltage: 5VDC<br>Analog output: 0-100mVDC |
| Measurement Specialties US300 | Absolute pressure transducer for ambient pressure measurement | Accuracy: ±0.15% full scale<br>Supply voltage: 5VDC<br>Current output: 4-20mA |

| | | |
|---|---|---|
| Type T Thermocouple | Temperature measurement | Accuracy:±0.1°C<br>Analog output |
| Micromotion ELITE series | Refrigerant mass flow rate measurement | Supply voltage: 240VAC<br>Accuracy: ±0.05% of reading<br>Repeatability: ±0.025% of reading<br>Frequency output |
| Hansen Technologies SHP-06 | Brazed-Plate HX refrigerant level measurement | Linearity :±0.5% of reading<br>Supply voltage: 11-36VDC<br>Maximum pressure: 400psig<br>Analog output: 0-5VDC |
| GEMU 3030 magnetic water flow meter | Chilled water flow rate measurement | Supply voltage: 24VDC<br>Accuracy: ±1% full scale<br>Pulse output |
| Watt Node WNB-3Y-400-P | Electric power measurement | Accuracy: ±0.5% of reading<br>Pulse output |
| LICOR Pyranometer | Solar radiation measurement | Accuracy: ±5% of reading<br>Current output |
| Honeywell HIH4000 Humidity sensor | Test chamber humidity measurement | Accuracy: ±3.5%<br>Repeatability: ±0.5%<br>Hysteresis: 3%<br>Analog output |

1. Datasheet values are reported

# Appendix B

## Data Logging and Controlling Code for Test Stand Instruments

```
'CR1000 Series Datalogger
'Logging code for Abu Dhabi low lift chiller system
'program author: Muhammad Tauha Ali & Nicholas Gayeski
'date: May 2011

'Declare Reference Variables
Public CR1000Temp, AM25Temp, AM25Temp0, batt_volt, sdmstat, serialstat, es,
Public comp_voltage,comp_current, comp_current_limit=5.7,  failmode, suction_timer=0, timer_flag=0,suction_timer_set=60,
zone_timer=0, zone_flag=0,zone_timer_set=5, delay_timer=200, delay_flag=0, delay_timer_set=120'failsafe
Public Qe,Tz,f,rpm,TxK,TzK 'model based speed control
Public log_result, water_flow, pump_power, slab_temp(20), room_temp(19), Ptemp, Iload  '+++++
Public rpm_sensor
Public GHI_South, GHI_West, Tsouth, Twest
Public PambairkPa, RelativeHumidity, room_temp_NW, Tdew, Tglobe, SpecificHumidity, Tdew1

Public PdisPSIG, PcondoutPSIG, PevapinPSIG, PsucPSIG
Public RTdischarge, RTcondin, RTcondout, RTdrierin, RTdrierout 'high side temp
Public RTpostLEV, RTsuction, RTsuction1 'low side temp
Public RTHXin, RTHXout, CHWTin, CHWTout 'HX inlet and outlet
'Public RTcondout1,RTcondoutlevhigh1small,RTcondoutlevhigh2big,RTcondoutlevlow1small,RTcondoutlevlow2big 'tcondout
error check
Public ATcondenserin, ATdelTcondenser, delta_mV, Tref, dTresult, mV_TdT 'condenser thermopile

Public fan_totpower,fan_angle,fan_power,VFDpowerin,comp_totpower,comp_angle,comp_power
Public ref_mass_flow

Public Psat, Tsat 'for saturation temperature
Public Tsatcond, Tsubcool, Tsubcool_set=5 'subcool control
Public Tsatsuc,Tsuperheat,Tsuperheat_set=2,Tsatdis,Tsuperheatdis 'superheat control
Public refrigerant_level,refrigerant_level_set=95 'refrigerant level control

Public frequency_set_old As Long,frequency_set As Long,VFD_control_old As Long,VFD_control As Long, VFD_relay_old
'VFD control
Public fan_speed_set, fan_speed_max=1000,volt_signal(4) 'fan speed control
Public LEV_Kp,LEV_Ki,LEV_Kd,errvarLEV_old,errvarLEV=0,intgrlLEV=0,LEVcorr_0,LEVcorr,LEV_Kpold, LEV_Kiold,
LEV_Kdold,LEVpos=0,del As Long,LEV_operation(16) 'LEVcontrol
Public speed_Kp,speed_Ki,speed_Kd,errvarspeed_old,errvarspeed=0,intgrlspeed=0,speedcorr_0,speedcorr,speed_Kpold,
speed_Kiold, speed_Kdold 'speed control

Public cntrlvarLEV,cntrlvarLEV_set,cntrlvarLEV_set_old,cntrlvarspeed,cntrlvarspeed_set,cntrlvarspeed_set_old,Tz_set=24,
dead_band_speed=.5 'control variables

Alias RTdrierout=RTpreLEV
Alias ATcondenserin=Tx

Alias LEV_operation(1)=LEV_open
Alias LEV_operation(2)=LEV_close
```

```
Alias LEV_operation(3)=VFD_relay

Dim i=1

Const LEVmax_pos=965 'millisec
Const ct = 2 'number of times in a sec scan time/control time for LEV
Const ctspeed = 60 'number of times in a sec scan time/control time for speeds
Const dtt=20 'sec data table time
Const C0= -30.27 'from honeywell PT chart for R410a quadratic polynomial with ln(P)  Genetron-Pressure-Temperature-Chart in papers folder
Const C1= -14.71
Const C2= 4.61

'++++++++++++++++++++++++++++++++++++++++
'CR1000 TC's
'array number corresponds to SE channel #
Alias room_temp(1)=TC_1S
Alias room_temp(2)=TC_1M
Alias room_temp(3)=TC_1C
Alias room_temp(4)=TC_2S
Alias room_temp(5)=TC_2M
Alias room_temp(6)=TC_2C
Alias room_temp(7)=TC_3S
Alias room_temp(8)=TC_3M
Alias room_temp(9)=TC_3C
Alias room_temp(10)=TC_4S
Alias room_temp(11)=TC_4M
Alias room_temp(12)=TC_4C
Alias room_temp(13)=TC_E1
Alias room_temp(14)=TC_E2

'slab_temp TC locations
' 1,1   2   3   4
' 2,1   2   3   4
' 3,1   2   3   4
'height location
'-1 at 2.5, 0 at 5 (or 3cm above pipes), 1 at 7.5, 2 at 10, 3 at 12.5  measured from the bottom of slab (i.e. above insulation) (all are in cm)
'long dimension spacing= D1/4
'short dimension spacing= D2/3

'AM25T TC's
'array number corresponds to channel # for slab_temp
Alias slab_temp(1)=TC_110
Alias slab_temp(2)=TC_120 'not sure
'Alias slab_temp(3)=TC_130 not working
Alias slab_temp(3)=TC_140
Alias slab_temp(4)=TC_210
Alias slab_temp(5)=TC_220
Alias slab_temp(6)=TC_230
Alias slab_temp(7)=TC_240
Alias slab_temp(8)=TC_310 'not sure
Alias slab_temp(9)=TC_320
Alias slab_temp(10)=TC_330
Alias slab_temp(11)=TC_340
Alias slab_temp(12)=TC_221_
Alias slab_temp(13)=TC_221
Alias slab_temp(14)=TC_222
'channel 15 terminal screw faulty
Alias slab_temp(16)=TC_223
Alias slab_temp(17)=TC_231_
Alias slab_temp(18)=TC_231
```

```
Alias slab_temp(19)=TC_232
Alias slab_temp(20)=TC_233
Alias room_temp(15)=TC_W2 'channel 21
Alias room_temp(16)=TC_W1 'channel 22
Alias room_temp(17)=TC_SW 'channel 23
Alias room_temp(18)=TC_SE 'channel 24
Alias room_temp(19)=TC_NE 'channel 25

Alias water_flow=flow_rate_l_sec
Alias pump_power=power_W

'Define Data Tables
DataTable (room_temp,1,-1)
  DataInterval (0,2,Min,10)
  Average(1,TC_1S,IEEE4,false)
  Average(1,TC_1M,IEEE4,false)
  Average(1,TC_1C,IEEE4,false)
  Average(1,TC_2S,IEEE4,false)
  Average(1,TC_2M,IEEE4,false)
  Average(1,TC_2C,IEEE4,false)
  Average(1,TC_3S,IEEE4,false)
  Average(1,TC_3M,IEEE4,false)
  Average(1,TC_3C,IEEE4,false)
  Average(1,TC_4S,IEEE4,false)
  Average(1,TC_4M,IEEE4,false)
  Average(1,TC_4C,IEEE4,false)
  Average(1,TC_E1,IEEE4,false)
  Average(1,TC_E2,IEEE4,false)
  Average(1,TC_NE,IEEE4,false)
  Average(1,TC_W2,IEEE4,false)
  Average(1,TC_W1,IEEE4,false)
  Average(1,TC_SW,IEEE4,false)
  Average(1,TC_SE,IEEE4,false)
EndTable

DataTable (slab_temp,1,-1)
  DataInterval (0,2,Min,10)
  Average(1,PTemp,IEEE4,false)
  Average(1,TC_110,IEEE4,false)
  Average(1,TC_120,IEEE4,false) 'not sure
  'Average(1,TC_130,IEEE4,false)'not working
  Average(1,TC_140,IEEE4,false)
  Average(1,TC_210,IEEE4,false)
  Average(1,TC_220,IEEE4,false)
  Average(1,TC_230,IEEE4,false)
  Average(1,TC_240,IEEE4,false)
  Average(1,TC_310,IEEE4,false)'not sure
  Average(1,TC_320,IEEE4,false)
  Average(1,TC_330,IEEE4,false)
  Average(1,TC_340,IEEE4,false)
  Average(1,TC_221_,IEEE4,false)
  Average(1,TC_221,IEEE4,false)
  Average(1,TC_222,IEEE4,false)
  Average(1,TC_223,IEEE4,false)
  Average(1,TC_231_,IEEE4,false)
  Average(1,TC_231,IEEE4,false)
  Average(1,TC_232,IEEE4,false)
  Average(1,TC_233,IEEE4,false)
EndTable

DataTable (pump_performance,1,-1)
  DataInterval (0,2,Min,10)
```

```
  Average (1,flow_rate_l_sec,IEEE4,false)
  StdDev (1,flow_rate_l_sec,IEEE4,False)
  Average (1,power_W,IEEE4,false)
  StdDev (1,power_W,IEEE4,false)
EndTable
'++++++++++++++++++++++++++++++++++++
'Define Data Tables
DataTable (test_stand1,1,-1)
  DataInterval (0,2,Min,10)
  Minimum (1,batt_volt,IEEE4,0,False)
  'Average (1,CR1000Temp,IEEE4,)
  Average (1,AM25Temp,IEEE4,False)
  Average (1,fan_speed_set,IEEE4,False)
  Average (1,frequency_set_old,IEEE4,False)
  Average (1,PambairkPa,IEEE4,False)
  Average (1,RelativeHumidity,IEEE4,False)
  Average (1,Tz,IEEE4,False)
  Average (1,room_temp_NW,IEEE4,False)
  Average (1,Tdew,IEEE4,False)
  Average (1,SpecificHumidity,IEEE4,False)
  '  Average (1,Tglobe,IEEE4,False)
  Average (1,Tx,IEEE4,False)
  Average (1,ATdelTcondenser,IEEE4,False)
  Average (1,RTcondin,IEEE4,False)
  Average (1,RTpreLEV,IEEE4,False)
  Average (1,RTpostLEV,IEEE4,False)
  '  Average (1,VFDpowerin,IEEE4,False)
  Average (1,comp_power,IEEE4,False)
  Average (1,fan_Power,IEEE4,False)
  Average (1,GHI_South,IEEE4,False)
  Average (1,GHI_West,IEEE4,False)
  Average (1,Tsouth,IEEE4,False)
  Average (1,Twest,IEEE4,False)
  '  Average (1,refrigerant_level,FP2,False)
  Average (1,comp_voltage,IEEE4,False)
  Average (1,comp_angle,IEEE4,False)
EndTable

DataTable (test_stand0,1,-1)
  DataInterval (0,2,Min,10)

  Average (1,PdisPSIG,IEEE4,False)
  Average (1,PcondoutPSIG,IEEE4,False)
  Average (1,PevapinPSIG,IEEE4,False)
  Average (1,PsucPSIG,IEEE4,False)
  Average (1,RTdischarge,IEEE4,False)
  Average (1,RTcondout,IEEE4,False)
  Average (1,RTsuction,IEEE4,False)
  Average (1,RTHXin,IEEE4,False)
  Average (1,RTHXout,IEEE4,False)
    Average (1,CHWTin,IEEE4,False)
  Average (1,CHWTout,IEEE4,False)
  Average (1,Tsuperheat,IEEE4,False)
  Average (1,Tsuperheatdis,IEEE4,False)
  Average (1,Tsubcool,IEEE4,False)
  Average (1,comp_current,IEEE4,False)
  Average (1,ref_mass_flow,IEEE4,False)
  Average (1,rpm_sensor,IEEE4,False)
EndTable

Sub actLEV(cntrlvarLEV)
  Call LEVcontrol(cntrlvarLEV)
```

```
  If i<>0 'for zero excitation when valve is fully closed or open
  If LEVcorr>0'cntrlvar<cntrlvar_set 'open valve red light C2
  del=ABS(LEVcorr)

  'If del>LEVmax_pos*1000 Then 'for crash prevention (from NANs) not working
  'Else
  If del>3 '3msec is the delay of microcontroller
  'WriteIO(&B00100000,&B00100000) 'C6
  LEV_open=1
  SDMIO16(LEV_operation,sdmstat,0,94,0,0,0,0,1,0)
  Delay (1,del,mSec)'LEVcorr is the amount of time excitation remains there
  LEV_open=0
  SDMIO16(LEV_operation,sdmstat,0,94,0,0,0,0,1,0)
  'WriteIO(&B00100000,&B00000000)

  LEVpos=LEVpos+LEVcorr
EndIf
'EndIf
ElseIf LEVcorr<0'cntrlvar>cntrlvar_set 'close valve green light C3
  del=ABS(LEVcorr)
  'If del>LEVmax_pos*1000 Then
  'Else
  If del>3
  'WriteIO(&B01000000,&B01000000) 'C7
  LEV_close=1
  SDMIO16(LEV_operation,sdmstat,0,94,0,0,0,0,1,0)
  Delay (1,del,mSec)'LEVcorr is the amount of time excitation remains there
  LEV_close=0
  SDMIO16(LEV_operation,sdmstat,0,94,0,0,0,0,1,0)
  'WriteIO(&B01000000,&B00000000)

  LEVpos=LEVpos+LEVcorr
EndIf
'EndIf
EndIf
If LEVpos>LEVmax_pos
LEVpos=LEVmax_pos
ElseIf LEVpos<0
  LEVpos=0 'can't be less than 0
EndIf
EndIf
EndSub

Sub LEVcontrol(cntrlvarLEV)
  errvarLEV=cntrlvarLEV_set-cntrlvarLEV
  If (ABS(cntrlvarLEV_set-cntrlvarLEV_set_old)+ABS(LEV_Kp-LEV_Kpold)+ABS(LEV_Ki-LEV_Kiold)+ABS(LEV_Kd-
LEV_Kdold))>0 OR LEVpos>LEVmax_pos OR LEVpos<=0 Then
    intgrlLEV=0 'Resset Intergal term if the setpoint or gains are changed or valve is at saturation
  EndIf
  LEVcorr_0=LEV_Kp*errvarLEV+LEV_Kp*(intgrlLEV+1/ct*errvarLEV)/LEV_Ki+LEV_Kp*LEV_Kd*(errvarLEV-
errvarLEV_old)*ct 'control line
  LEVcorr=Round(LEVcorr_0,0)
  If (cntrlvarLEV_set<cntrlvarLEV AND LEVcorr>0) Then  'correct for incorrect valve operation and wrong correction (have
encountered)
    LEVcorr=-LEVcorr
  ElseIf (cntrlvarLEV_set>cntrlvarLEV AND LEVcorr<0) Then
    LEVcorr=LEVcorr
  EndIf
  'If (LEVcorr-LEV_pos) > LEVmax_del Then 'limit for positive extreme of pulses (correction that CR1000 can handle w/o
skipping scans) depends on scan time (not needed for 1 sec)
  ' LEVcorr=LEVmax_pos+LEV_pos
  'ElseIf (LEVcorr-LEV_pos) < -LEVmax_del Then 'limit for negative extreme of pulses
```

```
 ' LEVcorr =-LEVmax_pos+LEV_pos
 'EndIf
 'integral routine
 If LEVcorr>LEVmax_pos Then 'for max time limit/valve position
   LEVcorr=LEVmax_pos
   If errvarLEV > 0 Then
     intgrlLEV=intgrlLEV+errvarLEV*1/ct 's(k-1) integral summing
   EndIf
 ElseIf LEVcorr<-LEVmax_pos Then 'for max time limit/valve position
   LEVcorr =-LEVmax_pos
   If errvarLEV < 0 Then
     intgrlLEV=intgrlLEV+errvarLEV*1/ct 's(k-1) integral summing
   EndIf
 Else
   intgrlLEV=intgrlLEV+errvarLEV*1/ct 's(k-1) integral summing
 EndIf
 'LEVcorr_a=LEVcorr-LEV_pos
 'refrigrant_level_set_old=refrigerant_level_set

 errvarLEV_old=errvarLEV
 cntrlvarLEV_set_old=cntrlvarLEV_set
 LEV_Kpold=LEV_Kp
 LEV_Kiold=LEV_Ki
 LEV_Kdold=LEV_Kd
 If (LEVpos>=LEVmax_pos AND LEVcorr>0) Then ' not to operate valve if already fully open or closed
   LEVcorr=0
   intgrlLEV=0
   i=0
 ElseIf (LEVpos<=0 AND LEVcorr<0) Then
   LEVcorr=0
   intgrlLEV=0
   i=0
 EndIf
EndSub

Sub Failsafe
 If CHWTin<5 OR CHWTout<5 OR Tz<10 OR RTdischarge>85 OR Tsatdis>60 OR comp_current>=7 OR comp_current=Nan
 frequency_set=0
 VFD_control=0
 ModBusMaster(serialstat,Com3,19200,1,16,VFD_control,9,1,3,10) 'change VFD operation status start (2)/stop(0 or 1)
 ModBusMaster(serialstat,Com3,19200,1,16,frequency_set,14,1,3,10) 'change running VFD frequency
 ModBusMaster(serialstat,Com3,19200,1,3,frequency_set_old,14,1,3,10) 'read running VFD frequency
 failmode=1
 delay_timer=Timer(3,Sec,2) 'reset and start delay_timer
 delay_flag=1
EndIf
If RTsuction1<-2 AND timer_flag=0
suction_timer=Timer(1,Sec,2) 'reset and start suction_timer
timer_flag=1
EndIf
suction_timer=Timer(1,Sec,4)
If RTsuction1<-2 AND suction_timer>suction_timer_set 'if Tsuction remains at -2 for 1 minute
frequency_set=0
VFD_control=0
ModBusMaster(serialstat,Com3,19200,1,16,VFD_control,9,1,3,10) 'change VFD operation status start (2)/stop(0 or 1)
ModBusMaster(serialstat,Com3,19200,1,16,frequency_set,14,1,3,10) 'change running VFD frequency
ModBusMaster(serialstat,Com3,19200,1,3,frequency_set_old,14,1,3,10) 'read running VFD frequency
failmode=2
delay_timer=Timer(3,Sec,2) 'reset and start delay_timer
suction_timer=Timer(1,Sec,3) 'stop and reset suction_timer
timer_flag=0
ElseIf suction_timer>suction_timer_set
```

```
  suction_timer=Timer(1,Sec,3) 'reset and stop suction_timer
  timer_flag=0
EndIf
EndSub

'Main Program
BeginProg
  'for LEV control with Tsuperheat
  LEV_Kp=5
  LEV_Kpold=LEV_Kp
  LEV_Ki= 45
  LEV_Kiold=LEV_Ki
  LEV_Kd= 11.25
  LEV_Kdold=LEV_Kd

  'for speed control with Tz
  speed_Kp=5000
  speed_Kpold=speed_Kp
  speed_Ki= 100000
  speed_Kiold=speed_Ki
  speed_Kd= 0
  speed_Kdold=speed_Kd

  'initialization
  frequency_set=10000
  frequency_set_old=frequency_set

  fan_speed_set=1000

  VFD_control=0
  VFD_control_old=VFD_control

  VFD_relay=0
  VFD_relay_old=VFD_relay

  cntrlvarLEV_set_old=cntrlvarLEV_set
  cntrlvarspeed_set_old=cntrlvarspeed_set
  f=63
  rpm=0

  SDMIO16(LEV_operation,sdmstat,0,89,0,0,0,0,0111,0) 'don't know why it doesn't work sometimes with 94 if restart cr1000

  'initialization for controls
  ModBusMaster(serialstat,Com3,19200,1,16,VFD_control,2,1,3,10) 'for resetting VFD .1msec delay
  'SW12(1) '12V power for control circuit
  'WriteIO(&B10000000,&B00000000) 'relay on (currently off)
  'WriteIO(&B00100000,&B00100000) 'to bring the valve to its fully close position green light C4
  LEV_close=1
  SDMIO16(LEV_operation,sdmstat,0,94,0,0,0,0,1,0)
  Delay (1,3,Sec)'LEVcorr is the amount of time excitation remains there
  LEV_close=0
  SDMIO16(LEV_operation,sdmstat,0,94,0,0,0,0,1,0)
  'WriteIO(&B00100000,&B00000000)
  'SDMIO16(LEV_close,sdmstat,0,89,9999,9999,9999,9990,1,0)
  ModBusMaster(serialstat,Com3,19200,1,3,VFD_control_old,9,1,3,10) 'read VFD operation status
  ModBusMaster(serialstat,Com3,19200,1,16,frequency_set,14,1,3,10) 'set VFD frequency = 0Hz

  volt_signal(1)=0 '1rpm=2.857mV
  SDMAO4(volt_signal(1),1,1)

  Scan (ct,Sec,0,0)
    AM25T (AM25Temp0,0,mV2_5,1,1,TypeT,AM25Temp0,4,8,Vx1,True ,0,_50Hz,1.0,0)
```

```
   ' Refrigerant pressures
   VoltDiff (PdisPSIG,1,mV250C,5,True ,0,_50Hz,4.977,1.55) 'calibrated transducer number 3
   VoltSe (PcondoutPSIG,1,mv5000,13,True,0,_50Hz,123.9e-3,-63.1) 'calibrated transducer number 5
   VoltSe (PevapinPSIG,1,mv5000,14,True,0,_50Hz,124.7e-3,-63.83) 'calibrated transducer number 8
   VoltDiff (PsucPSIG,1,mV250C,6,True ,0,_50Hz,4.945,-6.467) 'calibrated transducer number 1

   ' Refrigerant temperatures
   'high side temperatures
   AM25T (RTdischarge,1,mV2_5,1,1,TypeT,AM25Temp0,4,8,Vx1,True ,0,_50Hz,1.0,0) ' soldered
   AM25T (RTcondout,1,mV2_5,3,1,TypeT,AM25Temp0,4,8,Vx1,True ,0,_50Hz,1.0,0) ' soldered
   AM25T (RTsuction,1,mV2_5,8,1,TypeT,AM25Temp0,4,8,Vx1,True ,0,_50Hz,1.0,0) ' soldered

   AM25T (RTHXin,1,mV2_5,7,1,TypeT,AM25Temp0,4,8,Vx1,True ,0,_50Hz,1.0,0) ' soldered
   AM25T (RTHXout,1,mV2_5,12,1,TypeT,AM25Temp0,4,8,Vx1,True ,0,_50Hz,1.0,0) ' soldered

   'chilled water temperatures
   AM25T (CHWTin,1,mV2_5,9,1,TypeT,AM25Temp0,4,8,Vx1,True ,0,_50Hz,1.0,0) ' soldered
   AM25T (CHWTout,1,mV2_5,10,1,TypeT,AM25Temp0,4,8,Vx1,True ,0,_50Hz,1.0,0) ' soldered

   'to calculate superheat
   Tsatsuc=C2*(LN(PsucPSIG+14.5))^2+C1*(LN(PsucPSIG+14.5))+C0
   Tsuperheat=RTsuction-Tsatsuc

   Tsatdis=C2*(LN(PdisPSIG+14.5))^2+C1*(LN(PdisPSIG+14.5))+C0
   Tsuperheatdis=RTdischarge-Tsatdis

   'to calculate subcooling
   Tsatcond=C2*(LN(PcondoutPSIG+14.7))^2+C1*(LN(PcondoutPSIG+14.7))+C0
   Tsubcool=Tsatcond-RTcondout

   i=1
   cntrlvarLEV=-Tsuperheat 'can make any variable control varaiable as long as error (set-actual) follows for > valve open for <
valve close
   'parameter       s>a      s<a       actual increase   actual decrease
   'ref. level       open     close      open            close
   'Tsubcool         open     close      open            close
   'Tsuperheat       close    open       close           open     (if multiply by -1 both set and actual then s>a open s<a close)
   'Tsuperheatcond   close    open       close           open     (if multiply by -1 both set and actual then s>a open s<a close)
   'Q               decrease  increase   speed decrease     speed increase
   cntrlvarLEV_set=-Tsuperheat_set

   Call actLEV(cntrlvarLEV)

   ' mass flow rate
   PulseCount (ref_mass_flow,1,2,0,1,3e-6,0) 'Refrigerant
   '10000Hz=.03 kg/sec so for 1 Hz 3e-6

   ' rpm sensor
   PulseCount(rpm_sensor,1,1,2,1,60,0)

   'to prevent compressor stall and decrease compressor current
   AM25T(comp_current,1,mv5000,18,1,-1,AM25Temp0,4,8,Vx1,False,0,_50Hz,.002,0)
   Call Failsafe

   CallTable test_stand0

   PulseCountReset
  NextScan

  SlowSequence
  Scan(dtt,Sec,0,0)
```

```
    If VFD_relay<>VFD_relay_old
    SDMIO16(LEV_operation,sdmstat,0,94,0,0,0,0,1,0)
    VFD_relay_old=VFD_relay
  EndIf

  If frequency_set<>frequency_set_old
  ModBusMaster(serialstat,Com3,19200,1,16,frequency_set,14,1,3,10) 'change running VFD frequency
  ModBusMaster(serialstat,Com3,19200,1,3,frequency_set_old,14,1,3,10) 'read running VFD frequency
EndIf

volt_signal(1)=fan_speed_set*(2.857+.0857)+1.9 '1rpm=2.857mV
SDMAO4(volt_signal(1),1,1)

If VFD_control<>VFD_control_old
ModBusMaster(serialstat,Com3,19200,1,16,VFD_control,9,1,3,10) 'change VFD operation status start (2)/stop(0 or 1)
VFD_control_old=VFD_control
EndIf

'Panel Temperatures and references
AM25T (AM25Temp,0,mV2_5,1,1,TypeT,AM25Temp,4,8,Vx1,True ,0,_50Hz,1.0,0)
'PanelTemp (CR1000Temp,_50Hz)
Battery (Batt_volt)

' Air pressure
VoltDiff (PambairkPa,1,mv5000,8,True,0,_50Hz,3.939e-3,-3.75)
'238 ohm, 4-20 mA output, 4760 mV = 15 psia, 952 mV = 0 psia
PambairkPa=PambairkPa*6.89476

'zone relative humidity
VoltSe (RelativeHumidity, 1,mv5000,3,True,0,_50Hz,0.032258,-25.80645)

'zone temperature
AM25T (room_temp_NW,1,mV2_5,13,1,TypeT,AM25Temp,4,8,Vx1,True ,0,_50Hz,1.0,0)
'    AM25T (Tglobe,1,mV2_5,14,1,TypeT,AM25Temp,4,6,Vx1,True ,0,_50Hz,1.0,0)
es=6.1121*EXP((18.678-room_temp_NW/234.5)*room_temp_NW/(257.14+room_temp_NW)) 'arden buck equation 1996
'Tdew1=(237.7*LOG10(es*RelativeHumidity/611))/(7.5-LOG10(es*RelativeHumidity/611))
SpecificHumidity=.62197*(es*RelativeHumidity/100)/(PambairkPa*10+(es*RelativeHumidity/100)*(.62197-1))
DewPoint(Tdew,room_temp_NW,RelativeHumidity)
If Tdew>room_temp_NW OR Tdew=NAN Then Tdew=room_temp_NW

' Air Temperature
AM25T (ATcondenserin,1,mV2_5,11,1,TypeT,AM25Temp,4,8,Vx1,True ,0,_50Hz,1.0,0)

' Scaling for thermopile measurement
AM25T (delta_mV,1,mV25C,16,1,-1,AM25Temp,4,8,Vx1,True ,0,_50Hz,1.0,0)
delta_mV = delta_mV/16 '16 thermopile junction pairs
Tref = ATcondenserin
'delta_mV = delta_mV*0.1 'to avoid exponents in equation of volt to temp conversion dTresult
'TdTref = TdTref*0.01
'mV_TdT = delta_mV*TdTref*0.001' for bringing it in Volts
dTresult = 25.89-5.749e-2*Tref-.7447*delta_mV+1.632e-4*Tref^2+5.557e-3*Tref*delta_mV+.4654*delta_mV^2-.4475e-
6*Tref^3-2.107e-5*Tref^2*delta_mV-3.793e-4*Tref*delta_mV^2-2.188e-3*delta_mV^3 'volt to temp conversion
'dTresult = dTresult-5.749*TdTref+1.635*TdTref-0.4475*TdTref
'dTresult = dTresult+mV_TdT*5.557-2.107*mV_TdT*TdTref-3.793*mV_TdT*delta_mV
'delta_mV = delta_mV*10
ATdelTcondenser = dTresult*delta_mV
'TdTref = TdTref*100

' end of scaling for thermopile measurement

' Wattnode power
```

```
'PulseCount (VFDpowerin,1,1,0,1,34.506,0)
' WNB-3Y-400-P, Wh per pulse per CT rated Amp = 0.001917
' 59.7 ohm resistor installed = 5 Amps full scale
' WhpP = 0.0096
' Watts = WhpP*PulseCount/sec*3600 sec/hour
' W/Hz = WhpP*3600 sec/hour = 34.506 Watts

AM25T (RTcondin,1,mV2_5,2,1,TypeT,AM25Temp,4,8,Vx1,True ,0,_50Hz,1.0,0) ' soldered

'low side temperatures
AM25T (RTpostLEV,1,mV2_5,6,1,TypeT,AM25Temp,4,8,Vx1,True ,0,_50Hz,1.0,0) ' soldered

'to see drier temperature drop which implies pressure drop
'AM25T (RTdrierin,1,mV2_5,4,1,TypeT,AM25Temp,4,8,Vx1,True ,0,_50Hz,1.0,0) ' soldered
AM25T (RTdrierout,1,mV2_5,5,1,TypeT,AM25Temp,4,8,Vx1,True ,0,_50Hz,1.0,0) ' soldered

VoltSe(GHI_South,1,mV25,4,True,0,_50Hz,-86.704,0)  'PY64287 1/(78.7e-3*146.55ohm)
VoltSe(GHI_West,1,mV25,5,True,0,_50Hz,-85.03,0)   'PY64288 1/(78.93e-3*149ohm)
AM25T (Tsouth,1,mV2_5,25,1,TypeT,AM25Temp,4,8,Vx1,True ,0,_50Hz,1.0,0) 'epoxied
AM25T (Twest,1,mV2_5,24,1,TypeT,AM25Temp,4,8,Vx1,True ,0,_50Hz,1.0,0) ' epoxied

' Measure refrigerant level
VoltSe (refrigerant_level,1,mv5000,6,True,0,_50Hz,16.67e-3,16.67)
'3321.15mV=100 level 1mV=.03006153596 level (not applicable)

GetVariables(log_result,ComRS232,0,2,0,0,"Public","room_temp()",room_temp(),19)
Tz=(room_temp(1)+room_temp(2)+room_temp(3)+room_temp(4)+room_temp(5)+room_temp(6)+room_temp(7)+room_temp(8
)+room_temp(9)+room_temp(10)+room_temp(11)+room_temp(12)+room_temp(13)+room_temp(14)+room_temp(15)+room_te
mp(16)+room_temp(17)+room_temp(18)+room_temp(19)+room_temp_NW)/20
''cntrlvarspeed=-Tz
''cntrlvarspeed_set=-Tz_set

AM25T(comp_voltage,1,mv5000,17,1,-1,AM25Temp,4,8,Vx1,False,0,_50Hz,.06,0)
AM25T(comp_angle,1,mv5000,19,1,-1,AM25Temp,4,8,Vx1,False,0,_50Hz,.072,0)
AM25T(comp_power,1,mv5000,20,1,-1,AM25Temp,4,8,Vx1,False,0,_50Hz,1.22,0)
AM25T(fan_power,1,mv5000,22,1,-1,AM25Temp,4,8,Vx1,False,0,_50Hz,.06,0)
CallTable test_stand1

NextScan
EndSequence

SlowSequence
Scan(2,Min,0,0)
  PakBusClock(2)
  GetDataRecord(log_result,ComRS232,0,2,0,0,2,&H8001,room_temp)
  GetDataRecord(log_result,ComRS232,0,2,0,0,2,&H8002,slab_temp)
  GetDataRecord(log_result,ComRS232,0,2,0,0,2,&H8003,pump_performance)
  GetRecord(room_temp(),room_temp,1)
  GetVariables(log_result,ComRS232,0,2,0,0,"Public","Iload",Iload,1)
NextScan
EndSequence
EndProg
```

# Appendix C

## Test Chamber Heat Transfer Reduction after Insulation

**Data:**

Wall is made up of two steel sheets with fiberglass insulation in between

Thickness of wall (t) = 6cm

Insulation thickness = 10cm

k for fiberglass = 0.04W/mK ("Thermal Conductivity of some common Materials," 2011)

k for polystyrene = 0.0343 W/mK [manufacturer datasheet]

**Assumptions**:

– Thermal Resistance of steel sheets is negligible.

– Convection and radiation heat transfer is neglected.

– Assume a temperature difference of 10K between the internal walls.

**Solution**:

$$\frac{Q}{A} = k * \frac{\Delta T}{t}$$

Before insulation: Q = 6.67 $W/m^2$

After insulation: Q = 2.26 $W/m^2$

Percentage reduction: <u>66%</u>

# Appendix D

# Air Leakage Testing of Test Chamber

## 10.1 Air Leakage before Caulking:

**BUILDING LEAKAGE TEST**

Date of Test:
Test File: with ac off 1

Technician: Tauha

Customer:

Building Address: Block 6
Masdar City
Abu Dhabi, Abu Dhabi 54224

| | |
|---|---|
| **Test Results at 50 Pascals:** | |
| Airflow (m³/h) | 164 ( +/- 0.1 %) |
| Air Changes per Hour (1/h) | 2.04 |
| m³/(h*m² Floor Area) | 3.89 |
| m³/(h*m² Surface Area) | 1.23 |
| **Leakage Areas:** | 64.6 cm² ( +/- 0.4 %) Canadian EqLA @ 10 Pa or 0.49 cm²/m² Surface Area<br>34.5 cm² ( +/- 0.6 %) LBL ELA @ 4 Pa or 0.26 cm²/m² Surface Area |
| **Building Leakage Curve:** | Flow Coefficient (C) = 13.1 ( +/- 1.0 %)<br>Exponent (n) = 0.645 ( +/- 0.003 )<br>Correlation Coefficient = 0.99988 |
| Test Standard: | CGSB Test Mode: Pressurization |
| Equipment: | Model 4 (230V) Minneapolis Blower Door |

| | | | |
|---|---|---|---|
| Inside Temperature: | 24 °C | Volume: | 80 m³ |
| Outside Temperature: | 24 °C | Surface Area: | 133 m² |
| | | Floor Area: | 42 m² |

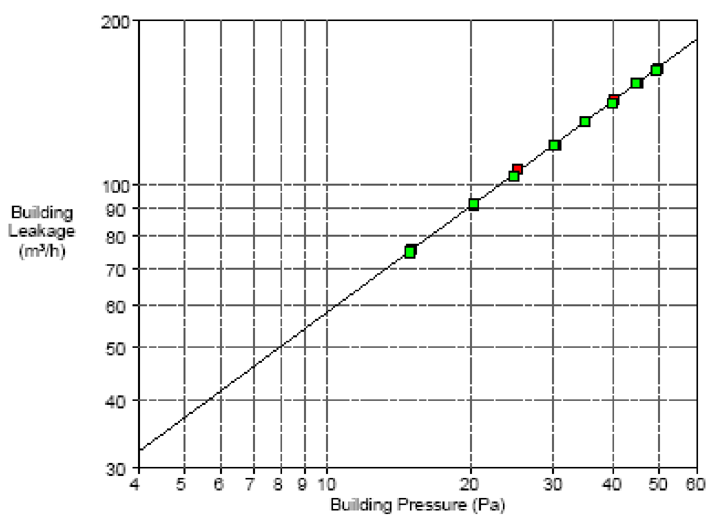

## 10.2 Air Leakage after Caulking:

BUILDING LEAKAGE TEST

| | | | |
|---|---|---|---|
| Date of Test: | | Technician: | Tauha |
| Test File: seal4 | | | |
| Customer: | | Building Address: | Block 6<br>Masdar City<br>Abu Dhabi, Abu Dhabi 54224 |

**Test Results at 50 Pascals:**

| | |
|---|---|
| Airflow ($m^3/h$) | 103 ( +/- 0.1 %) |
| Air Changes per Hour (1/h) | 1.29 |
| $m^3/(h*m^2$ Floor Area) | 2.46 |
| $m^3/(h*m^2$ Surface Area) | 0.77 |

**Leakage Areas:** 40.9 $cm^2$ ( +/- 0.2 %) Canadian EqLA @ 10 Pa or 0.31 $cm^2/m^2$ Surface Area
21.8 $cm^2$ ( +/- 0.3 %) LBL ELA @ 4 Pa or 0.16 $cm^2/m^2$ Surface Area

**Building Leakage Curve:** Flow Coefficient (C) = 8.3 ( +/- 0.5 %)
Exponent (n) = 0.644 ( +/- 0.001 )
Correlation Coefficient = 0.99999

Test Standard: CGSB Test Mode: Depressurization
Equipment: Model 4 (230V) Minneapolis Blower Door

| | | | |
|---|---|---|---|
| Inside Temperature: | 24 °C | Volume: | 80 $m^3$ |
| Outside Temperature: | 24 °C | Surface Area: | 133 $m^2$ |
| | | Floor Area: | 42 $m^2$ |

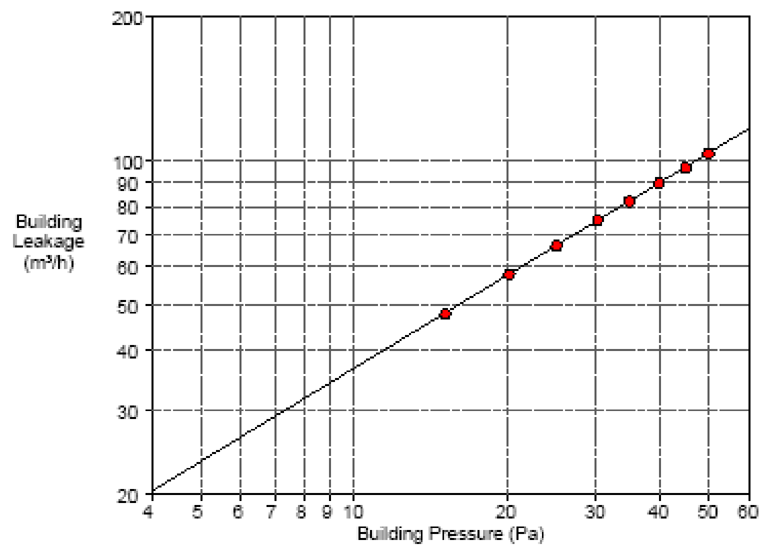

# Appendix E

## Test Chamber Components and Thermocouple Location Description

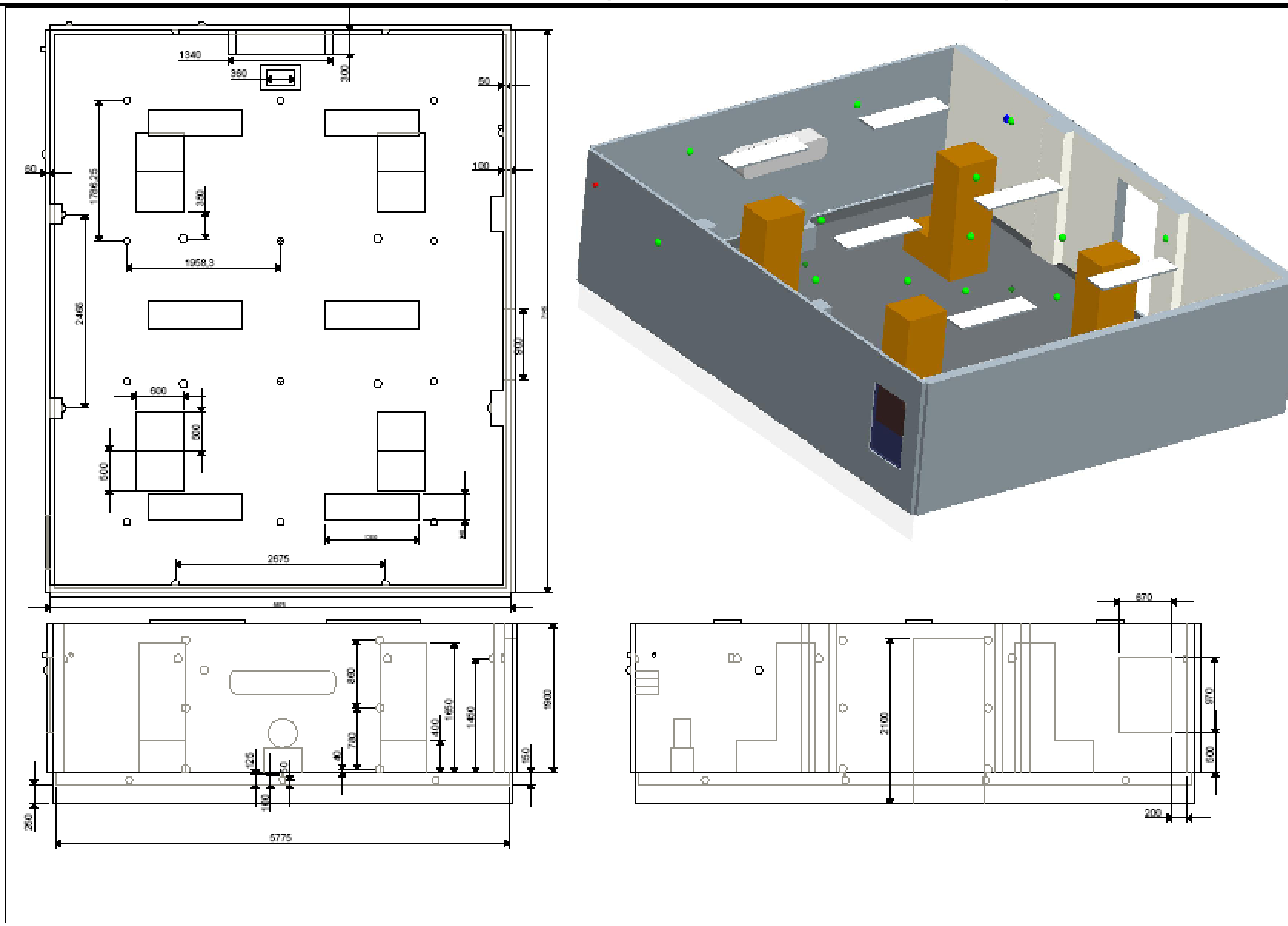

# Appendix F

## Gauge Pressure Sensor/ Transducer Calibration Procedure

1. Close the valve on the nitrogen cylinder pressure regulator.
2. Open the vent valve labeled “<- –“ on the Mensor CPB5000.
3. Remove the plug from the pressure sensor/transducer mounting place on the right side of CPB5000.
4. Attach the pressure sensor/transducer directly on the mounting or on the ¼” header with three ports available.
5. Close the vent valve and open the valve labeled “<- +” on CPB5000.
6. Open the valve on the pressure regulator to a suitable pressure value.[3]*
7. Check the connection for leaks using soap bubble.
8. Clean the soap from the connections after leak testing.
9. Close the valve labeled “<- +” and open the vent valve.
10. Remove the plug from piston mounting place by rotating the ConTect quick connector anti-clockwise on the left side of the CPB5000.[4]
11. Place the piston on the mounting and close the ConTect quick connector by rotating in clockwise direction.
12. Note the ambient temperature and pressure to 0.01% Full Scale (FS) of test article.

---

[3] **Do not exceed the maximum limit of the pressure sensor/transducer or CPB5000 which is 100bar/1500psi**

[4] Use Latex gloves while handling the piston or weights to protect them from dust or scratches. Use Alcohol and a soft cloth for cleaning of the weights

13. Use a voltage source stable to four significant digits or CR1000 (for +5V) for excitation of pressure transducers.
14. Place the weights on the piston to exert the desired pressure on the pressure sensor/transducer.
15. Open the valve labeled “<- +” and observe the pressure reading on the pressure gauge on CPB5000.
16. Use the three spoke handle for small increments or decrements in pressure and try to achieve a stable floating position for the piston.
17. Observe the marking line on the mirror near the piston mounting place as shown in the figure.

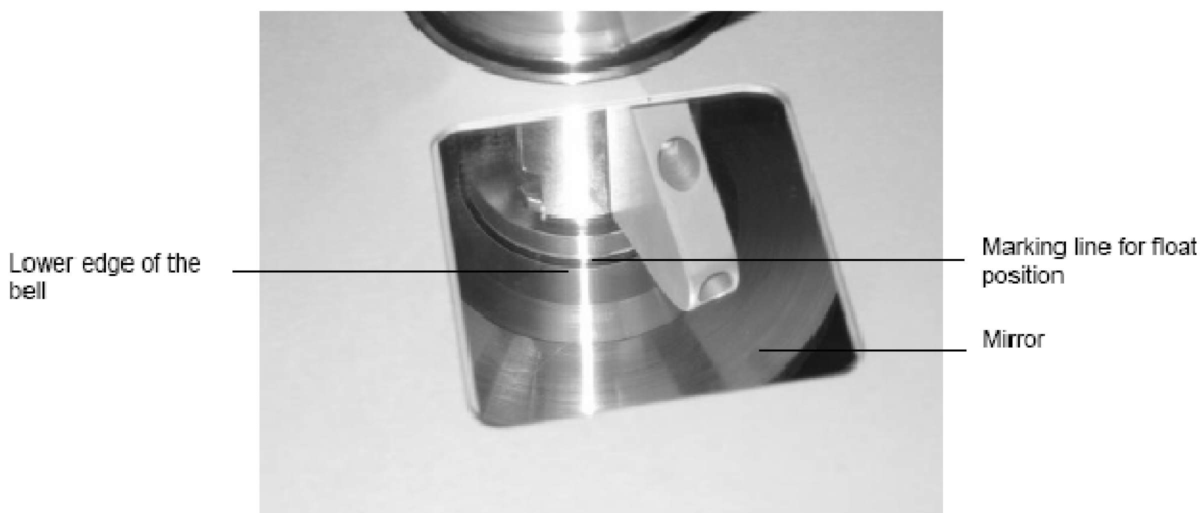


**Just before the float position, the system increases quickly.**
**We therefore recommend turning the spindle slowly and evenly clockwise.**

18. To minimize the effect of friction, move the system up against the weight pieces carefully and make a turning movement.[5]
19. Wait 10-15 seconds to see if the system maintains its position.
20. Observe the reading in the pressure sensor/transducer.
21. Use CR1000 (if possible) for reading voltage from the pressure transducer.
22. Take 6 readings at approximately 0%, 20%, 40%, 60%, 80% and 100% of full scale in increasing and decreasing manner each.
23. Plot the regression line to get the multiplier and offset for the pressure sensor/transducer. Report standard errors and t-statistics.
24. After finishing calibration, close the valve on the pressure regulator and release the pressure by opening the vent valve on CPB5000.
25. Remove the piston and pressure transducers from CPB5000 and put back the plugs.
26. Cover CPB5000 to protect it from dust.

[5] **Never move the system up and make a turning movement, if the piston is in the lower or upper block position.**

# Appendix G

## Test Stand Data for DX Mode of Operation

| | | | Refrigerant Temperatures | | | | Refrigerant Pressures | | | | |
|---|---|---|---|---|---|---|---|---|---|---|---|
| Comp-ressor Speed (Hz) | Zone Air Temp (°C) | Outdoor Air Temp (°C) | Discharge Temp (°C) | Condenser Inlet Temp (°C) | Condenser Outlet Temp (°C) | Suction Temp (°C) | Ambient Pressure (kPa) | Suction Pressure (psig) | Post-EXV Pressure (psig) | Condenser Outlet Pressure (psig) | Discharge Pressure (psig) |
| 21.67 | 31.94 | 35.71 | 50.81 | 49.18 | 38.88 | 26.66 | 99.56 | 221.59 | 241.89 | 327.35 | 335.72 |
| 21.67 | 31.94 | 36.74 | 51.41 | 50.02 | 40.02 | 27.25 | 99.69 | 227.97 | 249.02 | 336.67 | 345.50 |
| 21.67 | 32.00 | 37.64 | 51.88 | 50.64 | 40.86 | 27.63 | 99.54 | 232.54 | 253.88 | 343.59 | 352.85 |
| 26.67 | 31.76 | 36.24 | 55.18 | 53.49 | 41.36 | 26.10 | 99.47 | 216.49 | 242.96 | 348.08 | 358.03 |
| 26.67 | 31.73 | 35.41 | 54.60 | 52.87 | 41.13 | 26.02 | 99.50 | 216.65 | 242.87 | 346.50 | 355.95 |
| 26.67 | 31.70 | 34.70 | 54.20 | 52.47 | 40.84 | 25.88 | 99.44 | 215.85 | 241.93 | 344.14 | 353.56 |
| 26.67 | 31.97 | 35.25 | 55.72 | 54.03 | 42.90 | 26.99 | 99.51 | 225.83 | 253.17 | 361.97 | 372.77 |
| 33.33 | 31.29 | 35.68 | 57.09 | 55.51 | 42.59 | 23.23 | 99.59 | 205.19 | 238.64 | 359.38 | 371.00 |
| 33.33 | 31.30 | 36.27 | 57.99 | 56.56 | 43.90 | 22.77 | 99.61 | 209.00 | 244.83 | 370.97 | 382.80 |
| 33.33 | 32.08 | 34.30 | 57.54 | 55.90 | 43.17 | 23.49 | 99.35 | 208.49 | 243.09 | 364.75 | 376.42 |
| 40.00 | 31.44 | 34.79 | 62.29 | 60.45 | 44.99 | 21.71 | 99.42 | 195.08 | 238.54 | 381.51 | 395.76 |
| 40.00 | 31.31 | 33.82 | 62.95 | 60.99 | 44.30 | 22.54 | 99.21 | 191.32 | 233.86 | 375.34 | 388.71 |
| 40.00 | 31.16 | 33.08 | 62.14 | 60.28 | 44.28 | 21.65 | 99.21 | 191.90 | 234.84 | 375.38 | 388.59 |
| 40.00 | 27.27 | 30.39 | 55.73 | 53.75 | 40.09 | 16.30 | 99.67 | 171.97 | 211.46 | 337.27 | 349.62 |
| 40.00 | 27.15 | 30.33 | 55.73 | 53.79 | 40.43 | 16.20 | 99.80 | 172.51 | 212.43 | 340.03 | 352.55 |
| 40.00 | 27.06 | 30.24 | 55.50 | 53.53 | 40.23 | 16.17 | 99.73 | 171.65 | 211.14 | 338.55 | 351.04 |
| 40.00 | 27.00 | 29.85 | 56.70 | 54.55 | 40.64 | 16.44 | 99.77 | 170.05 | 208.18 | 342.57 | 353.87 |

*Appendix G: Test Stand Data for DX Mode of Operation*

| | | | Refrigerant Temperatures | | | | Refrigerant Pressures | | | | |
|---|---|---|---|---|---|---|---|---|---|---|---|
| **Comp-ressor Speed (Hz)** | **Zone Air Temp (°C)** | **Outdoor Air Temp (°C)** | **Discharge Temp (°C)** | **Condenser Inlet Temp (°C)** | **Condenser Outlet Temp (°C)** | **Suction Temp (°C)** | **Ambient Pressure (kPa)** | **Suction Pressure (psig)** | **Post-EXV Pressure (psig)** | **Condenser Outlet Pressure (psig)** | **Discharge Pressure (psig)** |
| 50.00 | 26.83 | 29.12 | 60.73 | 58.49 | 41.57 | 13.76 | 99.79 | 157.74 | 207.06 | 350.46 | 363.49 |
| 50.00 | 26.96 | 28.89 | 61.33 | 59.04 | 41.94 | 13.81 | 99.57 | 158.07 | 208.11 | 353.90 | 366.65 |
| 50.00 | 27.05 | 28.84 | 60.86 | 58.57 | 42.02 | 13.66 | 99.60 | 158.20 | 208.50 | 354.54 | 367.79 |
| 50.00 | 27.09 | 28.89 | 60.61 | 58.35 | 41.94 | 13.56 | 99.67 | 157.88 | 208.04 | 353.58 | 367.11 |
| 44.29 | 27.22 | 28.94 | 59.32 | 57.08 | 41.05 | 16.17 | 99.70 | 165.46 | 209.21 | 345.76 | 358.21 |
| 33.33 | 27.13 | 27.83 | 50.84 | 48.70 | 36.10 | 18.60 | 99.79 | 175.98 | 205.28 | 305.48 | 313.88 |
| 33.33 | 26.99 | 27.83 | 50.91 | 48.78 | 36.70 | 18.54 | 99.82 | 177.11 | 207.31 | 310.15 | 318.82 |
| 33.33 | 26.90 | 27.64 | 50.89 | 48.78 | 36.62 | 18.45 | 99.72 | 176.87 | 206.93 | 309.53 | 318.47 |
| 33.33 | 26.82 | 27.46 | 51.07 | 48.92 | 36.85 | 18.40 | 99.87 | 177.14 | 207.72 | 311.31 | 320.22 |
| 33.33 | 26.72 | 27.28 | 51.10 | 48.96 | 36.86 | 18.30 | 99.82 | 177.14 | 207.70 | 311.38 | 320.29 |
| 50.00 | 22.38 | 28.79 | 56.47 | 54.44 | 38.98 | 9.81 | 99.90 | 142.67 | 190.19 | 328.61 | 340.35 |
| 50.00 | 22.54 | 29.27 | 57.34 | 55.36 | 40.54 | 10.13 | 99.94 | 144.91 | 195.40 | 341.63 | 354.61 |
| 50.00 | 22.65 | 29.92 | 58.49 | 56.47 | 40.41 | 10.71 | 100.02 | 145.50 | 194.75 | 340.28 | 352.64 |
| 50.00 | 22.78 | 30.44 | 59.84 | 57.70 | 41.35 | 10.96 | 99.86 | 147.23 | 198.08 | 348.55 | 361.83 |
| 50.00 | 22.89 | 30.56 | 60.48 | 58.40 | 41.82 | 11.20 | 99.83 | 147.73 | 198.20 | 352.64 | 365.26 |
| 40.00 | 22.87 | 30.72 | 53.31 | 51.51 | 37.82 | 12.78 | 99.90 | 155.51 | 192.40 | 318.80 | 329.11 |
| 40.00 | 22.63 | 30.86 | 54.41 | 52.55 | 38.79 | 12.99 | 99.85 | 157.12 | 195.03 | 326.60 | 338.09 |
| 40.00 | 22.52 | 30.39 | 54.35 | 52.55 | 38.75 | 13.08 | 99.90 | 158.60 | 197.74 | 326.00 | 338.09 |
| 40.00 | 22.39 | 29.81 | 55.08 | 53.20 | 39.06 | 13.63 | 99.91 | 159.18 | 198.78 | 328.48 | 340.62 |
| 40.00 | 22.30 | 29.61 | 55.05 | 53.17 | 39.00 | 13.44 | 99.91 | 159.16 | 198.81 | 327.94 | 340.20 |
| 33.33 | 22.37 | 29.63 | 49.35 | 47.66 | 35.73 | 14.85 | 99.89 | 165.45 | 196.47 | 301.92 | 311.00 |
| 33.33 | 22.40 | 29.24 | 49.68 | 47.94 | 36.45 | 15.17 | 99.79 | 167.28 | 198.83 | 307.41 | 317.10 |
| 33.33 | 22.42 | 29.48 | 50.17 | 48.41 | 36.70 | 15.29 | 99.91 | 167.92 | 199.36 | 309.41 | 319.04 |
| 33.33 | 22.42 | 29.44 | 50.40 | 48.69 | 36.83 | 15.43 | 99.95 | 168.36 | 199.53 | 310.27 | 319.85 |

| | | | Refrigerant Temperatures | | | | Refrigerant Pressures | | | | |
|---|---|---|---|---|---|---|---|---|---|---|---|
| Comp-ressor Speed (Hz) | Zone Air Temp (°C) | Outdoor Air Temp (°C) | Discharge Temp (°C) | Condenser Inlet Temp (°C) | Condenser Outlet Temp (°C) | Suction Temp (°C) | Ambient Pressure (kPa) | Suction Pressure (psig) | Post-EXV Pressure (psig) | Condenser Outlet Pressure (psig) | Discharge Pressure (psig) |
| 33.33 | 22.42 | 29.58 | 50.46 | 48.78 | 37.08 | 15.25 | 99.86 | 168.96 | 200.81 | 312.25 | 322.09 |
| 26.67 | 22.66 | 29.49 | 45.95 | 44.40 | 34.13 | 17.63 | 99.95 | 177.61 | 201.01 | 289.66 | 296.61 |
| 26.67 | 22.70 | 29.11 | 45.55 | 44.01 | 34.44 | 17.32 | 99.81 | 178.46 | 202.27 | 292.01 | 299.13 |
| 26.67 | 22.76 | 29.05 | 45.71 | 44.13 | 34.61 | 17.70 | 99.78 | 178.93 | 203.10 | 293.21 | 300.39 |
| 26.67 | 22.75 | 28.16 | 45.94 | 44.27 | 34.39 | 17.54 | 99.93 | 178.34 | 202.31 | 291.69 | 298.49 |
| 26.67 | 22.68 | 26.69 | 44.32 | 42.43 | 33.31 | 16.71 | 99.82 | 175.64 | 198.74 | 284.00 | 290.54 |
| 21.67 | 22.72 | 26.07 | 41.12 | 39.15 | 30.41 | 18.44 | 99.89 | 178.28 | 193.97 | 263.59 | 267.59 |
| 21.67 | 22.65 | 26.01 | 41.43 | 39.39 | 31.01 | 18.36 | 99.92 | 178.02 | 193.37 | 268.19 | 272.11 |
| 21.67 | 22.55 | 25.47 | 42.09 | 39.90 | 30.90 | 17.91 | 99.82 | 175.54 | 190.25 | 267.71 | 271.03 |
| 21.67 | 22.49 | 25.37 | 42.45 | 40.14 | 31.19 | 17.73 | 100.10 | 174.55 | 189.12 | 269.96 | 273.08 |
| 21.67 | 22.40 | 25.25 | 42.87 | 40.46 | 31.31 | 17.54 | 99.98 | 173.10 | 186.90 | 271.16 | 274.08 |
| 50.00 | 17.13 | 21.41 | 48.10 | 45.70 | 30.19 | 4.14 | 100.30 | 118.23 | 155.84 | 261.81 | 270.44 |
| 50.00 | 17.34 | 22.34 | 49.64 | 47.20 | 31.83 | 4.58 | 100.25 | 120.57 | 160.42 | 273.52 | 283.27 |
| 50.00 | 17.45 | 22.66 | 50.47 | 47.98 | 32.46 | 4.99 | 100.22 | 121.72 | 162.15 | 278.02 | 287.88 |
| 50.00 | 17.58 | 23.15 | 51.48 | 48.98 | 33.21 | 5.31 | 100.27 | 123.08 | 164.19 | 283.59 | 293.80 |
| 50.00 | 17.67 | 23.62 | 52.48 | 49.90 | 33.93 | 5.87 | 100.26 | 124.53 | 166.78 | 288.88 | 299.55 |
| 40.00 | 17.66 | 24.23 | 46.73 | 44.51 | 30.85 | 8.16 | 100.35 | 132.83 | 164.73 | 265.98 | 274.42 |
| 40.00 | 17.64 | 25.03 | 47.87 | 45.50 | 32.25 | 9.15 | 100.35 | 134.91 | 168.60 | 275.92 | 284.63 |
| 40.00 | 17.63 | 25.34 | 48.49 | 46.25 | 32.73 | 8.58 | 100.43 | 135.87 | 170.33 | 279.42 | 288.89 |
| 40.00 | 17.64 | 25.76 | 49.62 | 47.32 | 33.47 | 9.51 | 100.51 | 137.36 | 172.32 | 284.69 | 294.06 |
| 40.00 | 17.66 | 26.20 | 50.22 | 47.94 | 34.21 | 9.26 | 100.50 | 138.84 | 174.42 | 290.30 | 300.05 |
| 33.33 | 17.86 | 26.05 | 46.66 | 44.33 | 31.45 | 12.03 | 100.42 | 144.98 | 172.77 | 270.05 | 277.11 |
| 33.33 | 17.89 | 26.53 | 47.33 | 44.97 | 32.64 | 11.97 | 100.43 | 145.02 | 172.10 | 279.01 | 286.03 |
| 33.33 | 17.95 | 27.20 | 49.10 | 46.67 | 33.68 | 11.53 | 100.42 | 147.18 | 176.54 | 286.35 | 294.75 |

| Condenser Conditions | | Evaporator Conditions | | Power Measurements | |
|---|---|---|---|---|---|
| Condenser Air Inlet Temp (°C) | Condenser Air Temp Difference (°C) | Evaporator Volumetric Flow Rate ($m^3/s$) | Refrigerant Mass Flow Rate (kg/s) | Compressor Three Phase Power (W) | Fan Three Phase Power (W) |
| 35.71 | 3.42 | 0.158 | 0.011 | 171.83 | 23.21 |
| 36.74 | 3.60 | 0.158 | 0.012 | 177.09 | 22.78 |
| 37.64 | 3.62 | 0.158 | 0.012 | 181.16 | 16.44 |
| 36.24 | 5.09 | 0.158 | 0.013 | 230.43 | 22.78 |
| 35.41 | 5.61 | 0.158 | 0.013 | 226.76 | 24.32 |
| 34.70 | 6.03 | 0.158 | 0.013 | 224.74 | 16.81 |
| 35.25 | 7.58 | 0.158 | 0.013 | 238.13 | 4.30 |
| 35.68 | 7.07 | 0.158 | 0.014 | 316.85 | 22.62 |
| 36.27 | 7.76 | 0.158 | 0.015 | 330.60 | 23.78 |
| 34.30 | 8.46 | 0.158 | 0.014 | 321.37 | 22.51 |
| 34.79 | 9.69 | 0.158 | 0.016 | 432.86 | 23.60 |
| 33.82 | 10.08 | 0.158 | 0.016 | 426.48 | 24.52 |
| 33.08 | 10.77 | 0.158 | 0.016 | 425.93 | 16.21 |
| 30.39 | 6.66 | 0.158 | 0.014 | 381.72 | 29.61 |
| 30.33 | 6.73 | 0.158 | 0.014 | 386.46 | 26.33 |
| 30.24 | 5.83 | 0.158 | 0.014 | 383.50 | 25.99 |
| 29.85 | 6.74 | 0.158 | 0.013 | 391.79 | 24.27 |
| 29.12 | 9.04 | 0.158 | 0.015 | 528.74 | 29.35 |
| 28.89 | 8.55 | 0.158 | 0.015 | 536.27 | 27.46 |
| 28.84 | 8.25 | 0.158 | 0.015 | 536.19 | 25.80 |
| 28.89 | 8.10 | 0.158 | 0.015 | 534.25 | 24.64 |
| 28.94 | 8.35 | 0.158 | 0.014 | 450.44 | 15.94 |
| 27.83 | 6.66 | 0.158 | 0.012 | 265.74 | 29.77 |
| 27.83 | 7.51 | 0.158 | 0.012 | 271.79 | 27.30 |

| Condenser Conditions | | Evaporator Conditions | | Power Measurements | |
|---|---|---|---|---|---|
| **Condenser Air Inlet Temp (°C)** | **Condenser Air Temp Difference (°C)** | **Evaporator Volumetric Flow Rate ($m^3/s$)** | **Refrigerant Mass Flow Rate (kg/s)** | **Compressor Three Phase Power (W)** | **Fan Three Phase Power (W)** |
| 27.64 | 7.68 | 0.158 | 0.012 | 270.94 | 25.71 |
| 27.46 | 7.69 | 0.158 | 0.012 | 273.60 | 24.60 |
| 27.28 | 7.96 | 0.158 | 0.012 | 273.52 | 16.09 |
| 28.79 | 9.26 | 0.158 | 0.013 | 501.04 | 29.06 |
| 29.27 | 10.28 | 0.158 | 0.015 | 524.11 | 26.21 |
| 29.92 | 10.25 | 0.158 | 0.015 | 520.92 | 26.09 |
| 30.44 | 10.51 | 0.158 | 0.015 | 534.82 | 24.89 |
| 30.56 | 10.95 | 0.158 | 0.015 | 541.76 | 16.31 |
| 30.72 | 7.44 | 0.158 | 0.013 | 366.91 | 29.01 |
| 30.86 | 8.20 | 0.158 | 0.013 | 377.91 | 26.44 |
| 30.39 | 8.32 | 0.158 | 0.013 | 376.99 | 25.12 |
| 29.81 | 8.63 | 0.158 | 0.014 | 380.10 | 24.29 |
| 29.61 | 8.78 | 0.158 | 0.013 | 379.71 | 16.28 |
| 29.63 | 5.66 | 0.158 | 0.012 | 272.62 | 28.94 |
| 29.24 | 6.56 | 0.158 | 0.012 | 279.08 | 25.89 |
| 29.48 | 6.68 | 0.158 | 0.012 | 281.32 | 25.31 |
| 29.44 | 6.88 | 0.158 | 0.012 | 282.81 | 24.20 |
| 29.58 | 7.02 | 0.158 | 0.012 | 284.71 | 16.02 |
| 29.49 | 4.30 | 0.158 | 0.011 | 191.58 | 28.79 |
| 29.11 | 4.95 | 0.158 | 0.011 | 192.61 | 26.17 |
| 29.05 | 5.22 | 0.158 | 0.011 | 193.83 | 25.74 |
| 28.16 | 5.57 | 0.158 | 0.011 | 192.63 | 23.93 |
| 26.69 | 6.01 | 0.158 | 0.011 | 185.48 | 16.25 |
| 26.07 | 3.96 | 0.158 | 0.009 | 133.54 | 29.38 |

| Condenser Conditions | | Evaporator Conditions | | Power Measurements | |
|---|---|---|---|---|---|
| **Condenser Air Inlet Temp (°C)** | **Condenser Air Temp Difference (°C)** | **Evaporator Volumetric Flow Rate ($m^3/s$)** | **Refrigerant Mass Flow Rate (kg/s)** | **Compressor Three Phase Power (W)** | **Fan Three Phase Power (W)** |
| 26.01 | 4.54 | 0.158 | 0.009 | 138.85 | 25.80 |
| 25.47 | 4.98 | 0.158 | 0.009 | 140.85 | 25.12 |
| 25.37 | 5.27 | 0.158 | 0.008 | 144.28 | 23.66 |
| 25.25 | 5.59 | 0.158 | 0.008 | 146.77 | 17.19 |
| 21.41 | 7.95 | 0.158 | 0.012 | 401.52 | 29.36 |
| 22.34 | 8.86 | 0.158 | 0.012 | 420.93 | 26.21 |
| 22.66 | 9.20 | 0.158 | 0.012 | 427.30 | 25.37 |
| 23.15 | 9.50 | 0.158 | 0.012 | 435.83 | 24.61 |
| 23.62 | 9.76 | 0.158 | 0.013 | 443.83 | 16.40 |
| 24.23 | 6.11 | 0.158 | 0.011 | 308.01 | 29.42 |
| 25.03 | 6.81 | 0.158 | 0.012 | 320.80 | 27.06 |
| 25.34 | 6.97 | 0.158 | 0.012 | 326.28 | 25.49 |
| 25.76 | 7.34 | 0.158 | 0.012 | 332.98 | 24.00 |
| 26.20 | 7.57 | 0.158 | 0.012 | 339.54 | 16.92 |
| 26.05 | 4.91 | 0.158 | 0.011 | 248.40 | 29.21 |
| 26.53 | 5.65 | 0.158 | 0.011 | 260.00 | 25.56 |
| 27.20 | 5.87 | 0.158 | 0.011 | 269.02 | 25.09 |

# Appendix H

## Test Stand Data for Chiller Mode of Operation

| | | | | Refrigerant Temperatures | | | | Refrigerant pressures | | | | |
|---|---|---|---|---|---|---|---|---|---|---|---|---|
| Comp-ressor Speed (Hz) | Condenser Fan Speed (RPM) | Zone Air Temp (°C) | Outdoor Air Temp (°C) | Discharge Temp (°C) | Condenser Inlet Temp (°C) | Condenser Outlet Temp (°C) | Suction Temp (°C) | Ambient Pressure (kPa) | Suction Pressure (psig) | Post-EXV Pressure (psig) | Condenser Outlet Pressure (psig) | Discharge Pressure (psig) |
| 33.33 | 690.50 | 27.22 | 27.85 | 53.23 | 50.94 | 31.92 | 21.54 | 98.87 | 181.37 | 187.03 | 318.94 | 321.29 |
| 33.33 | 502.70 | 27.10 | 28.44 | 56.70 | 54.26 | 34.06 | 21.60 | 98.87 | 181.88 | 187.41 | 336.12 | 338.44 |
| 33.33 | 387.50 | 27.00 | 28.24 | 58.64 | 56.01 | 35.93 | 21.64 | 98.83 | 181.93 | 187.43 | 350.92 | 353.52 |
| 26.67 | 895.50 | 26.73 | 27.49 | 48.85 | 46.49 | 30.00 | 22.12 | 99.00 | 185.06 | 188.79 | 301.37 | 301.87 |
| 26.67 | 686.30 | 26.69 | 27.09 | 50.13 | 47.69 | 30.24 | 22.12 | 99.02 | 185.02 | 188.76 | 304.79 | 305.40 |
| 26.67 | 498.70 | 26.67 | 28.57 | 53.05 | 50.29 | 32.63 | 22.19 | 98.90 | 185.29 | 189.06 | 323.18 | 323.99 |
| 26.67 | 384.40 | 26.69 | 32.28 | 62.13 | 58.59 | 38.03 | 22.43 | 99.12 | 186.64 | 190.38 | 365.67 | 367.04 |
| 26.67 | 889.80 | 26.78 | 32.73 | 57.79 | 53.89 | 34.21 | 17.77 | 98.98 | 160.71 | 163.92 | 331.01 | 331.49 |
| 26.67 | 681.20 | 26.85 | 33.62 | 60.85 | 56.60 | 35.66 | 17.94 | 99.29 | 161.56 | 164.70 | 343.40 | 343.96 |
| 26.67 | 498.40 | 26.94 | 34.56 | 64.63 | 59.87 | 37.74 | 18.00 | 99.22 | 161.94 | 165.05 | 361.12 | 361.55 |
| 33.33 | 898.80 | 26.69 | 26.70 | 51.90 | 49.13 | 29.14 | 17.06 | 98.97 | 156.85 | 161.22 | 296.98 | 298.15 |
| 33.33 | 688.20 | 26.44 | 26.65 | 52.85 | 50.03 | 29.80 | 17.06 | 99.25 | 156.98 | 161.23 | 302.93 | 304.14 |
| 33.33 | 505.20 | 26.25 | 26.75 | 55.40 | 52.41 | 31.10 | 17.12 | 98.96 | 157.18 | 161.42 | 313.38 | 314.73 |
| 33.33 | 389.30 | 26.05 | 28.49 | 60.67 | 57.24 | 34.36 | 16.85 | 99.13 | 155.66 | 159.81 | 338.42 | 339.73 |
| 33.33 | 897.75 | 25.97 | 27.91 | 52.12 | 49.91 | 30.80 | 21.29 | 99.13 | 180.13 | 185.19 | 310.10 | 312.31 |
| 43.33 | 893.30 | 27.34 | 27.82 | 60.12 | 57.65 | 32.69 | 15.28 | 98.96 | 147.79 | 158.09 | 327.39 | 333.39 |
| 43.33 | 685.30 | 27.18 | 28.06 | 62.44 | 59.85 | 34.12 | 15.14 | 98.93 | 146.83 | 157.08 | 338.71 | 344.85 |
| 43.33 | 503.80 | 27.03 | 28.04 | 65.41 | 62.70 | 36.15 | 15.31 | 99.05 | 147.78 | 158.24 | 355.23 | 361.51 |

# *Appendix H: Test Stand Data for Chiller Mode of Operation*

| | | | | Refrigerant Temperatures | | | | Refrigerant pressures | | | | |
|---|---|---|---|---|---|---|---|---|---|---|---|---|
| **Comp-ressor Speed (Hz)** | **Condenser Fan Speed (RPM)** | **Zone Air Temp (°C)** | **Outdoor Air Temp (°C)** | **Discharge Temp (°C)** | **Condenser Inlet Temp (°C)** | **Condenser Outlet Temp (°C)** | **Suction Temp (°C)** | **Ambient Pressure (kPa)** | **Suction Pressure (psig)** | **Post-EXV Pressure (psig)** | **Condenser Outlet Pressure (psig)** | **Discharge Pressure (psig)** |
| 43.33 | 897.70 | 26.86 | 28.41 | 56.48 | 54.33 | 33.10 | 20.54 | 99.16 | 175.71 | 183.98 | 328.71 | 334.77 |
| 43.33 | 504.80 | 26.76 | 27.19 | 59.04 | 56.79 | 34.91 | 20.57 | 99.13 | 175.64 | 183.93 | 343.89 | 349.89 |
| 43.33 | 688.30 | 26.69 | 27.36 | 56.33 | 54.19 | 33.06 | 20.42 | 99.17 | 175.00 | 183.18 | 329.09 | 334.81 |
| 53.33 | 612.94 | 28.62 | 30.17 | 66.32 | 63.63 | 36.98 | 15.30 | 99.02 | 147.89 | 158.84 | 360.52 | 366.61 |
| 53.33 | 898.64 | 28.32 | 30.30 | 62.75 | 60.38 | 35.82 | 17.61 | 99.02 | 160.02 | 171.82 | 350.10 | 357.59 |
| 53.33 | 610.60 | 28.04 | 30.05 | 64.99 | 62.76 | 38.46 | 19.74 | 98.98 | 170.97 | 183.67 | 371.32 | 379.54 |
| 53.33 | 504.13 | 27.84 | 30.11 | 67.19 | 64.85 | 40.15 | 19.75 | 99.12 | 171.45 | 184.16 | 385.01 | 394.14 |
| 53.33 | 795.63 | 27.66 | 29.55 | 62.68 | 60.36 | 35.75 | 17.90 | 98.86 | 161.55 | 173.21 | 349.86 | 357.68 |
| 40.00 | 878.25 | 33.44 | 35.57 | 61.58 | 59.96 | 41.56 | 28.83 | 98.59 | 227.02 | 239.52 | 395.38 | 402.30 |
| 33.33 | 870.00 | 33.95 | 35.29 | 58.85 | 57.12 | 39.87 | 29.61 | 98.65 | 232.39 | 242.28 | 381.79 | 386.37 |
| 26.67 | 873.17 | 34.10 | 35.09 | 56.20 | 54.40 | 38.25 | 29.99 | 98.56 | 235.04 | 242.92 | 367.84 | 370.27 |
| 50.00 | 504.10 | 32.05 | 30.76 | 66.03 | 64.03 | 41.83 | 24.12 | 98.64 | 196.81 | 212.12 | 399.31 | 408.01 |
| 40.00 | 895.88 | 31.20 | 30.18 | 56.19 | 54.38 | 35.23 | 24.72 | 98.61 | 200.52 | 211.23 | 345.86 | 351.42 |
| 33.33 | 870.10 | 30.62 | 30.01 | 53.29 | 51.42 | 33.92 | 25.47 | 98.57 | 205.16 | 213.65 | 335.08 | 338.27 |
| 26.67 | 873.25 | 29.99 | 29.19 | 50.05 | 48.07 | 32.10 | 25.97 | 98.69 | 208.32 | 214.84 | 319.90 | 320.79 |

| Condenser Conditions | | Evaporator Conditions | | | | | | Power Measurements | | | |
|---|---|---|---|---|---|---|---|---|---|---|---|
| **Condenser Air Inlet Temp (°C)** | **Condenser Air Temp Difference (°C)** | **Evaporator Inlet Temp (°C)** | **Evaporator Outlet Temp (°C)** | **Water Inlet Temp (°C)** | **Water Outlet Temp (°C)** | **Water Volumetric Flow Rate (L/s)** | **Refrigerant Mass Flow Rate (kg/s)** | **Cooling Load (W)** | **Compressor Three Phase Power (W)** | **Fan Three Phase Power (W)** | **Pump Power (W)** |
| 27.85 | 5.10 | 16.51 | 21.19 | 22.22 | 20.08 | 0.268 | 0.015 | 2464.84 | 276.03 | 18.73 | 22.89 |
| 28.44 | 7.17 | 16.69 | 21.25 | 22.18 | 20.11 | 0.270 | 0.015 | 2378.82 | 301.81 | 6.22 | 22.91 |
| 28.24 | 9.46 | 16.74 | 21.29 | 22.13 | 20.11 | 0.272 | 0.015 | 2322.96 | 323.32 | 2.61 | 22.91 |
| 27.49 | 3.19 | 16.77 | 21.68 | 22.26 | 20.45 | 0.272 | 0.013 | 2039.09 | 193.66 | 46.24 | 23.05 |
| 27.09 | 4.21 | 16.80 | 21.58 | 22.19 | 20.40 | 0.272 | 0.012 | 2034.36 | 199.23 | 18.72 | 23.05 |
| 28.57 | 5.84 | 16.96 | 21.62 | 22.19 | 20.46 | 0.268 | 0.012 | 1959.47 | 222.17 | 6.03 | 23.09 |
| 32.28 | 7.59 | 17.44 | 21.73 | 22.24 | 20.68 | 0.272 | 0.012 | 1755.68 | 282.06 | 2.66 | 23.07 |
| 32.73 | 2.55 | 12.66 | 16.80 | 17.21 | 15.95 | 0.261 | 0.010 | 1569.85 | 258.87 | 45.26 | 23.03 |
| 33.62 | 3.38 | 12.85 | 16.71 | 17.16 | 15.95 | 0.260 | 0.010 | 1525.97 | 274.84 | 18.62 | 23.00 |
| 34.56 | 4.73 | 12.96 | 16.68 | 17.11 | 15.97 | 0.259 | 0.010 | 1450.65 | 302.87 | 6.51 | 22.98 |
| 26.70 | 3.39 | 11.85 | 16.41 | 17.14 | 15.28 | 0.260 | 0.013 | 2139.53 | 270.31 | 46.42 | 22.60 |
| 26.65 | 4.47 | 11.90 | 16.37 | 17.11 | 15.26 | 0.260 | 0.013 | 2128.38 | 279.43 | 18.86 | 22.60 |
| 26.75 | 6.24 | 11.97 | 16.38 | 17.09 | 15.29 | 0.260 | 0.013 | 2080.77 | 296.73 | 6.36 | 22.60 |
| 28.49 | 8.05 | 11.76 | 16.01 | 16.63 | 14.95 | 0.260 | 0.012 | 1940.06 | 330.09 | 2.63 | 22.60 |
| 27.91 | 3.75 | 16.14 | 21.06 | 22.04 | 19.74 | 0.260 | 0.015 | 2496.06 | 263.51 | 46.61 | 22.60 |
| 27.82 | 5.23 | 11.01 | 15.18 | 17.44 | 14.75 | 0.260 | 0.019 | 3118.56 | 528.35 | 45.98 | 22.60 |
| 28.06 | 6.82 | 10.83 | 15.34 | 17.09 | 14.48 | 0.260 | 0.019 | 3032.27 | 553.08 | 18.71 | 22.60 |
| 28.04 | 9.51 | 11.06 | 15.57 | 17.15 | 14.61 | 0.260 | 0.019 | 2955.56 | 588.13 | 6.30 | 22.60 |
| 28.41 | 4.90 | 15.88 | 20.95 | 22.27 | 19.50 | 0.260 | 0.019 | 3070.34 | 389.20 | 46.29 | 22.60 |
| 27.19 | 9.02 | 15.94 | 20.97 | 22.13 | 19.45 | 0.260 | 0.018 | 2977.50 | 418.61 | 6.47 | 22.60 |
| 27.36 | 6.44 | 15.73 | 20.84 | 22.13 | 19.35 | 0.260 | 0.018 | 3056.03 | 393.04 | 18.88 | 22.60 |
| 30.17 | 7.64 | 11.20 | 15.41 | 17.21 | 14.75 | 0.260 | 0.019 | 2923.53 | 600.57 | 12.35 | 22.60 |
| 30.30 | 5.50 | 13.52 | 17.76 | 20.05 | 17.19 | 0.260 | 0.021 | 3285.24 | 566.31 | 46.31 | 22.60 |
| 30.05 | 8.74 | 15.70 | 20.21 | 22.29 | 19.28 | 0.260 | 0.022 | 3401.19 | 599.87 | 12.29 | 22.60 |
| 30.11 | 10.70 | 15.82 | 20.14 | 22.23 | 19.29 | 0.260 | 0.022 | 3328.37 | 630.00 | 6.28 | 22.60 |

*Appendix H: Test Stand Data for Chiller Mode of Operation*

| Condenser Conditions | | Evaporator Conditions | | | | | | Power Measurements | | | |
|---|---|---|---|---|---|---|---|---|---|---|---|
| Condenser Air Inlet Temp (°C) | Condenser Air Temp Difference (°C) | Evaporator Inlet Temp (°C) | Evaporator Outlet Temp (°C) | Water Inlet Temp (°C) | Water Outlet Temp (°C) | Water Volumetric Flow Rate (L/s) | Refrigerant Mass Flow Rate (kg/s) | Cooling Load (W) | Compressor Three Phase Power (W) | Fan Three Phase Power (W) | Pump Power (W) |
| 29.55 | 6.33 | 13.78 | 17.84 | 20.37 | 17.47 | 0.260 | 0.021 | 3310.70 | 562.91 | 29.91 | 22.60 |
| 35.57 | 5.72 | 24.88 | 28.66 | 31.21 | 28.22 | 0.247 | 0.022 | 2896.58 | 407.67 | 44.37 | 22.54 |
| 35.29 | 4.92 | 25.26 | 29.92 | 31.16 | 28.48 | 0.242 | 0.019 | 2964.56 | 307.26 | 43.82 | 22.58 |
| 35.09 | 3.91 | 25.44 | 29.88 | 30.86 | 28.73 | 0.254 | 0.016 | 2511.40 | 223.31 | 43.60 | 22.58 |
| 30.76 | 11.48 | 20.43 | 24.07 | 26.99 | 23.93 | 0.236 | 0.023 | 3540.12 | 576.80 | 6.13 | 22.62 |
| 30.18 | 5.15 | 20.32 | 24.55 | 26.85 | 24.04 | 0.231 | 0.020 | 3205.77 | 354.30 | 46.07 | 22.64 |
| 30.01 | 4.42 | 20.72 | 25.79 | 26.69 | 24.24 | 0.237 | 0.017 | 2799.86 | 269.70 | 44.96 | 22.61 |
| 29.19 | 3.61 | 20.84 | 26.19 | 26.44 | 24.41 | 0.238 | 0.014 | 2325.41 | 188.65 | 44.57 | 22.54 |

# Appendix I

## Nomenclature

| | | | |
|---|---|---|---|
| A | Area (m) | n | Polytropic exponent |
| cp | Specific heat (J/kg.K) | $n_s$ | Isentropic exponent |
| $D_{in}$ | Tube inside diameter (m) | P | Pressure (kPa) |
| $D_o$ | Tube outside diameter (m) | $P_{fin}$ | Heat exchanger fin pitch |
| $D_c$ | Collar diameter (m) $D_c = D_o + 2 * t_{fin}$ | $P_{longitudnal}$ | Longitudinal pitch of heat exchanger |
| dP | Pressure drop | $P_{transverse}$ | Transversal pitch of heat exchanger |
| e | Void fraction | Pr | Prandtl number $Pr = \mu * cp/k$ |
| Fr | Froude number | Q | Heat (W) |
| f | Friction factor | $Q_{load}$ | Evaporator heat load (W) |
| $f_{comp}$ | Compressor speed (Hz) | $q_{flux}$ | Heat flux ($Q_{Flux} = Q/A$) (W/m$^2$) |
| G | Mass velocity or mass flux ($G = \dot{m}/A$) (kg/s.m$^2$) | RMSE | Root Mean Squared Error $RMSE = \sqrt{\frac{\sum(\text{Predicted}-\text{Actual})^2}{\text{Data Points}}}$ |
| h | Specific enthalpy (J/kg) | Re | Reynolds number ($R_e = G * D/\mu$) |
| $h_{conv}$ | Single-phase convection heat transfer coefficient (W/m$^2$.K) | $R_{eq}$ | Equivalent radius (m) |
| $h_{conv_{out}}$ | Air-side heat transfer coefficient (W/m$^2$.K) | r | Tube radius (m) |

*Appendix I: Nomenclature*

| | | | |
|---|---|---|---|
| $h_{conv_{in}}$ | Refrigerant-side heat transfer coefficient (W/m$^2$.K) | T | Temperature (K) |
| $h_{fgref}$ | Latent heat of vaporization (J/kg) | $T_i$ | Integral time (sec) |
| k | Thermal conductivity (W/m.K) | $T_d$ | Derivative time (sec) |
| kW | Compressor power (kW) | $t_{fin}$ | Fin thickness (m) |
| $L_{element}$ | Element length (m) | $t_{plate}$ | Plate thickness (m) |
| M | Molar mass (g/mol) | $tube_{row}$ | Number of tube rows in longitudinal direction |
| RMSPE | Root Mean Squared Percentage Error $\text{RMSPE}=\sqrt{\frac{\Sigma\left(\frac{\text{Predicted}-\text{Actual}}{\text{Actual}}\right)^2}{\text{Data Points}}}$ | U | Heat transfer conductance (K.m$^2$/W) |
| $\dot{m}$ | Mass flow rate (kg/sec) | $\dot{V}_{air}$ | Volumetric flow rate of air (m$^3$/s) |
| NTU | Number of transfer units | v | Velocity (m/s) |
| Nu | Nusselt number | We | Weber number |
| x | Vapor quality $x = \frac{m_g}{m_{liq}+m_g+m_{oil}}$ | | |

**Greek Letters:**

| | | | |
|---|---|---|---|
| ρ | Density (kg/m$^3$) | μ | Viscosity (Pa.s) |
| σ | Surface tension (N/m) | ω | Oil concentration |
| ν | Specific volume (m$^3$/kg) | η | Efficiency |
| ε | Effectiveness | θ | Angle (radians) |
| δ | Thickness (m) | ϕ | Area enlargement factor |
| β | Chevron angle | | |

**Sub-scripts:**

| | | | |
|---|---|---|---|
| amb | Ambient | max | Maximum |
| bulb | Saturation temperature of refrigerant-oil mixture | min | Minimum |
| comb | Combined | $\mathrm{min_{air}}$ | Element area exposed to air |
| cond | Condenser | oil | Refrigerant oil POE/VG68 |
| $\mathrm{cond_{out}}$ | Condenser outlet | out | Output from element |
| comp | Compressor | plate | Brazed-Plate heat exchanger |
| crit | Critical | port | Brazed-Plate HX inlet/outlet port |
| dis | Discharge | ref | Refrigerant |
| evap | Evaporator | $\mathrm{ref_{liq}}$ | Liquid phase of refrigerant |
| $\mathrm{evap_{in}}$ | Evaporator inlet | $\mathrm{ref_g}$ | Gas phase of refrigerant |
| $\mathrm{evap_{out}}$ | Evaporator outlet | ref-oil | Refrigerant-oil mixture |
| eq | Equivalent | sat | Saturation |
| fin | Heat exchanger fins | strat | Stratified |
| g | Gas | suc | Suction |
| gD | Gas portion of tube in two-phase | surf | Surface |
| IA | Intermittent-annular | $\mathrm{surf_{total}}$ | Element surface area exposed to air |
| in | Input to the element | tp | Two-phase |
| liq | Liquid | tube | Tube of fan-coil heat exchanger |
| liqD | Liquid portion of tube in two-phase | v | Volumetric |
| liqfilm | Liquid film in two-phase | x | Outdoor |
| local | Local oil concentration | z | Indoor |

# Bibliography

Ali, M. T., Mokhtar, M., Chiesa, M., & Armstrong, P. (2011). A cooling change-point model of community-aggregate electrical load. *Energy and Buildings*, *43*(1), 28-37.

Allen, J. J., & Hamilton, J. F. (1983). Steady-state reciprocating water chiller models. *ASHRAE Transactions*, *89*(2A), 398–407.

Armstrong, P. R., Jiang, W., Winiarski, D., Katipamula, S., & Norford, L. K. (2009). Efficient low-lift cooling with radiant distribution, thermal storage, and variable-speed chiller controls—Part II: Annual use and energy savings. *HVAC&R Research*, *15*(2), 402–432.

Armstrong, P. R., Jiang, W., Winiarski, D., Katipamula, S., Norford, L. K., & Willingham, R. A. (2009). Efficient low-lift cooling with radiant distribution, thermal storage, and variable-speed chiller controls—Part I: Component and subsystem models. *HVAC&R Research*, *15*(2), 366–401.

Arslan Khalid. (2011). Personal Communication.

Ayub, Z. H. (2003). Plate heat exchanger literature survey and new heat transfer and pressure drop correlations for refrigerant evaporators. *Heat transfer engineering*, *24*(5), 3–16.

Bandarra Filho, E. P., Cheng, L., & Thome, J. R. (2009). Flow boiling characteristics and flow pattern visualization of refrigerant/lubricant oil mixtures. *International Journal of Refrigeration*, *32*(2), 185–202.

Bendapudi, S., & Braun, J. E. (2002). A review of literature on dynamic models of vapor compression equipment. *ASHRAE Report*, *HL 2002-9 Report #4036-5*.

Boissieux, X., Heikal, M. R., & Johns, R. A. (2000a). Two-phase heat transfer coefficients of three HFC refrigerants inside a horizontal smooth tube—Part II: Condensation. *International Journal of Refrigeration*, *23*(5), 345-352.

Boissieux, X., Heikal, M. R., & Johns, R. A. (2000b). Two-phase heat transfer coefficients of three HFC refrigerants inside a horizontal smooth tube—Part I: Evaporation. *International Journal of Refrigeration*, *23*(4), 269-283.

Brown, R. N. (1997). *Compressors: Selection and Sizing*. Gulf Professional Publishing.

Browne, M. W., & Bansal, P. K. (2001). An elemental NTU-model for vapor-compression liquid chillers. *International Journal of Refrigeration*, *24*(7), 612–627.

Cavallini, A., Censi, G., Del Col, D., Doretti, L., Longo, G. A., & Rossetto, L. (2002). In-tube condensation of halogenated refrigerants. *ASHRAE Transactions*, *108*(4507), 146–161.

Chen, I. Y., Wang, C.-C., & Lin, S. Y. (2004). Measurements and correlations of frictional single-phase and two-phase pressure drops of R-410A flow in small U-type return bends. *International Journal of Heat and Mass Transfer*, *47*(10-11), 2241-2249.

Chen, I. Y., Wu, Y.-S., Chang, Y.-J., & Wang, C.-C. (2007). Two-phase frictional pressure drop of R-134a and R-410A refrigerant-oil mixtures in straight tubes and U-type wavy tubes. *Experimental Thermal and Fluid Science*, *31*(4), 291-299.

Cho, K., & Tae, S.-J. (2001). Condensation heat transfer for R-22 and R-407C refrigerant-oil mixtures in a micro-fin tube with a U-bend. *International Journal of Heat and Mass Transfer*, *44*(11), 2043-2051.

Choi, J. Y., Kedzierski, M. A., & Domański, P. (1999). *A generalized pressure drop correlation for evaporation and condensation of alternative refrigerants in smooth and micro-fin* *tubes*. US Dept. of Commerce, Technology Administration, National Institute of Standards and Technology, Building and Fire Research Laboratory.

Claesson, J. (2005). *Thermal and hydraulic performance of compact brazed plate heat exchangers operating as evaporators in domestic heat pumps* (Ph.D. thesis). KTH, Sweden: Royal Institute of Technology.

Cohen, R., Hamilton, J. F., & Pearson, J. T. (1974). Possible energy conservation through the use of variable capacity compressor. *Proceedings Purdue Compressor Technology Conference, Purdue, US* (pp. 50–55).

Conde, M. R. (1996). Estimation of thermophysical properties of lubricating oils and their solutions with refrigerants: an appraisal of existing methods. *Applied thermal engineering*, *16*(1), 51–61.

Cooper, M. G. (1984). Heat flow rates in saturated nucleate pool boiling-a wide-ranging examination using reduced properties. *Advances in heat transfer*, *16*, 157–239.

Damasceno, G. S., Goldschmidt, V. W., & Rooke, S. P. (1990). Comparison of three steady-state heat pump computer models. *ASHRAE Transactions*, *96*(2), 191–204.

Doerr, T. M., Pate, M. B., & Eckels, S. J. (1994). In-tube heat transfer and pressure drop of R-134a and ester lubricant mixtures in a smooth tube and a micro-fin tube: part I - evaporation. *ASHRAE Transactions*, *100*(2), 265-282.

Domanski, P., & Didion, D. (1984). Mathematical model of an air-to-air heat pump equipped with a capillary tube. *International Journal of Refrigeration*, *7*(4), 249–255.

El Hajal, J., Thome, J. R., & Cavallini, A. (2003). Condensation in horizontal tubes, part 1: two-phase flow pattern map. *International Journal of Heat and Mass Transfer*, *46*(18), 3349–3363.

Feustel, H. E., & Stetiu, C. (1995). Hydronic radiant cooling–preliminary assessment. *Energy and buildings*, *22*(3), 193–205.

Fischer, S. K., Rice, C. K., & Jackson, W. L. (1988). The Oak Ridge Heat Pump Design Model: Mark III Version Program Documentation. *ORNL/TM-10192*.

Friedel, L. (1979). Improved friction pressure drop correlations for horizontal and vertical two-phase pipe flow. *European two-phase flow group meeting, Paper E* (Vol. 2).

Fukuta, M., Yanagisawa, T., Miyamura, S., & Ogi, Y. (2004). Concentration measurement of refrigerant/refrigeration oil mixture by refractive index. *International Journal of Refrigeration*, *27*(4), 346-352.

García-Cascales, J. R., Vera-García, F., Corberán-Salvador, J. M., & Gonzálvez-Maciá, J. (2007). Assessment of boiling and condensation heat transfer correlations in the modelling of plate heat exchangers. *International Journal of Refrigeration*, *30*(6), 1029–1041.

Gayeski, N. T. (2010). Predictive pre-cooling control for low lift radiant cooling using building thermal mass. (PhD Thesis). Massachusetts Institute of Technology.

Gayeski, N. T., Zakula, T., Armstrong, P. R., & Norford, L. K. (2010). Empirical Modeling of a Rolling-Piston Compressor Heat Pump for Predictive Control in Low Lift Cooling. *ASHRAE Transactions*, *116*(1).

Gnielinski, V. (1976). New equations for heat and mass transfer in turbulent pipe and channel flow. *Int. Chem. Eng*, *16*(2), 359–368.

Gray, D. L., & Webb, R. L. (1986). Heat transfer and friction correlations for plate finned-tube heat exchangers having plain fins. *Proceedings of the 8th International Heat Transfer Conference* (Vol. 6, pp. 2745–2750).

Grönnerud, R. (1972). Investigation of Liquid Hold-Up, Flow-Resistance and Heat Transfer in Circulation Type Evaporators, Part IV: Two-Phase Flow Resistance in Boiling Refrigerants. *Bull. De l'Inst. Du Froid, Annexe*, *1*.

Hambraeus, K. (1995). Heat transfer of oil-contaminated HFC134a in a horizontal evaporator. *International Journal of Refrigeration*, *18*(2), 87-99.

Hamilton, J. F., & Miller, J. L. (1990). A simulation program for modeling an air-conditioning system. *ASHRAE Transactions*, *96*(1), 213–221.

Han, D. H., Lee, K. J., & Kim, Y. H. (2003). Experiments on the characteristics of evaporation of R410A in brazed plate heat exchangers with different geometric configurations. *Applied thermal engineering*, *23*(10), 1209–1225.

Harp Lubricants – Technical Data SheetHarp Polyol Ester Oils. Harp International.

Hermetic Compressors. (2011). . Retrieved May 3, 2011, from http://www.refrigers.com/content/view/31439/28/

Hiller, C. C., & Glicksman, L. R. (1976). *Improving heat pump performance via compressor capacity control: analysis and test*. MIT Energy Lab.

Hsieh, Y. Y., & Lin, T. F. (2002). Saturated flow boiling heat transfer and pressure drop of refrigerant R-410A in a vertical plate heat exchanger. *International journal of heat and mass transfer*, *45*(5), 1033–1044.

Hsieh, Y. Y., & Lin, T. F. (2003). Evaporation heat transfer and pressure drop of refrigerant R-410A flow in a vertical plate heat exchanger. *Journal of heat transfer*, *125*, 852.

Hu, H., Ding, G., Wei, W., Wang, Z., & Wang, K. (2008). Heat transfer characteristics of R410A-oil mixture flow boiling inside a 7 mm straight smooth tube. *Experimental Thermal and Fluid Science*, *32*(3), 857–869.

Iu, I. S. (2007). *Development of air-to-air heat pump simulation program with advanced heat exchanger circuitry algorithm*. Oklahoma State University.

Jacobi, A. M., Park, Y., Tafti, D., & Zhang, X. (2001). *An Assessment of The State of The Art, And Potential Design Improvements, For Flat-Tube Heat Exchangers In Air Conditioning And Refrigeration Applications-Phase I*. Air-Conditioning and Refrigeration Technology Institute, Arlington, VA (US).

Jähnig, D. I., Reindl, D. T., & Klein, S. A. (2000). A semi-empirical method for representing domestic refrigerator/freezer compressor calorimeter test data. *ASHRAE Transactions*, *106*(4379 (RP-870)), 122–30.

Jeong, J., Kim, C. N., & Youn, B. (2006). A study on the thermal contact conductance in fin-tube heat exchangers with 7 mm tube. *International Journal of Heat and Mass Transfer*, *49*(7-8), 1547-1555.

Jin, H., & Spitler, J. D. (2002). A parameter estimation based model of water-to-water heat pumps for use in energy calculation programs. *ASHRAE Transactions*, *108*(4493), 3–17.

Lebreton, J. M., Vuillame, L., Morvan, E., & Lottin, O. (2001). Oil Concentration Measurement In Saturated Liquid Refrigerant Flowing Inside A Refrigeration Machine. *International Journal of Applied Thermodynamics*, *4*(1), 53-60.

Lida, K., Yamamoto, T., Kuroda, T., & Hibi, H. (1982). Development of an energy saving oriented variable capacity system heat pump. *ASHRAE Transactions*, *88*(DA-88-6-4), 441–449.

Martin, H. (1996). A theoretical approach to predict the performance of chevron-type plate heat exchangers. *Chemical Engineering and Processing*, *35*(4), 301-310.

Michael D. Larrañaga, Mario G. Beruvides, H.W. Holder, Enusha Karunasena, & David C. Straus. (2008). DOAS & Humidity Control. *ASHRAE Journal*, 34-40.

Moreno Quibén, J., & Thome, J. R. (2007a). Flow pattern based two-phase frictional pressure drop model for horizontal tubes, Part II: New phenomenological model. *International Journal of Heat and Fluid Flow*, *28*(5), 1060–1072.

Moreno Quibén, J., & Thome, J. R. (2007b). Flow pattern based two-phase frictional pressure drop model for horizontal tubes, Part II: New phenomenological model. *International Journal of Heat and Fluid Flow*, *28*(5), 1060–1072.

Muley, A., & Manglik, R. M. (1999). Experimental study of turbulent flow heat transfer and pressure drop in a plate heat exchanger with chevron plates. *Journal of heat transfer*, *121*, 110.

Nidegger, E., Thome, J. R., & Favrat, D. (1997). Flow boiling andpressure drop measurements for R134a/oil mixtures part 1:evaporation in a microfin tube. *HVAC&R Research*, *3*(1), 38-53.

Niu, J. L., Zhang, L. Z., & Zuo, H. G. (2002). Energy savings potential of chilled-ceiling combined with desiccant cooling in hot and humid climates. *Energy and Buildings*, *34*(5), 487–495.

Perrotin, T., & Clodic, D. (2003). Fin efficiency calculation in enhanced fin-and-tube heat exchangers in dry conditions. *International Congress of Refrigeration*.

Qureshi, T. Q., & Tassou, S. A. (1996). Variable-speed capacity control in refrigeration systems. *Applied Thermal Engineering*, *16*(2), 103–113.

Radhi, H. (2009). Evaluating the potential impact of global warming on the UAE residential buildings-A contribution to reduce the CO2 emissions. *Building and Environment*, *44*(12), 2451–2462.

Rice, C. K. (1988). Efficiency Characteristics of Speed Modulated Drives at Predicted Torque Conditions for Air-to-Air Heat Pumps. *ASHRAE Transactions*, *94*(DA-88-6-4), 892-921.

Roth, K. W., Westphalen, D., Dieckmann, J., Hamilton, S. D., & Goetzler, W. (2002). Energy consumption characteristics of commercial building hvac systems–volume III: energy savings potential. *Final Report by TIAX LLC to US Department of Energy, Office of Building Technology, State and Community Programs*.

Sarntichartsak, P., Monyakul, V., Thepa, S., & Nathakaranakule, A. (2006). Simulation and experimental evaluation of the effects of oil circulation in an inverter air conditioning system using R-22 and R-407C. *Applied Thermal Engineering*, *26*(14-15), 1481-1491.

Schmidt, T. E. (1949). Heat transfer calculations for extended surfaces. *Refrigerating Engineering*, *57*, 351–357.

Shah, M. M. (1979). A general correlation for heat transfer during film condensation inside pipes. *International Journal of Heat and Mass Transfer*, *22*(4), 547–556.

Shen, B., & Groll, E. A. (2005). A Critical Review of the Influence of Lubricants on the Heat Transfer and Pressure Drop of Refrigerants-Part II: Lubricant Influence on Condensation and Pressure Drop. *HVAC&R Research*, *11*(4), 511.

Shimma, Y., Tateuchi, T., & Sugiura, H. (1985). Inverter control systems in the residential heat pump air conditioner. *ASHRAE Transactions*, *91*(HI-85-31).

Stefanuk, N. B. M., Aplevich, J. D., & Renksizbulut, M. (1993). Modeling and simulation of a superheat-controlled water-to-water heat pump. *ASHRAE Transactions*, *98*, 172–172.

Tcheou, E., & McNeil, D. A. (1994). The effect of ester-oils on heattransfer during evaporation of refrigerant HFC134a. *Proceedings of the 10th International Heat Transfer Conference* (pp. 551-556). Brighton, UK.

The benefits of Aluminum in HVAC&R Heat Exchangers. (2011). Sapa Heat Transfer.

Thermal Conductivity of some common Materials. (2011). . Retrieved March 5, 2011, from http://www.engineeringtoolbox.com/thermal-conductivity-d_429.html

Thome, J. R. (2004). Wolverine Engineering Data Book III. *Wolverine Tube Inc*.

Thome, J. R., El Hajal, J., & Cavallini, A. (2003). Condensation in horizontal tubes, part 2: new heat transfer model based on flow regimes. *International Journal of Heat and Mass Transfer*, *46*(18), 3365–3387.

Thome, J. R. (2011). Personal Communication.

Tran, T. N. (1998). *Pressure drop and heat transfer study of two-phase flow in small channels*. (PhD Thesis). Texas Tech University.

Tribbe, C., & Müller-Steinhagen, H. M. (2000). An evaluation of the performance of phenomenological models for predicting pressure gradient during gas-liquid flow in horizontal pipelines. *International Journal of Multiphase Flow*, *26*(6), 1019-1036.

US Department of Energy. (2010). *Buildings Energy Data Book*. US Department of Energy.

Wanniarachchi, A. S., Ratnam, U., Tilton, B. E., & Dutta-Roy, K. (1995). Approximate correlations for chevron-type plate heat exchangers. *ASME-PUBLICATIONS-HTD*, *314*, 145–152.

Wei, W., Ding, G., Hu, H., & Wang, K. (2008). Models of thermodynamic and transport properties of POE VG68 and R410A/POE VG68 mixture. *Frontiers of Energy and Power Engineering in China*, *2*(2), 227–234.

Willingham, R. A. (2009). Testing and modeling of compressors for low-lift cooling applications.

Wojtan, L. (2005). *Experimental and analytical investigation of void fraction and heat transfer during evaporation in horizontal tubes* (PhD Thesis).

Wojtan, L., Ursenbacher, T., & Thome, J. R. (2005a). Investigation of flow boiling in horizontal tubes: Part I–A new diabatic two-phase flow pattern map. *International journal of heat and mass transfer*, *48*(14), 2955–2969.

Wojtan, L., Ursenbacher, T., & Thome, J. R. (2005b). Investigation of flow boiling in horizontal tubes: Part II–Development of a new heat transfer model for stratified-wavy, dryout and mist flow regimes. *International journal of heat and mass transfer*, *48*(14), 2970–2985.

World Building Council for Sustainable Development (WBCSD). (2008). *Energy Efficiency in Buildings*. World Building Council for Sustainable Development (WBCSD).

Youbi-Idrissi, M., & Bonjour, J. (2008). The effect of oil in refrigeration: Current research issues and critical review of thermodynamic aspects. *International Journal of Refrigeration*, *31*(2), 165-179.

Zakula, T. (2011). Personal Communication.

Zakula, T. (2010). Heat pump simulation model and optimal variable-speed control for a wide range of cooling conditions.

Zürcher, O., Thome, J. R., & Favrat, D. (1997). Flow boiling andpressure drop measurements for R134a/oil mixtures part 1:evaporation in a plain tube. *HVAC&R Research*, *3*(1), 54-64.